Politecnico di Torino

Politecnico di Torino

Corso di Laurea Magistrale in Materials Engineering for Industry 4.0
A.a. 2023/2024
Ottobre 2024

Tesi di Laurea Magistrale

Manufacturing through Electron Beam Melting of hot-work tool steels

Relatore:
Prof. Federico Simone Gobber
Corelatore:
Prof. Daniele Ugues

Candidato:
Piemontese Luca

Abstract

The use of hot work tool steels is widespread in the production of tooling dedicated to metal forming processes, including forging and high-pressure die casting. A viable strategy to mitigate thermal gradients and enhance temperature distribution, thereby optimising the metal forming process and the working condition of the tool, is the production of tooling with internal hollow shapes and conformal cooling channels. The application of innovative metal additive manufacturing techniques, such as electron beam melting (EBM) offers a competitive advantage in the production of components with complex shapes that would otherwise be unattainable through subtractive manufacturing. However, due to the rapid melting and solidification process starting from a material in powder form, the materials produced by additive processes are often characterized by anisotropic microstructures, high residual stresses and microstructural inhomogeneity. Such techniques also allow to obtain finer microstructures with great advantage of mechanical properties such as wear resistance and impact toughness. The microstructural properties of hot-work tool steels are particularly suitable to face wear and mechanical stress at high temperature, nevertheless the correct heat treatment has to be identified to achieve the most appropriate microstructural properties. This work covers the study of the heat treatment of an AISI H13 hot work tool steel, obtained from nitrogen atomized powders and manufactured through EBM with a powder bed preheat temperature of 1040°C. Despite showing a hardness of 47 HRC, the EBM material showed clear carbide precipitation phenomena, due to long high temperature permanence (about 5.3 hours) and subsequent slow cooling (about 6.2 hours) in He. Starting from the literature on nitrogen-containing wrought AISI H13. The effect of austenitization temperatures between 1025°C and 1100°C on the as quenched alloy was studied by microstructural studies and hardness assessment; the tempering curves were built in a range between 400°C and 650°C for samples austenitized at 1050°C and 1100°C respectively. The microstructure was studied by scanning electron microscopy (SEM), which revealed the presence of undissolved carbides. The size of these carbides was measured by means of image analysis (Imagej software). Carbide size distribution curves were determined for each heat treatment condition to characterize the effect of solubilization at higher temperatures due to austenitization, as well as the effect of precipitation of carbides after tempering and hardness after double tempering was correlated to the impact released energy starting from the as-built condition. Moreover, the tempering curves were built using macro-hardness measurements as a function of tempering temperature to determine the optimal heat treatment condition.

Contents

List of Figures

List of Tables

Chapter 1

Introduction

This work focuses on the study of the heat treatment of an AISI H13 hot-work tool steel, obtained from nitrogen atomized powders and manufactured through Electron Beam Melting (EBM) with a powder bed preheat temperature of 1040°C. This research is inserted in the framework of new Additive Manufacturing techniques for the processing tool steels. AM can be successfully applied to traditional steel grades obtaining peculiar microstructural properties, moreover it allows to produce more complex geometries with respect to machining, which can effectively prolong tool life. The present work also deals with the influence of nitrogen additions on the microstructural properties of as-built and heat treated H13 samples, starting from literature research on the wrought material. This addition occurred during powders production, through nitrogen gas atomization, and is considered a novel paradigm for the production of superior tools and molds capable of sustaining higher loads for a prolonged working time.

Tool steels are a wide set of carbon or alloyed steels used for the manufacturing of tools, inserts, dies and matrices. They are largely implemented for industrial applications for their mechanical properties to shape, deform or cut other materials. Tool steels can be classified according to the AISI standard in ten categories identified by a capital letter according to their manufacturing process, their chemical composition or their final application [1]. In this context, hot-work tool steels are a specific class which is normally adopted for applications in open and closed die forging, die casting or hot rolling. This category of materials requires a complex manufacturing process, starting from EAF melting, following with secondary metallurgy processes, such as AOD and VOD, and continuing with ingot remelting technologies, such as ESR and VAR, to obtain a controlled chemical composition and minimizing ingot solidification defects such as segregations, inclusions and internal inhomogeneities [2]. This work focuses on metallurgical aspects of hot-work tool steels, in particular the AISI H13. This steel is widely applied to manufacture dies for High Pressure Die Casting (HPDC), molds for injection molding and hot

extrusion matrices. Its microstructure made of tempered martensite along with high temperature resisting carbides such the MC-type rich in V, allow hot-working applications for prolonged times at temperatures such as 500°C. The conventional heat treatment of H13 parts is divided in many steps, including quenching and multiple tempering to reach the final target hardness and toughness.Recent studies have shown the effect that external elements such as nitrogen have on the microstructure of wrought H13. Nitrogen addition can increase the stability of MC-type carbides during austenitizing while decreasing grain coarsening at higher temperatures. Moreover it promotes the precipitation of finer nanometric carbides during tempering [3]. These considerations have been reported in chapter 2 of the present thesis.

It is widely known that traditional metallurgy has intrinsic limits linked to the cooling rate during primary solidification, causing the formation of dendritic and columnar structures. In recent years Powder Metallurgy (PM) has promised to overcome these issues, allowing to obtain finer and more homogeneous microstructures with respect to castings, obtaining higher properties in terms of impact energy and ductility, by maintaining high mechanical properties. In the context of PM, Additive Manufacturing (AM) techniques allow to obtain complex shapes not achievable by machining, attributing features such as conformal cooling channels to dies and inserts, improving heat dissipation and ensuring longer life. In chapter 3 a brief description of the most relevant metal additive manufacturing techniques for tool steels is presented, in particular DED, SLM and EBM. After a general description regarding the principles and the mechanisms of each technique, a literature review of their application in the manufacture of AISI H13 products is presented, with a focus on the as-built microstructural evolution of the processed material due to rapid solidification and thermal cycling, typical of all DED and PBF techniques.

In chapter 4 the experimental work is presented, while results are discussed in chapter 5. This thesis has been developed starting from a previous work by [4], in which nitrogen containing AISI H13 powders were characterized and adopted for producing specimens with dimension 15×16×60 mm through EBM using an A2X Arcam (GE Additive) EBM machine with different process parameters in terms of scan speed and beam current. The as-built material was characterized through a porosity assessment, X-ray diffraction (XRD) measurement for retained austenite fraction, metallographic analysis and differential scanning calorimetry (DSC). However, despite showing low porosity level and a hardness of 47 HRC, it showed clear carbide precipitation phenomena, due to long high temperature permanence (about 5.3 hours) and subsequent slow cooling (about 6.2 hours) in He. The effect of austenitizing temperatures between 1025°C and 1100°C on the as-built alloy was evaluated by scanning electron microscopy (SEM) and energy-dispersive

X-ray spectroscopy (EDS), which revealed the presence of undissolved carbides and a hardness assessment to study carbides dissolution phenomena; the tempering curves were built in a range between 400°C and 650°C for samples hardened at 1050°C and 1100°C respectively. Carbide particle size distribution (PSD) curves were determined for each heat treatment condition to characterize the effect of solubilization at higher temperatures due to austenitizing, as well as the effect of precipitation after tempering. The evolution of PSD curves through the full heat treatment was measured by means of image analysis (Imagej software), together with carbide volume fraction. The changing of retained austenite was measured through XRD analysis. Moreover, the tempering curves were built using macro-hardness measurements as a function of tempering temperature to determine the optimal heat treatment condition for each final application.

Chapter 2

Tool steels

In this master thesis large space is left to the specific description of the AISI H13 hot-work tool steel. Nevertheless, before deepening in this specific argument it is necessary to cite the entire category of tool steels in general to underline what are their main alloying strategies and microstructural features and to give a complete context to the experimental work. In this chapter an introduction to the traditional metallurgy of tool steels is provided. The chapter continues with a description of the AISI H13 steel and its main microstructural features.

2.1 Generalities on tool steels

Tool steels are a wide set of carbon or alloyed steels used for the manufacturing of tools, inserts, dies and matrices [1]. Their applications range between extremely different conditions where high abrasion resistance, strength or good cutting performances are required. There is not a unique and standardized definition of these category of steels but, according to [2], tool steels generally possess three main features: ability to be applied as forming or cutting tools, a complex manufacturing process and strong hardenability by heat treatment. Expanding this definition, firstly they have elevated wear resistance together with shock resistance, which are the two main requirements for tools forming or cutting other materials, such as softer metals like aluminium and plastics. Secondly, they are usually manufactured through complex forming process going beyond traditional blast furnace technologies and requiring a much finer process control. In most of the cases Electric Arc Furnaces (EAF) are considered as a reference, often followed by ingot remelting technologies. In addition, new Powder Metallurgy (PM) and Additive Manufacturing (AM) techniques are emerging, as described in chapter 3. Thirdly, in almost all the cases, their very high hardness is reached through the application of a complex heat treatment made of quenching and multiple tempering, with the

aim of having a microstructure of tempered martensite containing finely dispersed carbides of alloying elements providing secondary hardness.

Tool steels base their functionality on well established alloying strategies in metallurgy. They usually have a high carbon content, promoting the ability to form martensite and to enhance its hardness. Their generally high carbides forming alloy elements content not only promotes solid solution strengthening, but especially precipitation hardening during tempering of martensite, achieving a combination between hardness and toughness. The higher the carbides forming elements content, the higher the overall hardness and wear resistance, but the lower the impact toughness. Moreover, according to the type of alloying element, some carbides cannot be easily dissolved during austenitization and therefore will contribute to reducing the forgiability of the final product [1], greatly impacting on the overall transformation costs.

According to [5], the global tool steel market was valued USD 5.07 billion in 2021 and it is estimated to reach USD 8.16 billion by 2030 at a compound annual growth rate (CAGR) of 5.3%. A similar trend is reported by [6], which valued the global tool steel market USD 5.25 billion in 2021, forecasting a CAGR of 4.5% from 2022 to 2028. Available data from the year 2022 is confirming this trend: according to [7], the same market was evaluated USD 5.8 billion, while the forecast CAGR will be 4.80% from 2023 to 2030. The demand for these kind of special steels is driven by the automotive and aerospace sector where they are fundamental for every kind of open and closed-die forging applications. Moreover, the worldwide growing demand for relatively low cost products manufactured by injection molding is increasing the demand for forming molds and inserts, as well as cutting tools. Expansion is driven by the Asia-Pacific region due to its growing industrialization, automotive industry demand and infrastructure investments. Europe and North America stands as second and third poles in today's tool steel market.

2.2 Tool steels classifications

The designation of tool steels is not unique and follows the standards of different countries. The most common one is the American Iron and Steel Institute (AISI) classification developed by the American Society for Testing and Materials (ASTM) [8], [9]. It divides tool steels according to several features, such as alloying elements, application and heat treatment [1], assigning a letter to each group and a number to each single grade. A list of most of the alloy grades standardized by ASTM are reported in table 2.1. Another typical standard is the Unified Numbering System (UNS) classification, developed by ASTM and by Society of Automotive Engineers (SAE). Furthermore, the ISO standard [10] is also used, which defines each grade through an alphanumeric code based on its chemical

Table 2.1: Main tool steels groups in the AISI standard [1].

Tool steels group	**Identifying Symbol**
Water-hardening tool steels	W
Shock-resisting tool steels	S
Oil-hardening cold-work tool steels	O
Air-hardening, medium-alloy cold-work tool steels	A
High-carbon, high-chromium cold-work tool steels	D
Mold steels	P
Hot-work tool steels, chromium, tungsten, and molybdenum	H
Tungsten high-speed tool steels	T
Molybdenum high-speed tool steels	M

composition or a numeric code. Besides these main standards, many other are available for the designation of tool steels and are currently adopted by different countries. Some of them are the JIS (Japan), the BS (United Kingdom), AFNOR (France), or SSH (Sweden) [2]. An example of cross reference table for some of the AISI H (hot-work tool steels) is reported in table 2.4.

As depicted by table 2.1 the AISI standard classifies tool steels in nine main categories. In the following lines a brief description for each category is reported [1]. Water-hardening tool steels (W types) are mostly carbon steels based, having low hardenability (only the surface is fully quenched) and only Fe-type carbides after tempering. Shock-resisting tool steels (S types) are suited for impact loading conditions. They have low C content and finely dispersed carbides, they are more alloyed with respect to W types, therefore more hardenable, but still tougher. Oil-hardening cold-work tool steels (O types) are medium alloyed, having high C martensite, giving more hardenability, and very fine carbides dispersion due to low temperature tempering. They are suited for cold working applications. Air-hardening cold-work tool steels (A types) are also suited for cold working, but the higher alloy content allows quenching in air with better dimensional stability. High-carbon, high-chromium cold-work tool steels (D types) have the highest wear resistance. Their microstructure consists of tempered martensite and a great amount of primary and secondary carbides. Their machinability is therefore complex and toughness is usually low. Mold steels (P types) have good machinability in the annealed state to allow complex geometric features. Then, they are carburized and hardened to get surface wear resistance. Hot-work tool steels (H-types) have high temperature strength and toughness, together with thermal cracking

resistance. This set of requirements is obtained by relatively high temperature tempering to obtain a microstructure of tempered martensite and fine high temperature carbides. More space is given to this class of tool steels in 2.4. Tungsten high-speed tool steels (T types) and molybdenum high-speed steels (M types) are used for high-speed cutting applications. They have a very high content of stable carbide forming elements, such as tungsten, allowing to maintain hardness even at red-hot condition. The molybdenum is sometimes replacing part of the tungsten allowing slightly higher toughness. The summary table 2.2 of these main classes is reported from [2], where all types of cold-work tool steels (W, S, O, A, D) and high-speed steels (T, M) have been grouped together. This families of tool steels

Table 2.2: Summary of main properties and representative of the the main tool steels groups [2].

Tool steels general group	**AISI classes**	**Main properties**	**Main representative AISI/DIN**
Cold-work tool steels	W, S, O, A, D	Cold hardness, Wear resistance	D2/1.2379
Hot-work tool steels	H	Hot strength, Toughness	H13/1.2344
Mold steels	P	Hardenability, Surface finishing	P20/1.2738
High-speed steels	T, M	Hot hardness, Wear resistance	M2/1.3343

cannot satisfy many multiple requirements at the same time in most of the cases. For example, D2 steel is one of the most exploited candidates for the construction of cold trimming or cutting tools, due to its extreme wear resistance mostly due to its carbon content of about 1.4% - 1.6% and chromium of 11% - 13%. On the other hand, for a hot working die casting application, steels such as H11 or H13 with lower amount of carbon and chromium must be preferred, due to their softening and heat checking resistance as well as toughness. Moreover, several surface treatments such as carburizing and nitriding are often applied to softer steels, while treatments such as physical vapour deposition (PVD) or chemical vapour deposition (CVD) of hard ceramic materials are applied on high-speed steels [11]. This certainly complicates the final choice, but allows to offer a tuned material for each application. Overall, the selection of the correct tool steel for a specific case is a complex process which begins with the identification of the correct group and concludes with a final choice. In addition to mere experience, nowadays more simulations software tools are available on the market allowing additional time and money savings.

2.3 Traditional manufacturing of tool steels

As introduced in section 2.1, one of the main features of tool steels is their particular manufacturing process. With this respect, they share similar difficulties with other types of highly alloyed steels, like stainless steels, such as the necessity of controlling a complex chemical composition made of elements whose oxides are particularly stable such as Cr, Mo, V. Nowadays, the entire panorama of manufacturing processes can be divided in two branches: the first branch regarding traditional metallurgical processes and the second one regarding powder metallurgy.

Traditional processes for tool steels are a set of technologies that have been mostly developed within the course of the XX century, starting from the smelting of metal to obtain a solid semi-product which is plastically deformed towards a final part. Since this category of steels is normally manufactured in relatively small lots (at least when compared to carbon steels), their manufacturing process is mainly composed by discontinuous steps, working on a small and predefined amount of material. Moreover, they often demand the usage of complex and expensive technologies with respect to the integrated steelmaking route, to obtain a precise control on chemical composition and microstructure. This is usually justified by a higher cost per part. A scheme representing the main manufacturing route for tool steels is shown in figure 2.1. Tool steels have a chemical composi-

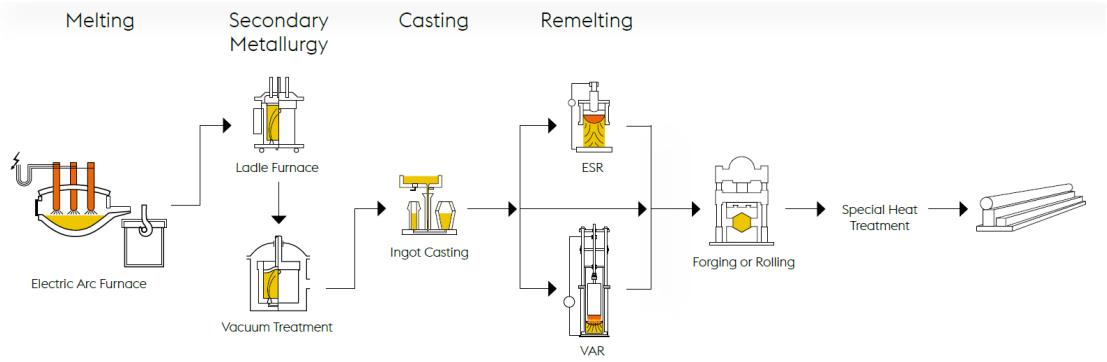

Figure 2.1: Simplified schematics of the traditional processing route for the manufacturing of tool steels, courtesy of Voestalpine Böhler [13].

tion rich in alloying elements: in addition to C that can reach also 2.1%, Cr until 11% - 12%, or even W and Mo, they are required to have low levels of deleterious elements such as S and P, normally below 0.03%. These requirements are mostly satisfied through melting and secondary metallurgy steps. Nowadays, melting is mostly performed in electric arc furnaces (EAF), starting from end-of-life steel

parts and scraps. The EAF uses the heat generated by electric arcs produced by graphite electrodes, which are inserted from the top of the furnace, to melt the metal. Modern ultra high power (UHP) furnaces offer the possibility of providing heat also by oxygen blowing lances and burners, reducing energy costs. Here several steps of composition refining can be performed. Despite that, for highly alloyed steels more steps are required, specifically the argon-oxygen decarburization (AOD) or even the vacuum-oxygen decarburization (VOD). The first process, similar to the traditional basic oxygen furnace decarburizer (BOF), is adopted to reach low carbon content in the melt, without reducing the amount of more oxygen affine elements such as Cr, which otherwise would be forming the correspondent oxide. The working principle is based on the reduction of the partial pressure of CO by diluting the gas using Ar and other inert gases. On the other hand, the usage of VOD is strictly related to very low carbon content alloys with higher costs. It uses vacuum to directly remove CO from the melt, allowing finer control. Afterwards even more refining steps can be performed to reduce S, or dissolved gases (using vacuum arc degasing). After the secondary metallurgy processes, the ingot casting step is performed. As aforementioned, tool steels are produced in small lots, hence this casting procedure is adopted instead of continuous casting. During solidification many defects form, such as the shrinkage cavity, segregations, banding and skin-core microstructural differences. It is possible to control such defects by working on remelting technologies, normally adopted for high quality productions only, such as electro slag remelting (ESR) and vacuum arc remelting (VAR). They allow to obtain much finer ingot microstructures and higher level of purity. Despite that, it is still not possible to completely avoid all solidification defects [2]. The final step of this route are thermomechanical processes. Foundries use mechanical actions together with high temperature to change the shape of metal semi-products. Moreover, by applying mechanical stresses, it is possible to break previously formed inclusions, reducing their size and possibly avoiding elongated shapes to reduce the stress intensity factor. Another key role of this phase is the closure of inner shrinkage cavities, formed after solidification. The two main classes of processes for tool steels are forging and rolling. Both of them are performed on a microstructure made of an austenitic matrix with dispersion of primary carbides. After this phase, an annealing step is required to have an homogenous and ductile microstructure at room temperature to allow a correct and easier machining. After this last stage the final heat treatment begins which will be discussed in more details in section 2.5.1, followed by finishing operations.

On the other hand, Powder Metallurgy (PM) does not involve the casting of a liquid metal, but it starts from the manufacture of metal powders and their assembly into dense objects. According to this definition adapted from [12], the first step is production of powders. Nowadays many methods exist, some of which

can be considered as physical methods, such as mechanical milling or atomization, others are chemical methods, such as reduction or carbonyl route. Each type of powder production process influences the final shape, size, porosity and chemical composition of powders, making them more adapt to a specific densification technique. Powder metallurgy allows to obtain much finer microstructures with respect to traditional metallurgy, avoiding the presence of defects coming from ingot solidification or banded structures due to the rolling process. This is a key advancement in metal tools manufacturing since it translates in a sharp increase in toughness, ductility and fatigue life [2]. A particular in-depth analysis is reserved for Additive manufacturing techniques, which are also considered as part of powder metallurgy, in chapter 3, due to their relevance in this work.

2.4 Hot-work tool steels

In this work, chapters 4 and 5 are dedicated to the processing of AISI H13 steel deriving from EBM additive manufacturing route. Therefore, this preliminary section is also focused on the description of the H category of the AISI standard, i.e. hot-work tool steels.

This class of steels is employed in many hot working applications ranging from die casting, towards plastic deformation processing, such as open die, closed die and hammer forging where their impact loading resistance and toughness is exploited. Others applications include hot extrusion and hot rolling. H type tool steels are widely used for manufacturing dies for the High-Pressure Die Casting process (HPDC), where liquid metals with lower melting point than steel are injected in a closed die under high pressure using a piston, processing metals such as tin, lead, zinc, aluminium and magnesium alloys. The temperature of the liquid, is about 700°C for Al alloys, which are the most common ones for HPDC. Pressure is kept until solidification of the part, which is normally in the order of milliseconds to seconds, hence the surface of the tool is facing a maximum temperature of about 650°C [2]. Another common application is to manufacture molds for plastic injection molding. Compared to the HPDC, here a less demanding set of properties is required, allowing longer mold life in general. In all the main cases of application of hot-work tool steels, they are used to build relatively large and complex components with a high production cost deriving both from the material cost (due to the presence of many alloying elements) and from the machining and heat treatment stages, which are both usually long and expensive. Overall the cost of a single unit can reach up to a several thousand USD [2].

Normally, the strength of materials decreases with temperature due the increased lattice energy allowing dislocations to overcome obstacles more easily using their own thermal energy [14]. Hence, the dispersion of fine carbides in addition

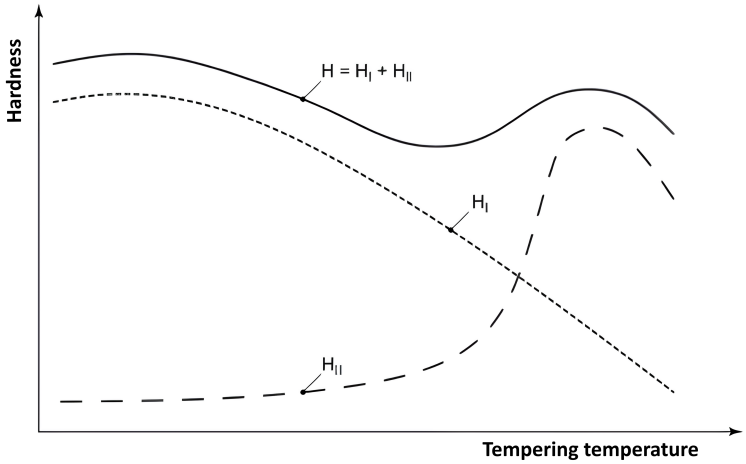

Figure 2.2: Evolution of surface hardness of a typical hot-work tool steel as a function of temperature. The two hardness contributions of martensite (I) and carbides (II) are enlightened.

to tempered martensite is the most common way to satisfy high temperature applications as it is shown in figure 2.2. To satisfy high temperature applications, hot-work tool steels have been designed, starting from 1940s [2], to have high hot wear resistance and hot hardness to ensure a longer tool life during operations and resistance to deformation. In addition, other requirements are researched, such as high tempering resistance and softening resistance after multiple hours of work, together with heat checking resistance (ability to withstand thermal fatigue cracking). Moreover, through a relatively low content of alloying elements, with respect to many cold-work tool steels and high-speed steels, it is possible to design tougher microstructures with low density of finely dispersed carbides, making hot-work tool steels adapt to impact loading conditions and in general reducing the risk of crack propagation due to heat checking. This set of properties cannot be obtained without a complex heat treatment procedure, hence a certain grade of resistance to heat treatment distortion is needed. With this respect, air hardening capability is requested in order to minimize the effects of quenching on thin and complex features [1]. Lastly, decent responding to surface treatments is requested, such as nitriding [2]. This surface treatment is widely used when high hardness (about 900 - 1000 HV), is needed.

Hot-work tool steels are divided into three subcategories, in accordance to their chemical composition and alloying strategies, offering different behaviours in hot-work conditions. They are listed in table 2.4 as follows:

- Chromium hot-work tool steels;

- Tungsten hot-work tool steels;
- Molybdenum hot-work tool steels.

In the following, each of this three typologies is presented, trying to enlighten their own differences and metallurgical properties.

2.4.1 Chromium hot-work tool steels

Chromium hot-work tool steels are the most common and widely used due to their versatility and relatively lower cost with respect to the other two types. They were originally developed for die casting applications and forging. They have in common a similar chemical composition, as shown in table 2.5, with a carbon content between 0.30 - 0.45 wt%, which is relatively low with respect to other tool steels. This allows to maintain higher toughness and relatively high martensite start (M_s) temperatures, allowing easier hardenability. They all have a chromium content between 4.00% - 5.50% in weight (with the only exception og AISI H10) and most of it is contained in carbides of the type of M_7C_3 or $M_{23}C_6$. These primary and secondary solidification carbides need to be dissolved during annealing to enhance formability and during austenitizing. The presence of alloying elements such as molybdenum also enhances hardenability by shifting Continous Cooling Transformation (CCT) curves to the right, so promoting formation of martensite during quenching, even in air cooling conditions. In addition to chromium and molybdenum, also small wt% of tungsten and vanadium are alternatively present in the final chemical composition (usually about 1.00 - 2.00 wt% with some exceptions). These strong carbides forming elements tend to form stable carbides of the type of MC and M_2C (for vanadium) or M_6C (molybdenum). Austenitizing is therefore adopted to dissolve them, even if vanadium and tungsten carbides are not completely dissolved in austenite even at 1100°C. After quenching double tempering is needed to achieve final properties in working temperatures. It is noted that most of the hardening action in tempering is due to precipitation of very fine vanadium rich MC-type carbides at temperatures around 500°C - 600°C where it is normally located the hardness peak [1]. At higher temperatures, not only tempered martensite transforms into ferrite and spheroidal cementite, but chromium-rich M_7C_3 and molybdenum-rich M_6C carbides form, rapidly coarsening and not significantly contributing to strength [1].

2.4.2 Tungsten hot-work tool steels

Tungsten hot-work tool steels are the oldest one to be designed, between the three. Their chemical composition is extremely rich in W ranging between 8.5 wt% towards 19 wt%, with moderate amounts of C, Cr and V. They posses the

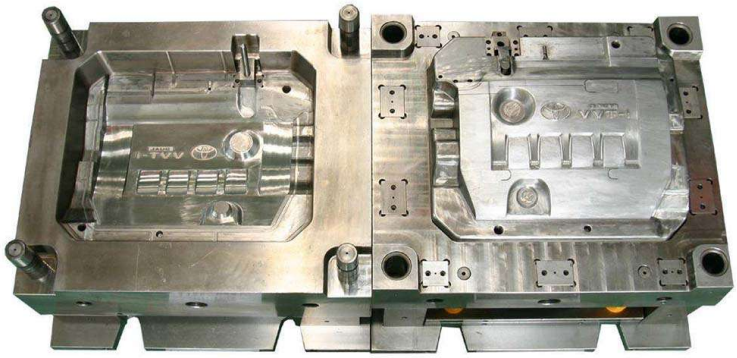

Figure 2.3: Example of mold manufactured in AISI H13 [15].

highest hot hardness and lower toughness as well thermal shock resistance, due to elevated brittleness. For this reason normally they cannot be rapidly cooled using water. They are used for hot working extrusion dies, drawing dies, shear blades and hot punches [1]. Tungsten is a strong ferrite-stabilizing and carbide forming element: the two main strengthening carbides are W-rich M_6C and M_2C, being the latter one associated with peak hardness during tempering.

2.4.3 Molybdenum hot-work tool steels

Molybdenum hot-work tool steels are the least famous between the three. They were developed as an alternative with respect to tungsten due to their lower cost, but nowadays the only still used example is AISI H42. Its properties are intermediate between the other two classes, containing about 4 %wt of Cr, 5 %wt of Mo and 6 %wt of W. This elements enhance hardening and form carbides giving secondary hardening as well, similarly to the other two groups [1].

2.5 The AISI H13 hot-work tool steel

The core of this work is based on the study of the properties of the H13 hot-work tool steel, one of the most widely used materials for manufacturing HPDC molds and forging dies. An example is reported in figure 2.3. Its peculiar properties range from hardenability and hot-hardness, small heat treatment distortion, low tendency to oxidation, tempering resistance, heat checking resistance and corrosion resistance against molten aluminium. It can be nitrated to achieve hardness greater than 1000 HV [2]. Its complete chemical composition is reported in table 2.5. H13 steel contains a moderate amount of C between 0.32 - 0.45 %wt similarly to other chromium hot-work tool steels, as described in section 2.4.1. In the chemical

composition there are small amounts of Mn (ranging between 0.20 - 0.50 %wt) and Si (ranging between 0.80 - 1.20 %wt). Manganese is an austenite-stabilizing element which not only contributes in solid solution strengthening, but is mostly added to neutralize sulphur and oxygen based inclusions. On the other hand silicon is ferrite-stabilizing element with the ability of increasing the yield strength of steels through interstitial solid solution strengthening, moreover it increases tempering resistance due to its ability to reduce cementite formation [1]. As far as chromium, molybdenum and vanadium are concerned the same considerations reported in section 2.4.1 are still valid, including the role of Cr in hardenability and in forming carbides, which are dissolved during forging and quenching, and the role of V-rich carbides in secondary hardening. Furthermore, no tungsten is inserted in the final chemical composition. Time-Temperature-Transformation (TTT) curves and Continuous Cooling Transformation (CCT) curves, relative respectively to 1010°C and 1020°C austenitization temperatures, are reported in figure 2.4. It is possible to observe that the perlitic and bainitic nose are well separated and shifted to the right allowing easy hardenability even with moderate cooling rates, hence avoiding high inner residual stresses and thermal cracks.

2.5.1 Wrought AISI H13 microstructural aspects during preliminary heat treatments

In this section a brief discussion is presented about the effects of a certain microstructure on final properties of the H13 hot-work tool steel, even if most of these considerations are generalizable to other classes of tool steels. This correlation is enlightened by It is widely known that the same material, i.e. same chemical composition, can present many different microstructures according to its metallurgical state due to a certain thermal history, therefore it is important to deepen this argument as a basis for the next chapters.

The microstructure of the H13 steel needs to be tuned for hot-working conditions such as working at 500°C, where normal carbon steels are loose their mechanical characteristics. Therefore, in its final stage it is constituted by a matrix of tempered martensite with an array of finely dispersed carbides with nanometric size to better have a pinning action against movement of dislocations. This allows to couple relatively high toughness with strength. To reach this final microstructure many steps are required, where several phases play a important role. In addition to these fine carbides, which are called secondary carbides since that they are precipitated during the heat treatment, some larger carbides are present coming from solidification of the liquid, i.e. primary carbides. One of the biggest problems regarding traditional manufacturing is that primary carbides have usually elongated shapes, following previous grain boundaries of primary austenite,

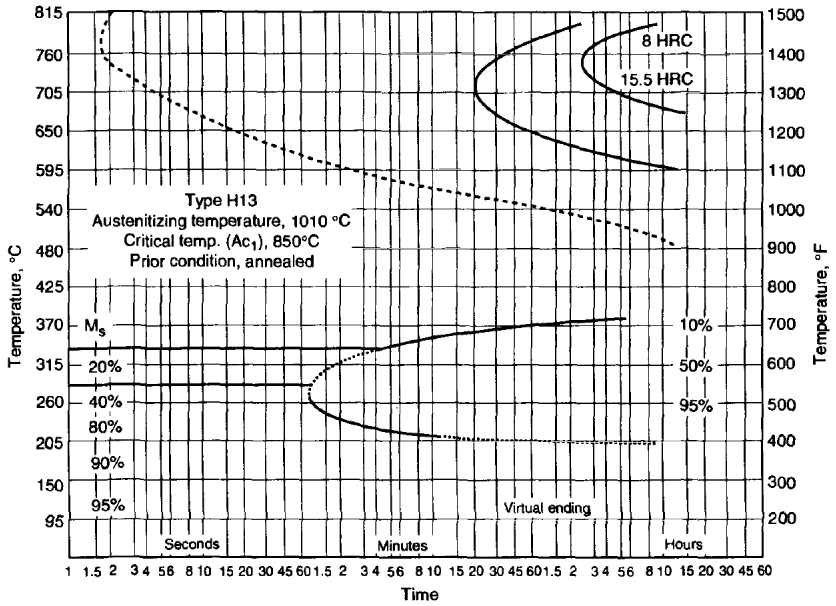

(a)

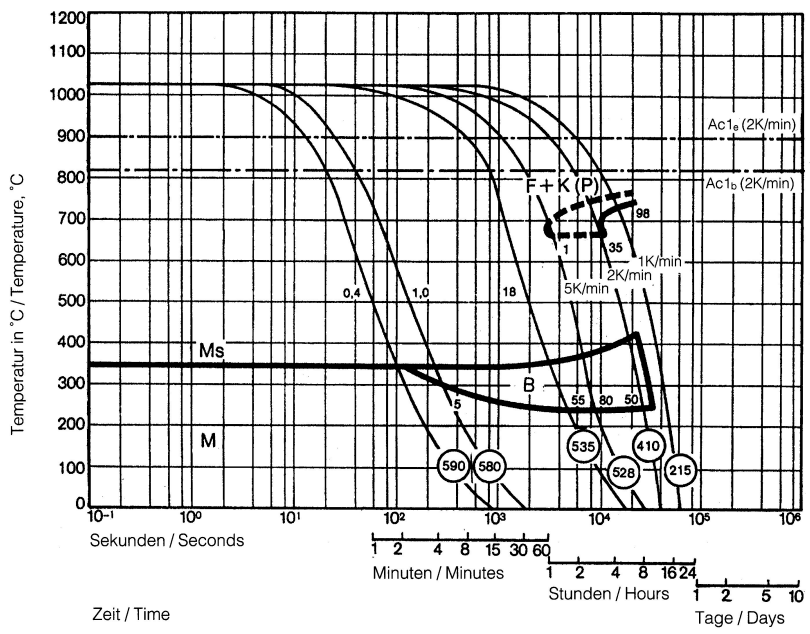

(b)

Figure 2.4: (a) TTT curve for AISI H13 tool steel after austenitization at 1010°C where dashed line represents carbides precipitation [1], (b) CCT curves for AISI H13 tool steel after austenitization at 1020°C [13].

and are only partially affected by all heat treatments due to their large size in the order of microns [2]. This happens since normal cooling rates are quite slow, allowing the formation of large and elongated structures and segregations. This problem can be tackled through the adoption of remelting technologies as described in section 2.3 or in a much more effective way using Powder Metallurgy (PM).

Apart form these cases, after ingot casting typical solidification structures are generated with small equiaxial grains on the surface due to rapid heat exchange with the walls in addition to columnar and coarser equiaxial grains at the core. Directly after solidification the first formed phase in the H13 steel will be δ-ferrite, i.e. the BCC phase of steel with thermodynamic stability in the highest temperature range directly below the liquid phase. As temperature lowers the peritectic transformation occurs and δ-ferrite transforms to austenite (the FCC phase of steel where solubility of alloying elements is the highest) and liquid phase, which will turn to austenite as well [16]. Different is the case of Additive Manufacturing (AM), where cooling rates can even be of the order of 10^4 - 10^6 K/s. A brief description is reported in chapter 3. To save energy consumption (especially for large pieces), high ingots are not let cool down to room temperature but they are directly held in a reheating furnace in order to avoid austenite to ferrite transformation until forging (or rolling eventually) begins. As said in section 2.3, the forging step will refine the microstructure leading to more homogeneity [2]. For H13 steel forging is usually performed at 1050°C - 1100°C after a preheat stage at 750°C, to exploit lower strength and higher ductility, always keeping temperature above 850°C - 870°C to avoid cracking. After the forging cycle, slow furnace cooling is necessary [17]. This slow cooling is important to avoid thermal cracks, in facts at this stage the austenitic microstructure is still coarse, hence heavy presence of coarse martensite laths or bainite should be avoided to avoid excessive brittleness [2]. After forging, the final annealing begins. The aim of this step is to prepare an ideal microstructure for machining operations, i.e. a softer material with a controlled grade of ductility to avoid too long chip formation. Since, machining is performed at room temperature the best microstructure is a purely ferritic matrix with dispersed carbides of alloy elements (Cr, Mo, V). This annealing is performed between 840°C - 900°C for 6 - 8 hours to have a homogeneous microstructure made of large spheroidal carbides in ferrite [2], [17]. Machining in general can be divided into two subcategories: roughing and finishing. In roughing processes most material is removed from the starting work part, cutting is performed with high depths and low speeds with tolerance in the mm range. Finishing processes are for receiving final dimensions and surface finish and is performed after the final heat treatments due to their loss of tolerances. After the roughing process, large pieces of H13 undergo a stress relief treatment between 600°C - 700°C [17] to recover heavy residual stresses left by the previous workings.

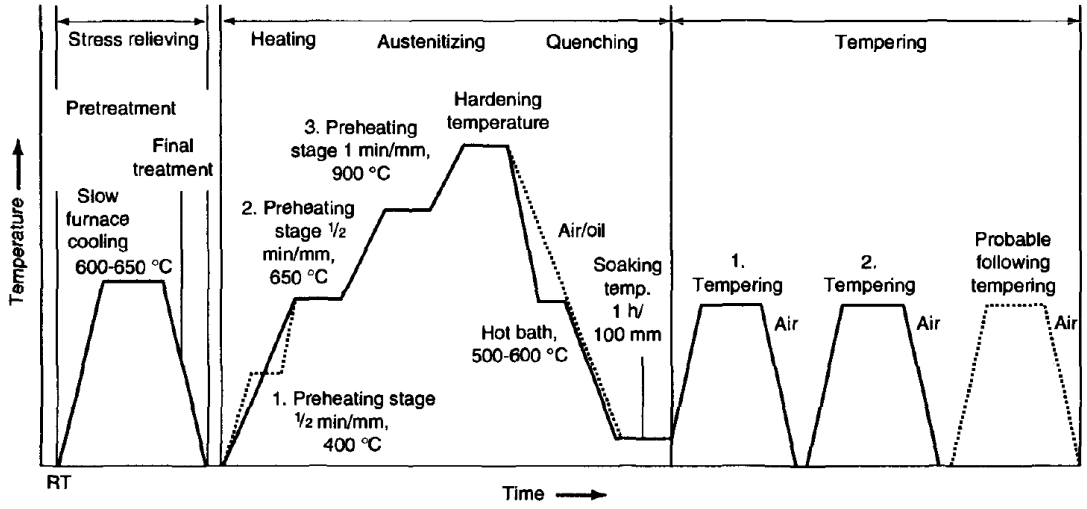

Figure 2.5: Schematics of the stress relieving, quenching and tempering steps of AISI H13 tool steel, with the courtesy of [1].

2.5.2 Wrought AISI H13 microstructural aspects during final heat treatments

At this stage the microstructure of is still not optimal for the final application. Therefore, final heat treatment sequences are needed. A schematics of the heat treatment presented in this section is shown in figure 2.5. Ferrite is the BCC phase of low temperature of steel and despite the solid solution strengthening and precipitation hardening of alloying carbides, it has very low hardness and abrasion resistance. Therefore, a series of austenitizing, quenching and tempering are needed. This is normally what is intended as proper heat treatment in literature. Austenitizing has the role to reach an homogeneous fine austenitic microstructure. For AISI H13 and other tool steels the beginning of the totally austenitic range (A_{c3}) is well above 750 - 850°C as in carbon steels, due to the presence of many ferrite stabilizing elements in solid solution and in carbides. During austenitizing most of the carbides should be dissolved to allow more carbon to produce the martensitic transformation and to allow alloying elements to produce secondary carbides during tempering. Despite that some of them such as VC carbides will need much higher temperatures to be completely dissolved, which will cause too high grain coarsening. Austenitizing for H13 are performed at temperatures greater than 1000°C, usually between 1020°C - 1080°C according to the single producer [13] for 30 minutes with multiple preheating stage. During the quenching step a rapid cooling is used through a quenching medium, such as oil, air, molten salts or high pressure gas in vacuum furnaces to make the martensitic transformation.

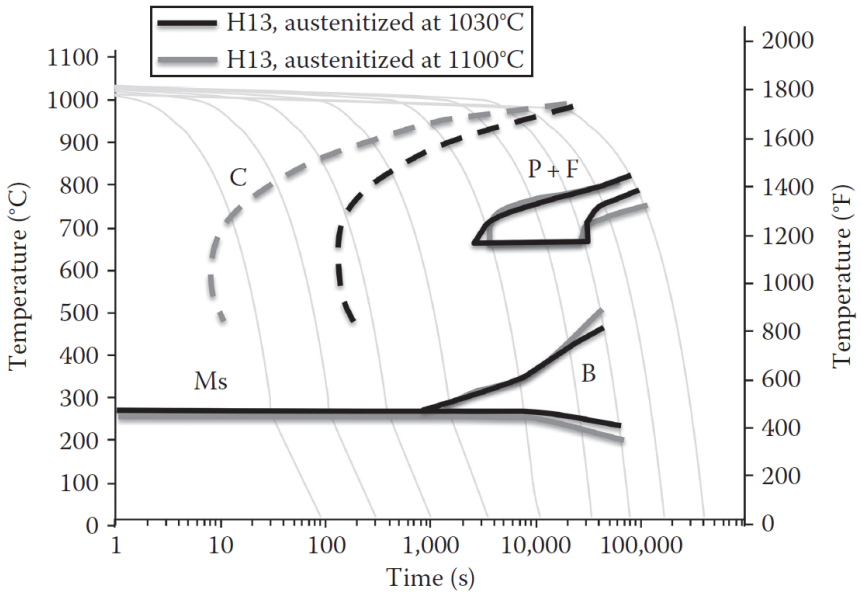

Figure 2.6: Effect of austenitizing temperature on CCT curves in AISI H13. Dashed curves represent carbides precipitation. Quenching embrittlement is enhances for higher austenitizing temperatures [2].

Martensite is the TCC metastable phase of steels obtained through a fast and diffusionless motion of atoms from austenite, it is characterized by very high hardness (normally as a function of many factors such as carbon content and prior austenite grain size, but even around 500 - 700 HV [18]) and brittleness. Normally, due to very low temperature location of martensite finish (M_f), a certain fraction of retained austenite remains, which plays a detrimental role in tool steels due to its ability to transform to martensite after stress application causing dimensional variations [2]. Another key aspect regarding quenching is the so called quenching embrittlement. This phenomenon can occur during cooling and consists in the precipitation of carbides (especially V or Mo-rich ones) at the austenite grain boundaries. Even if the volume fraction of such carbides is small they can form a preferential path for crack propagation reducing impact toughness. Quenching embrittlement may occur if the cooling rate is not fast enough or if the austenitizing temperature is too high, since when there is a high concentration of alloy elements in solid solution in austenite they can be easily pushed towards grain boundaries to form carbides [2]. This effect is shown in figure 2.6 where carbide precipitation curves are shown. To reduce the great amount of internal stresses and increase toughness of martensite tempering is needed. Tempering consists of a heating at a certain temperature for 2 hours in the ferritic/pearlitic range to promote the transformation of martensite. During tempering many diffusive transformations occurs.

At lower temperatures between 100°C - 250°C, carbon atoms start to diffuse from the TCC cell of martensite and there is formation of transition carbides such as ϵ or η of the type Fe_2C. In the temperature range of 200°C - 300°C retained austenite transforms to ferrite and cementite, while above 250°C - 300°C transition carbides and low-carbon martensite also transform to ferrite and cementite [18]. Normally double tempering is adopted in every industrial procedure and the main reason is to due to the complete decomposition of retained austenite. In fact, in large tools not all the retained austenite will be eliminated after the first tempering. The fraction of retained austenite that successfully transforms to ferrite and carbides will deplete the steel from carbon, causing the raising of M_s and M_f temperature and causing more retained austenite to transform to martensite upon cooling. Hence, second tempering cycle is needed to remove this new martensite (sometimes called as fresh martensite) [2]. In some cases a third tempering is used to recover residual stresses after heat treatments. The effect of time and temperature is related by the well known Hollomon-Jaffe parameter expressed by equation 2.1 [19].

$$P = T(20 + log\, t) \tag{2.1}$$

At lower values of P mechanical properties will be higher due to martensite, then as P increases carbon steels will see a decrease in strength and hardness, caused first by loss of martensite and then by microstructure coarsening for higher temperatures.

2.5.3 Carbides in AISI H13

While these series of transformations occur for any carbon steel, in the specific case of the H13, tempering is normally conduced at higher temperatures (between 400°C - 650°C) since the precipitation of specific alloy carbides is researched to withstand working for multiple hours at elevated temperatures. The reason for this is that alloy elements start to diffuse more rapidly at temperatures above 400°C. Carbides are small ceramic materials, based on covalent or ionic bonds, where carbon is bonded in different stoichiometries with transition metals. In every steel carbides are never pure compounds of transition metals and carbon, but Fe is always present. According to temperatures, each type of carbide has a different solubility products as shown in figure 2.7, hence having specific precipitation and dissolution temperatures according to the specific alloy composition. Before deepening on the various carbide typologies in H13 steel, it is important to enlighten that a mixture of carbides of various dimensions (i.e. a certain size distribution curve) is the best solution for improving both abrasion resistance and strength. For the first one, carbides of the size of 1 - 100 μm are the best since they avoid direct penetration of a generic tooling tip (which has compatible dimensions),

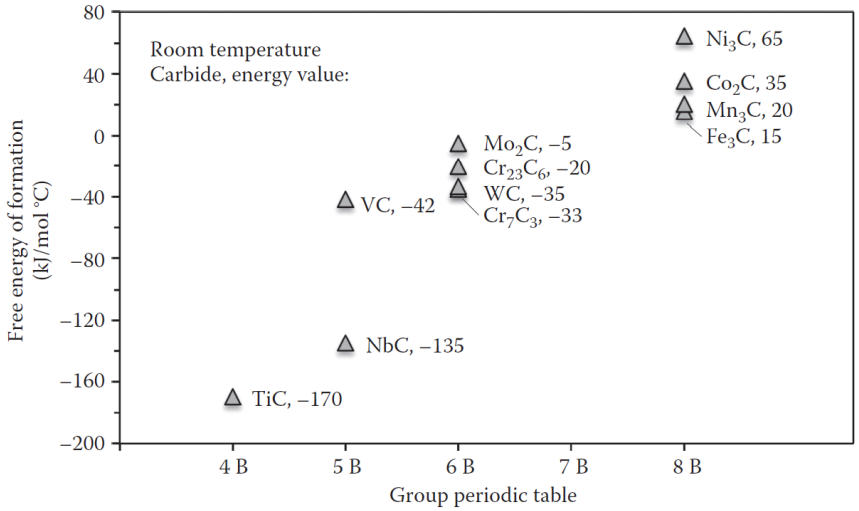

Figure 2.7: Free energy of formation for different carbides of alloying elements in iron at room temperature. Data is presented for 1% activity of the metal. The data represents the decrease of free energy when 1 mol of C is added and forms a carbide in the alloy. The lower the energy, the higher the tendency to form a carbide [2], [20].

while for the second one carbides in the nanoscale are the best to pin dislocations [2]. In other cold-work tool steels, in fact large volume fractions (i.e. 15- 20%) of micrometric carbides are present, which are absent in AISI H13 due to its required toughness. Moreover, large carbides are not the best solution when maximizing adhesive wear resistance, i.e. resistance to loss of material due to welding of two metals when they are pressed together and quickly removed, due to their higher brittleness. The main carbides typologies found to precipitate specifically in the H13 steel according to literature are:

- MC - type carbides: they are V-rich with face-centered cubic structure. They are the most stable alloy carbides (generally being dissolved around 1100°C) in H13 and can be present as undissolved carbides during lower temperatures austenitizing with normally micrometric size. During tempering they precipitate with nanometric size (less than 200 nm). These carbides have the highest strengthening effect, due to greater temperature stability, small size, cuboidal or spheroidal shape and coarsening resistance. Within this family the V_8C_7 carbide is the most present and important, with FCC structure and lattice constant is a = b = c = 0.833 nm [21], [22].

- M_2C - type carbides: they are mainly Mo-rich carbides with hexagonal close packed structure. They are found in less volume fraction than MC carbides due to low Mo content and thermal stability. In H13 steel they are usually

not found at higher tempering temperatures (650°C - 700°C). They can precipitate in small amount during tempering together with M_6C - type [22], [23].

- M_7C_3 - type carbides: mainly Cr-rich. They have hexagonal close packed structure and only present in small traces after tempering of H13. Their contribution to strength is not high due to low concentration. They can transform during annealing to more stable $M_{23}C_6$ [26], or be totally dissolved at lower austenitizing temperatures [25].

- M_6C - type carbides: they are mainly Mo-rich in H13 steel. They are less frequent than MC and $M_{23}C_6$. They can precipitate during tempering together with M_2C - type in large ingots, having however lower contribution to final strength [2], [21].

- $M_{23}C_6$ - type carbides: they are Cr-rich, even if also some Fe-rich type are reported [25], with body-centered cubic cell. They are the second most present type of carbides in H13 steel due to high Cr concentration. They have a low thermal stability and are totally dissolved in austenite during austenitizing above 800 - 850°C [22], [24]. They have lower hardness compared to MC-type carbides and tend to coarsen much rapidly at higher tempering temperatures due to much higher diffusivity of Cr with respect of V. In large ingots, they usually form at the centre where cooling rate is the lowest, where they are found to precipitate at grain boundaries and have sizes of 1 - 100 μm [21].

- M_3C - type carbides: mainly Fe-rich carbides. They have hexagonal close packed structure, and are found also in all carbon steel, named as cementite. They starts forming at lower temperature tempering (200°C - 300°C) and have the lowest contribution to strength and highest coarsening rate. However they have also high free energy of formation with respect to other carbides, meaning that C is not prone to bond to Fe when other carbide forming elements are present [2].

In figure 2.8 a scale of each carbides hardness in steel is shown, compared to martensite, showing the great interest towards MC-type carbides in increasing abrasive wear resistance and mechanical properties even at higher working temperatures.

2.5.4 Effect of Nitrogen on AISI H13 microstructure

In the literature many works have been proposed regarding surface modifications such as PVD or CVD coatings or alloy variations with respect to pure AISI H13

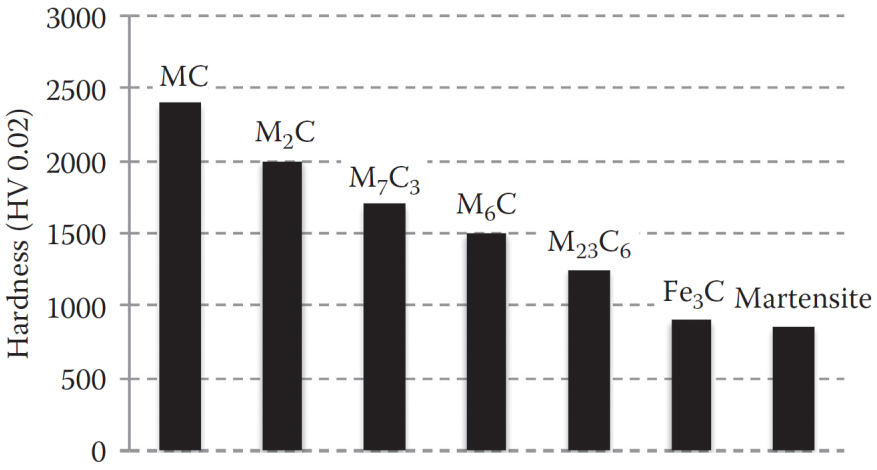

Figure 2.8: Hardness HV 0.02 of various carbides systems present in H13 steel compared to martensite [2].

steel. In this work a section is dedicated to show the effects of relatively small nitrogen additions (about 0.050%wt) with respect to H13 nominal composition, since traces of N are also present in the analysed material due to nitrogen atomization method of the powders, as described in chapter 4. Nitrogen additions have been performed on wrought H13 material by [3], [27], [28], [29] and [30]. Results show that stability of MC-type carbides increases at tempering temperatures showing reduced coarsening, due to presence of N substituting carbon in the new M(C,N) structure rich in V. Moreover, their dissolution temperature increases from 1100°C to about 1300°C [3]. This has a strong effect on the heat treatment, since even at temperatures of 1150 - 1200°C amounts of such carbides can be found. Due to reduced coarsening rate, V(C,N) carbides tend to be smaller compared to previous VC carbides acting as grain refining particles for austenite at common austenitizing temperatures, hence avoiding grain growth [27]. N also promotes complete solution of Cr and Mo. Overall, after quenching and tempering of wrought specimens, even small traces of N (around 0.029 wt%) can improve hardness of 3 - 5 HRC without reducing impact toughness with respect to the standard specified in NADCA #207-2003 [31] for wrought H13 regarding die casting applications, according to [27] and [28]. The effect of N on H13 steel microstructure has been evaluated by a thermodynamic calculation regarding phase stability using Thermocalc software by [3]. In their calculations two alloy systems where considered: a typical composition of H13 steel and a Nitrogen-alloyed H13 steel showed in table 2.3. Calculations show the increased range of thermodynamic stability of V(C,N) with respect to VC. In conclusion, such an alloying strategy can improve thermal stability of AISI H13 steel, allowing elevated performances for a longer service life.

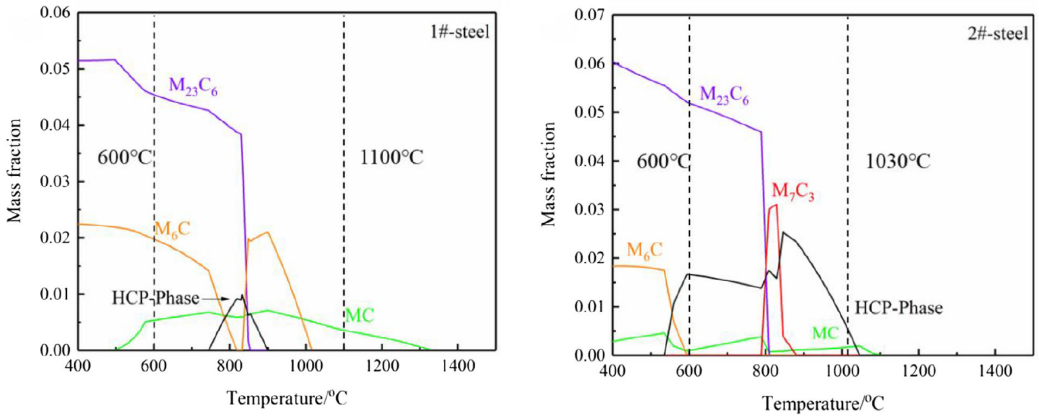

(a) (b)

Figure 2.9: Thermodynamic calculation of phase stability in (a) Nitrogen containing H13 with chemical composition provided in table 2.3, (b) Nitrogen free H13 with chemical composition provided in 2.3 [3].

Table 2.3: Chemical composition of examined steels for thermodynamic calculation and microstructure analysis by [3].

Sample	**C**	**Cr**	**Mo**	**V**	**Si**	**Mn**	**N**	**Fe**
1#	0.32	5.02	2.72	0.70	0.46	0.37	0.059	Bal.
2#	0.40	4.75	2.56	0.66	0.47	0.31	-	Bal.

Table 2.4: Cross reference table of the main hot-work tool steels according to the main national standards [1].

AISI (US)	DIN (Ger)	JIS (Jpn)	BS (UK)	AFNOR (Fra)	SSH (Swe)
Chromium hot-work tool steels					
H10	1.2365, 1.2367	G4404SKD7	4659 BH10	A35-590 3451 32DCV28	...
H11	1.2343, 1.7783, 1.7784	G4404SKD6	4659 BH11	A35-590 3431 FZ38CDV5	...
H12	1.2606	G4404SKD62	4659 BH12	A35-590 3432 Z35CWDV5	..
H13	1.2344	G4404SKD61	4659 BH13, 4659 H13	A35-590 3433 Z4OCDV5	2242
H14	1.2567	G4404SKD4	...	3541 Z40WCV5	...
H19	1.2678	G4404SKD8	4659 BH19	...	...
Tungsten hot-work tool steels					
H21	1.2581	G4404SKD5	4659 BH21, 4659 H21A	A35-590 3543 Z30WCV9	2730
H22	1.2581	G4404SKD5	...	...	...
H23	1.2625	...	...	...	...
H24	...	...	...	...	...
H25	...	...	...	...	...
H26	...	...	4659 BH26	...	...
Molybdenum hot-work tool steels					
H42	...	...	...	3548 Z65WDCV6.05	...

Table 2.5: Chemical composition (wt%) of hot-work tool steels [1].

AISI	**UNS**	**Composition (wt%)**								
Type	**No.**	C	Mn	Si	Cr	Ni	Mo	W	V	Co
Chromium hot-work tool steels										
H10	T20810	0.35-0.45	0.25-0.70	0.80-1.20	3.00-3.75	0.30 max	2.00-3.00	...	0.25-0.75	...
H11	T20811	0.33-0.43	0.20-0.50	0.80-1.20	4.75-5.50	0.30 max	1.10-1.60	...	0.30-0.60	...
H12	T20812	0.30-0.40	0.20-0.50	0.80-1.20	4.75-5.50	0.30 max	1.25-1.75	1.00-1.70	0.50max	...
H13	T20813	0.32-0.45	0.20-0.50	0.80-1.20	4.75-5.50	0.30 max	1.10-1.75	...	0.80-1.20	...
H14	T20814	0.35-0.45	0.20-0.50	0.80-1.20	4.75-5.50	0.30 max	...	4.00-5.25	...	...
H19	T20819	0.35-0.45	0.20-0.50	0.20-0.50	4.00-4.75	0.30 max	0.30-0.55	3.75-1.50	1.75-2.20	4.00-4.50
Tungsten hot-work tool steels										
H21	T20821	0.26-0.36	0.15-0.40	0.15-0.50	3.00-3.75	0.30 max	...	8.50-10.00	0.30-0.60	...
H22	T20822	0.30-0.40	0.15-0.40	0.15-0.40	1.75-3.75	0.30 max	...	10.00-11.75	0.25-0.50	...
H23	T20823	0.25-0.35	0.15-0.40	0.15-0.60	11.00-12.75	0.30 max	...	11.00-12.75	0.75-1.25	...
H24	T20824	0.42-0.53	0.15-0.40	0.15-0.40	2.50-3.50	0.30 max	...	14.00-16.00	0.40-0.60	...
H25	T20825	0.22-0.32	0.15-0.40	0.15-0.40	3.75-4.50	0.30 max	...	14.00-16.00	0.40-0.60	...
H26	T20826	0.45-0.55	0.15-0.40	0.15-0.40	3.75-4.50	0.30 max	...	17.25-19.00	0.75-1.25	...
Molybdenum hot-work tool steels										
H42	T20842	0.55-0.70	0.15-0.40	...	3.75-4.50	0.30max	4.50-5.50	5.50-6.75	1.75-2.20	...

Chapter 3

Additive manufacturing of AISI H13 tool steel

This chapter deals with the topic of Additive Manufacturing in the contest of tool steel. In particular a brief introduction is given to this topic, before dealing with the most important Additive Manufacturing techniques specific to AISI H13 tool steel.

3.1 Introduction on Additive Manufacturing

This chapter has the aim of introducing the new challenges and perspective linked to the manufacturing of H13 tool steel components, by focusing on the newest technological possibilities in the field of metal forming technologies, i.e. Additive Manufacturing (AM). Traditional manufacturing processes of tool steels have the disadvantage of containing a stage where liquid metal is cast into an ingot, thus having low cooling rates in various positions of the ingot and strongly promoting segregations, grain growth and grain boundary precipitation of deleterious phases. Despite the evolution of casting technologies, i.e. the diffusion of ingot remelting processes to obtain more controlled and finer microstructures, cooling rates remain too low to completely avoid such problems. In this context, the adoption of Powder Metallurgy (PM) for manufacturing high quality metal products, such as various typologies of tool steels, revealed as a success. According to [12], PM is the branch of metallurgy which deals with the manufacture of powders or metal components made from those powders. The main reason for its success is its capability of manufacturing products with at least the same mechanical performances but with higher toughness due to a much finer microstructure. As an example, the effect of carbides size when one of them acts as a crack initiating factor on bend strength is shown in figure 3.1. In the figure taken from [2] also three microstructures are

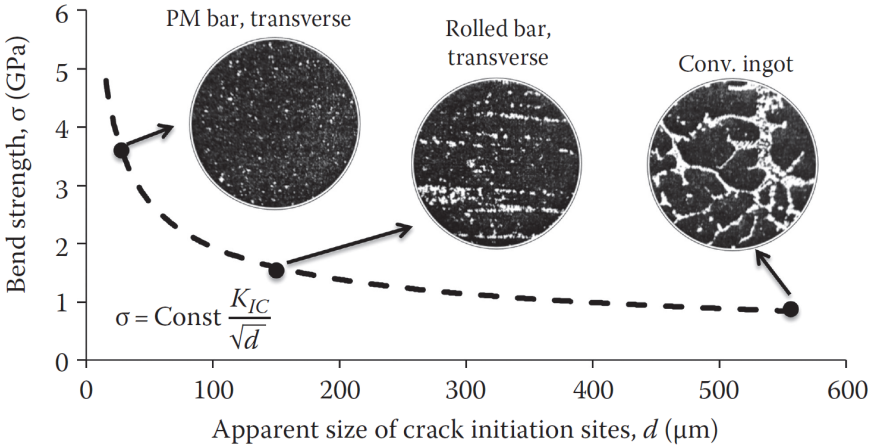

Figure 3.1: Effect of carbide size on flexural strength of steels when one of them acts as a crack initiating factor. Three examples of microstructures are shown, i.e. one coming from a PM bar, one coming from a rolled bar and one coming from a conventional ingot [2].

shown coming from three different metallurgical products coming from the same steel (i.e. same carbides content): an ingot obtained through conventional casting technologies where carbides are precipitated at grain boundaries forming a continuous network, a rolled product where mechanical actions have broken carbide networks leaving 1D structures along the rolling direction, a PM product where carbides are finely dispersed particles. Furthermore, PM has allowed to manufacture components which were not accessible in the same way with traditional processing. In the tool industry this is the case of WC-Co or cemented carbides which cannot be produces through casting routes due to their peculiar microstructure [32]. Established PM technologies are the Press and Sinter (P&S), Metal Injection Molding (MIM), Hot or Cold Isostatic Pressing (HIP or CIP), Field Assisted Sintering Technology (FAST). Most of them share in common a sintering step where high temperatures (below the melting temperature) are used to favour diffusion processes to bond particles together.

Among the various technologies belonging to the set of Powder Metallurgy Additive Manufacturing (AM), is a set of processes involving the addition of material to obtain the final shape and not the subtraction. In general, this approach allows to obtain lower material wastes and more complex shapes with respect to subtractive techniques [33]. Raw material is provided under the form of a powder of a wire and is melted or bonded layer by layer starting from a 3D model simply created on a Computer-Aided Design (CAD) file. Another basic consideration that is always made is the relationship between part cost and complexity. In traditional manufacturing cost is directly proportional to complexity [34], since internal cavities

and features need additional tooling and machining. In AM complexity is almost for free, in fact the only two factors that change are print time and amount of material used to provide any support structure and the final part can be produces in near-net shape [35]. Therefore, components such as molds, with internal cooling channels are perfect candidates for such manufacturing processes, since machined channels need to have simple shapes, limited by tooling handling and geometry. With the adoption of AM, cooling channels may be perfectly conformal to the shape of the molded part, improving cooling efficiency with benefits on process times and mold life [36], [37]. Product design with AM is peculiar with respect to traditional design for manufacturing and requires in depth knowledge on various aspects, usually including a well planned Design of Experiment (DoE) phase. In general the process is divided in several steps [35]:

- Product design: the AM part is designed through a CAD software generating a 3D model containing all product features.
- File conversion: the file is converted into standard tessellation language (STL) to be read by the machine. Then it is divided in many 2D slices which will used to generate the G-code, addressing tool movement of AM machine.
- AM machine configuration: before operating, process parameters need to be set. These parameter are material-specific and sometimes part specific (such as layer/wall thickness).
- Print: Then printing phase begins. For larger parts printing is the most time-consuming stage (form hours to days).
- Part removal: the part is removed from the platform or the building chamber. Sometimes this requires additional machining.
- Post processing: additional machining for final surface finishing, heat treatment stages or other specific post-processing relative to the AM technology are performed to obtained the completed part with final characteristics.

Due to its nature, economical feasibility of AM needs to be studied according to the specific case, to determine whether it can substitute or not traditional processes.

3.1.1 AM techniques for metals

Before 2017 a complete classification of AM techniques was not present in literature, therefore different nomenclature was given to the same process. Nowadays, according to the ASTM/ISO 52900:2017 [38], there exist four categories of AM

processes (between the total seven described by the standard) relative to metal AM:

- Material Extrusion (MEX): AM process in which material is selectively dispensed through a nozzle or orifice. For metal parts, feedstock is in the form of a wire made of metallic powders bound in a polymeric matrix. After the printing phase, the part needs to go through a de-binding step to remove the polymer and sintering to achieve full density.

- Binder Jetting (BJT): AM process in which a liquid bonding agent is selectively deposited to join powder materials. Binder deposition is carried out in 3D and helps metal powders stick together. With the deposition of every layer a UV or heated lamp cures the binder. In the end, also here a de-binding and sintering step are performed.

- Power Bed Fusion (PBF): AM process in which thermal energy selectively fuses regions of a powder bed. After Loose powder is distributed evenly on a powder bed, a high power beam melts or sinters them selectively proceeding layer by layer.

- Directed Energy Deposition (DED): AM process in which focused thermal energy is used to fuse materials by melting as they are being deposited. Feedstock material can be in the form of powder or wire and is directed towards the energy source, melting and creating a pool which then solidifies.

As far as tool steels are concerned and more specifically the AISI H13 hot-work tool steel, that remain the focus of this work, the three AM techniques that are more studied in literature are Laser-PBF (LPBF), also called Selective Laser Melting (SLM), using a laser beam source compared to other energy sources, Electron-PBF (EPBF), also called Electron Beam Melting (EBM) in the present work, which in contrast uses an electron beam and DED techniques such as Laser metal deposition (LMD or LDED) and Wire Arc-AM (WAAM) [39]. All this fusion based techniques have in common the local melting of small amounts of material which then is rapidly solidified layer by layer. The repeated addition of thermal energy which is provided along the building direction, conventionally called z direction (normal to the build platform), usually brings to an anisotropic microstructure in the as-built components with columnar grains along z [40]. In the next sections a more detailed description of theses techniques and their application in this context is provided.

3.2 DED principles and mechanisms overview

Directed Energy Deposition (DED) directly evolves from traditional welding technologies such as traditional cladding. Together with its usage to manufacture near net shape parts, DED is adopted to repair components or modifying their surface functional properties. The principle within DED is to direct the feedstock material in the form of a metal wire with diameter of 1 - 3 mm or a powder (which can be water atomized, i.e. with irregular shape and strongly cutting costs) in the range of 50 - 200 μm, directly towards the energy source [35]. DED processes have a higher deposition rate with respect to PBF processes, but also higher layer thickness, surface roughness and higher minimum feature size, often compromising the manufacturing of very thin features. Furthermore, they have a relatively simple machinery, allowing possible process hybridization or even the possibility to manufacture components made of multiple materials [41]. There are several possible energy sources in DED machines, giving them a certain grade of specificity with respect to the metal alloys. Most common ones are Laser Directed Energy Deposition (LDED) processing powders, while metal wires can be processes through Wire Arc-AM (WAAM) and Electron Beam-AM (EBAM) machines. According to the type of machine the melting principle changes: for powder based systems a number of nozzles (which can be coaxial or lateral) directly spray the powder using a shield gas, normally Ar, onto the melt pool where the energy is directed, melting it. The liquid is rapidly cooled down at extremely high rates around 10^3 - 10^5 °C/s. At the bottom of the melt pool a Heat Affected Zone (HAZ) of material will incur a rapid heat cycle. The energy source is moved by a Computer Numerical Controlled (CNC) robotic arm, following a pre-set path together with the build plate which may rotate, hence allowing more degrees of freedom. A schematics of a DED machine principles is reported in figure 3.2 with courtesy of [35] and [42]. DED technologies allow to manufacture relatively large components, with higher deposition rates than all PBF processes, moreover their success is also given by the possibility of repairing damaged components [35]. However, defects such as Lacks of Fusion (LoF) due to insufficient energy, keyholing due to material vaporization caused by too high energy, gas entrapment, cracking and delamination due to residual stresses are very common in DED components. The possibility of relatively economic feedstock material, the high scan speed and material deposition rate with the absence of expensive technologies such as vacuum, make DED a much more economic choice with respect to PBF, in cases where roughness and geometrical accuracy are not fundamental, making it suitable for manufacturing or repairing larger and complex parts in automotive, aerospace and military sectors.

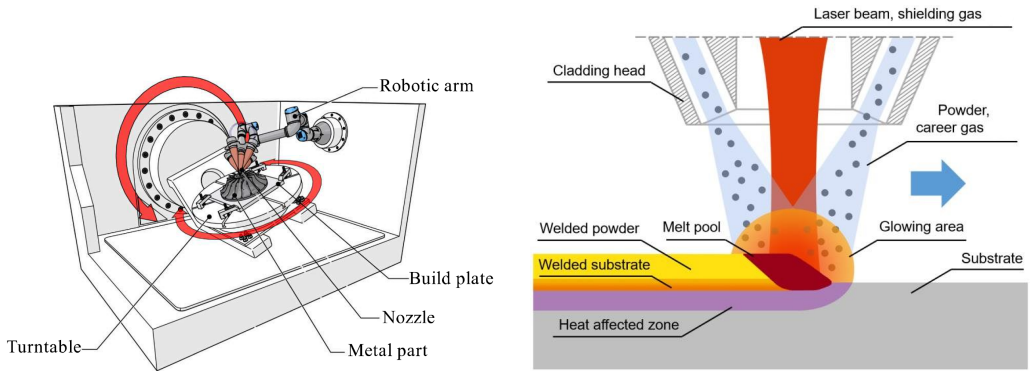

Figure 3.2: (a) General schematics of a LDED machine using powder feedstock [35], (b) Powder melting schematics showing the melt pool, the welding area and HAZ [42].

3.2.1 DED of AISI H13

As anticipated in 3.1.1, additive manufacturing of H13 tool steel has been mainly investigated using LDED by [40], [43] and [44] and WAAM by [45] and [46]. In the case of LDED a older work was made by [47]. Results have shown that the specific thermal history of the material is crucial in the determination of final microstructure. Normally, both LDED and WAAM H13 steels show gradient hardness going from the top layer to the bottom layers due to prolonged high temperature dwell time of the latter ones. In LDED, parameters such as laser power, beam speed and laser cross sectional area will influence the geometry of the melting pool. Other process parameters such as the type of shield gas, deposition rate and scanning strategy will influence the quality of manufactured parts in terms of porosities, LoF, residual stresses, distortions and cracks. The specific thermal history of a single point has been studied and simulated by [43], showing that after the first melting and rapid cooling to austenite, temperature lowers until reaching M_s, i.e. the martensitic transformation occurs. Later on, the material will experience a number of thermal oscillations. In particular a second laser passage may lead to a remelting or to a transformation to austenite phase according to its energy and focus distance. Subsequent laser passages will lead to tempering of martensite and to formation of bainitic structure, therefore a decrease in martensite and retained austenite formed earlier will happen. The LDED as-built microstructure of H13 has proved to have cellular morphology due micro-segregation phenomena with average cell dimension around 10 - 30 μm [40]. A SEM micrograph of LDED H13 by [43] is shown in figure 3.3 where three different configurations of laser power and speed are used. They have been joint in a unique parameter called laser fluence, together with beam cross section. These micrographs show the elongated shape of

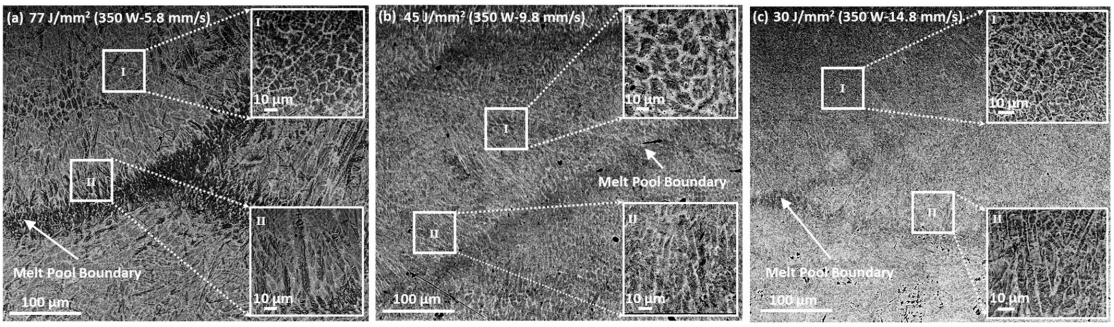

Figure 3.3: SEM micrographs of LDED H13 with three laser fluences, cellular and elongated structures are shown in the centre and at the melting pool respectively [43].

cells near the melt pool boundary due to heat flux direction and the more equiaxial shape in the centre caused by rapid cooling. This cell-type microstructure is happening since during solidification alloy elements such as Cr, Mo, V are pushed in the liquid due to their lower diffusivity, therefore their concentration is higher in the boundary region between cells and will tend to stabilise retained austenite. Later passages will also lead to the formation of carbides at the cell boundaries.

WAAM manufacturing works through a similar principle with respect to LDED. The main two differences are the even higher material deposition rates, due to usage of a wire instead of blown powder, and the usage of an electric arc as energy source. In figure 3.4 a simplified scheme of WAAM apparatus is presented. The adoption of electric arc brings the melt pool and therefore the width of a single track to generally have larger dimensions, i.e. bringing to higher minimum feature sizes. For example, in the case of [46], the track width was 8.72 mm with a distance between adjacent tracks of 5.50 mm, while in the case of [43] (using LDED) the pool width (indicative of the track thickness) was 1.2 mm in the case of 77 J/mm^2 of laser fluence. WAAM H13 microstructure is similar to LDED one. Also in this cases a cellular/dendritic microstructure is found in the as-built material with slightly larger dimensions with respect to LDED, with retained austenite at boundary regions enriched in C, Cr, Mo and V, which shifted M_s temperature below room temperature. The inner region was mainly martensitic/bainitic and shows the signs of thermal cycles due to multiple passages and a heat sink effect due to heat exchange. Mechanical properties of LDED and WAAM parts are anisotropic showing greater strength along the deposition direction (x-y plane) with respect to the building direction (z axis) [41] and having higher brittleness with respect to traditionally manufactured H13 coming from heat treatment. Microhardness of H13 samples produced with LDED showed values around 600-700 HV at the top layers and of 500 - 550 HV at the bottom [43]. In general LDED allows to obtain finer and denser microstructure with respect to WAAM due to

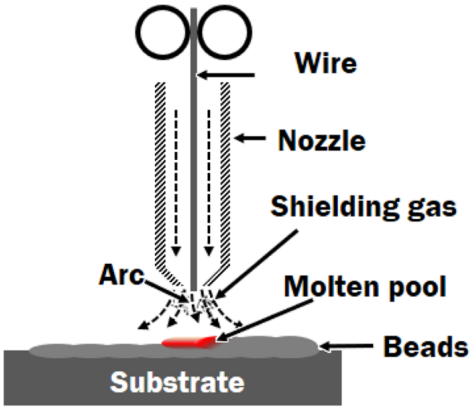

Figure 3.4: Simple schematics of coxial wire feeder WAAM precess by [41].

Table 3.1: Main representative characteristics of LDED and WAAM processes with typical values, adapted from [41].

Process	**Typical layer thickness [mm]**	**Minimum feature size [mm]**	**Heat flux density [W/mm^2]**	**Energy efficiency [%]**	**Deposition rate [g/min]**
LDED	0.2 - 0.5	0.38 - 1	$\approx 10^6$	$< 40\%$	< 8.3
WAAM	1 - 2	1 - 2	$\approx 10^4$	$< 90\%$	16.7 - 66.7

the higher cooling rates (smaller melt pool dimensions), while WAAM presents higher material usage efficiency and cost-effectiveness [49]. In table 3.1 a comparison between main characteristics of LDED and WAAM are reported, taken from [41].

In conclusion, the large amount of retained austenite and residual stresses upon fast cooling, delamination effects, low geometric tolerances and high surface roughness strongly limit the application of DED H13 materials. Further studies need to be assessed upon effects of heat treatments to reach standard levels for tooling applications.

3.3 PBF principles and mechanisms overview

In the latter years Powder bed Fusion processes (PBF) have received great interest to manufacturing complex geometric parts achieving near full density. PBF machines are rather complex and more expensive with respect to DED equipments, but allow to obtain higher quality results under many different perspectives. There two main power source typologies in PBF machines: laser beams and electron

beams giving name to different technologies. Laser beams can be used to selectively melt of sinter the powders while electron beams, being are used to melt only, having more power. Laser based PBF or LPBF also called Selective Laser Melting (SLM) or Selective Laser Sintering (SLS), while electron based PBF or EPBF are also called Electron Beam Melting (EBM). In the generic case of a LPBF machine, feedstock powder is charged into a powder store and then transferred into the building chamber, working in inert atmosphere, by a re-coater which evenly distributes it across the bed. After the layer has been deposited, the beam selectively melts or sinters it and the bed moves in the negative z direction to allow the next layer to be worked. Usual cooling rates of PBF systems are 10^5 - 10^7 °C/s which are far greater than DED systems, allowing finer cooling microstructures [35]. A schematics of a SLM machinery is shown in figure 3.5. Powder feedstock for PBF processes have strict requirements in terms of flowability and size range. This is a great difference compared to DED powders which may be irregular, hence water atomized. In PBF gas or plasma atomized powder are needed, increasing feedstock costs, hence many studies focus on the possibility of recycling powders. SLM and EBM are the two main processes for the manufacturing of H13 components. In the case of SLM a laser source is mechanically controlled. The build chamber works in inert atmosphere (Ar or N_2) and the required powder size is between 15 - 63 μm. SLM machines offer the possibility of applying a preheating to the powder bed, reaching temperatures until 200°C - 400°C to reduce thermal stresses, which indeed are extremely high due to rapid cooling, causing distortions and crack opening [50]. SLM technique is generally the most adopted one for manufacturing H13 due to relatively high geometrical accuracy, low surface roughness, relatively fine final microstructure and lower cost with respect to EBM. A graph showing the typical thermal cycle of a SLM material is provided in figure 3.6.

On the other hand, EBM machinery requires a rather complex apparatus and a smaller number of producers are present on the market. The typical EBM machine is composed by the an electron beam unit (similar to the one in SEM microscopes) and a building chamber. In the first unit a cathodic heated filament generates electrons which are accelerated, focused and deflected by subsequent magnetic lenses, therefore no mechanical control is adopted [51]. The process takes place in vacuum (usually around 10^{-3} Pa), even if small amount of He are used to better cool down and dissipate the charge which is built. Feedstock powder needs to be spherical and in the range between 45 - 150 μm. This technology allows to apply a strong bed preheating through a series of defocused beam passages at high power and speed ($1.5 \cdot 10^4$ mm/s). This provokes partial powder sintering, even reaching temperatures between 750°C - 1100°C, to reduce powder spreading during the primary melting action and to reduce temperature gradients in the part, strongly influencing the final microstructure [51]. Many high carbon steels

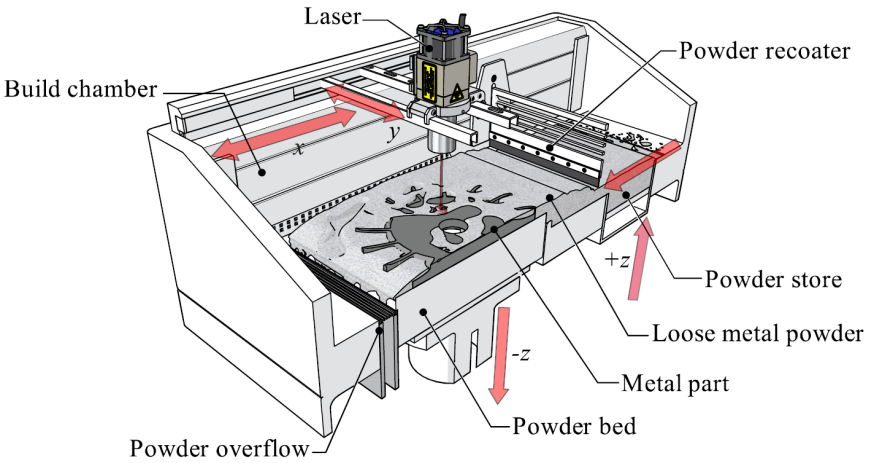

Figure 3.5: Simple schematics of SLM machinery. A powder store platform rises to allow new powder to be spread across the bed by a recoater. A laser is mechanically controlled and directed to specific points defined by a control algorithm by [35].

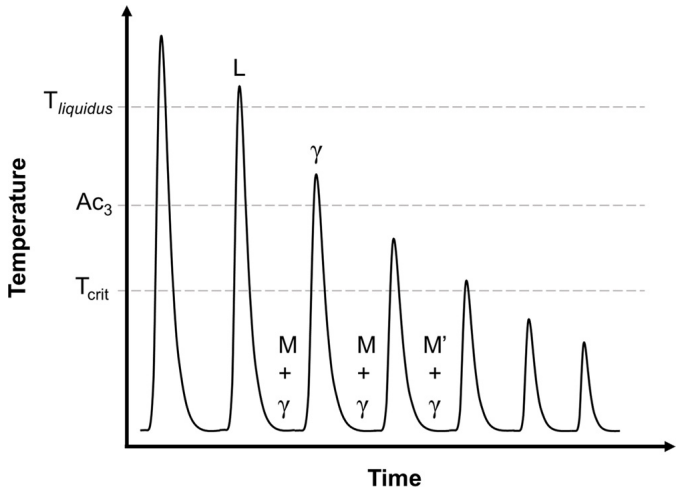

Figure 3.6: Simplified representation of a SLM thermal cycle of a H13 steel. Phase transformation temperatures are reported. T_{crit} is the last temperature that triggered tempering effects, above which the microstructure does not change in a particular manner. L is liquid phase, γ is austenite, M is martensite, M$'$ is tempered martensite [55].

(as brittle materials) have been successfully processed with EBM obtaining crack and porosity free specimens even with higher scan speed [52], [53]. Compared to SLM, EBM process involves higher beam power. Moreover the use of accelerated electron vs photons slightly changes the mechanisms of heat transfer. In fact, higher layer thickness and coarser powder are used in this case, since kinetic energy of electrons allow for higher penetration with effects such as remelting of two or

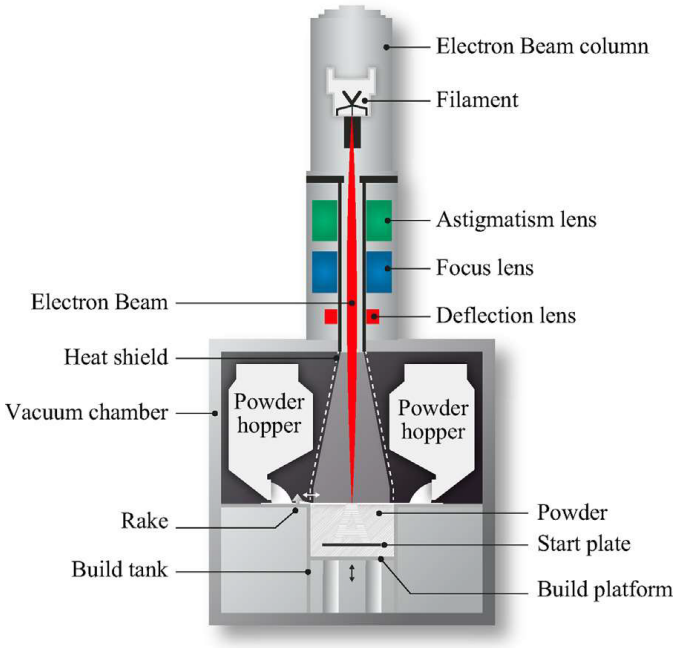

Figure 3.7: Schematics of the Arcam EBM machine made up an electron beam column containing the cathode filament and three types of electromagnetic lenses and a building chamber with powder hoppers, build platform and build tank by [51].

more layers [54]. The use of coarser powder reduces surface quality, but ensures higher productivity.

3.3.1 SLM of AISI H13

SLM of H13 tool steel has been studied by a high number of publications in latest years, successfully obtaining fully dense structures with various combinations of process parameters. The final as-built microstructure consists of the typical fine cellular/dendritic solidification pattern, where C and alloy elements such as Cr, Mo and V are mostly concentrated at cell walls made of retained austenite around martensite [55]. The typical dimension of the SLM cellular structure is around 0.6 - 1 μm, hence much finer than in the case of LDED and WAAM [56]. Retained austenite levels are found to be around 16.5 - 29.7% by [55]. This levels are not acceptable for tooling applications, therefore heat treatment is necessary. Small traces of nanometric carbides are found in the HAZ below each melting tracks, even if their content is lower with respect to DED H13 parts [39]. From the morphological point of view, effects such as keyholes and protrusions can occur when the laser power is too high, causing molten material to accumulate on the borders. In case of too low laser powers, LoF are found reducing overall density. LoF may

also occur at higher scanning speed if the laser has not enough time to completely melt the powder. SLM H13 parts incur important residual stresses generated by the rapid heating and cooling cycles, that can locally overcome the yield limit (YL) causing part distortion or the ultimate tensile strength (UTS) causing crack opening. Normally, when a new melted layer is rapidly cooled down, its contraction will be much greater than bottom layers cooling more slowly. This will result in tensile stresses in the new layer and compressive stresses in the bottom ones [54]. Preheating is a strategy to mitigate the overall temperature difference between the melt and the part, hence reducing residual stresses. Preheating procedures allow to avoid plastic distortions and cracks formed due to such intense stresses. Moreover, they can lower the required laser power, reducing porosities at higher scanning speed since part of the energy required for melting is given as thermal energy from the bed, hence lowering process time [56]. Other variables may affect the thermal cycles seen by the material, represented in figure 3.6, such as layer thickness and hatching distance, determining the zones of partial remelting and the intensity of later heat pulses. The microstructure will evolve as a consequence of the thermal cycles until temperature is lower than a certain T_{crit} (in the ferritic field) when no more evident microstructural change will occur, due to available energy lowering down. In conclusion, fully dense and uncracked SLM H13 parts have showed to posses similar or to even exceed static properties as wrought H13 parts in terms of tensile strength and hardness, due to finer microstructures. However, they lack in ductility and fatigue strength [39]. This is mainly caused by internal defects and high residual stresses. In most cases heat treatments to reach better homogenization, reducing retained austenite and residual stresses are needed [57].

3.3.2 EBM of AISI H13

The manufacture of AISI H13 through EBM has received less attention with respect to SLM in the literature. In EBM, higher powers and electromagnetic deflection lenses controls allow to reach much higher scan speeds and the possibility of higher temperatures preheating overcoming 1000°C. This last aspect has two main effects: the pronounced reduction of inner residual stress with consequent reduction in delamination and cracking and the disappearance of the cellular/dendritic microstructure typical of SLM and DED as shown by [58], [59] and [60]. In particular, a needle-like microstructure is found in H13 specimens with preheat temperature of 920°C. An example of as-EBM H13 microstructure taken using BSD imaging mode in SEM is shown in figure 3.8. This morphology indicates the presence of martensite and bainite, while retained austenite reached levels around or below 5% (usually near to the measurement error). A rather high level of homogenisation is evident, due to the long permanence at high temperatures. Thermal history in EBM is completely different from to SLM one. In fact, rapid cooling occurs in the

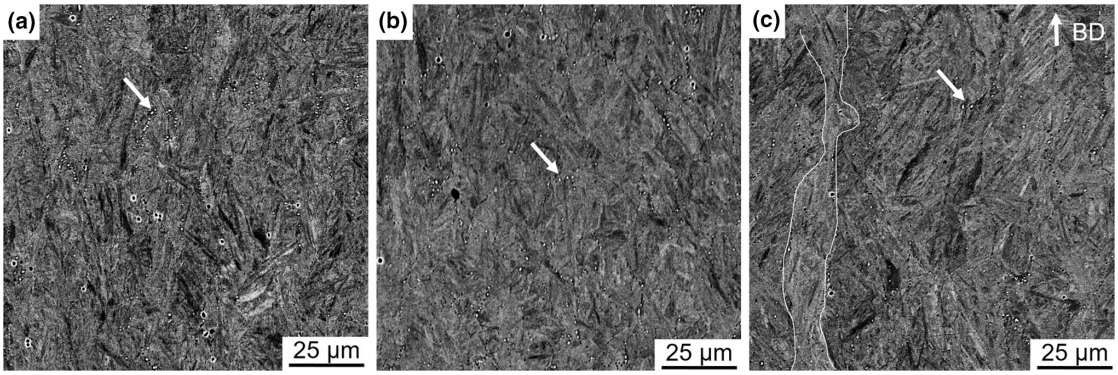

Figure 3.8: BSD micrograph of as-EBM AISI H13 processed with three different increasing volume energies and preheat of 920°C, showing martensite/bainite microstructure. Carbide precipitation is indicated. In case (c) of higher energy, columnar structures are enlightened by [58].

melt pool as in SLM, but overall thermal gradient is lowered due to higher preheat. The same spot will face a number of heat cycles due to subsequent remelting with a following long dwell time around the preheat temperature or slightly below. This phase is crucial for determining the final microstructure. In H13 specimens temperatures around 1000°C bring the material in the austenitic field, allowing the formation of VC carbides (the only ones stable). In [58] He gas is used to finally cool down the parts, hence rather slow cooling rates are employed. This has brought to bainite and martensite formation with hardness levels between 500-580 HV increasing along the building direction. The influence of preheating can be seen also considering the work by [61], where preheat temperature of 794°C was used and cellular/dendritic morphology was found in EBM H13 specimens, similar to SLM microstructures. This is caused by the higher thermal gradient, which resulted in faster cooling and less alloy element diffusion. Moreover, dwell time at 794°C, even in austenitic range was not enough to bring the same level of homogenisation as in [58].

Chapter 4

Experimental method

4.1 Introduction and Objectives

In this chapter, an extensive description of the followed experimental procedures is presented. The aim of this experimental work has been the characterization of an as-built EBM hot-work tool steel and the study of the effects of different heat treatment conditions, in terms of quenching and tempering, on its microstructure and mechanical properties. The raw materials employed are commercial powders characterised with nominal chemical composition equivalent to an AISI H13 steel. The steel powders were gas atomized with nitrogen, thus causing a nitrogen intake in the powders compared to wrought materials. Specimens coming from two EBM printing jobs, named as job 5 and job 7, delivered form a previous work by [4] have been analysed. In the first job a study on the correct process parameters has been performed, while in the second a series of specimens was produced to study the effect the heat treatments on the EBM as-built material. After a first analysis of the effect of different austenitizing temperatures (1025°C, 1050°C, 1075°C, 1100°C) on the as-built material, two series of specimens were austenitized for 30 minutes in vacuum at temperatures of 1050°C and 1100°C respectively, followed by gas quenching. The tempering curve was obtained after a two hours double tempering treatment at temperatures between 400°C and 650°C. The effect of quenching and tempering has been evaluated on the microstructure through OEM and SEM analysis, with particular reference to the evolution of the carbide size distribution curve, obtained through image analysis.

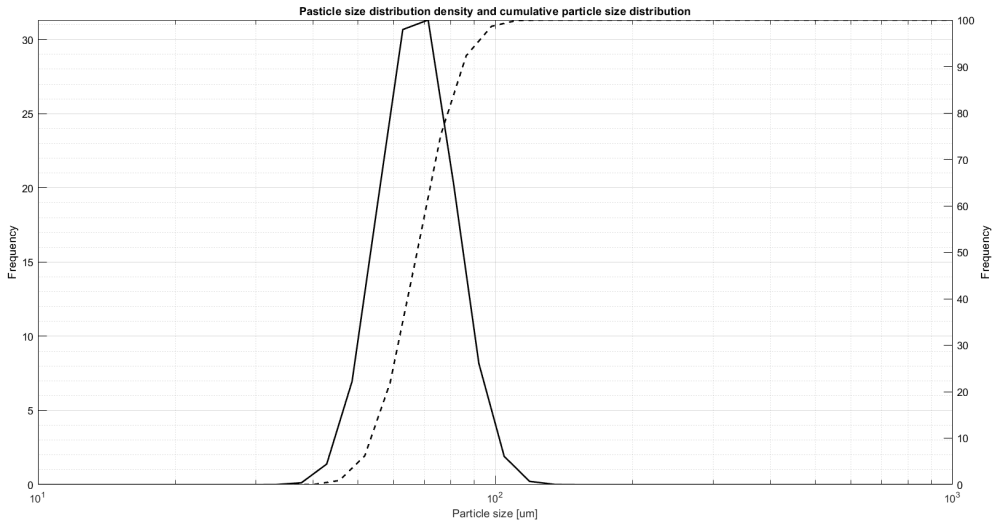

Figure 4.1: AISI H13 powder particle size distribution with cumulative (CSD) in dashed line and distributive (PSD) curve in continuous line, provided by [4].

4.2 AISI H13 powder feedstock assessment

The powder feedstock material derives from a set of commercial powders provided by Sandvik A.B. and nitrogen atomized. The nominal chemical composition corresponds to the standard AISI H13 hot-work tool steel provided in table 2.5 [62]. In a former work [4], the powders were analysed through Optical Emission Spectroscopy (OES), combustion analysis through Leco CS and gas IR spectroscopy through Leco ONH to evaluate their exact chemical composition. Moreover, in the same work their particle size distribution curve was obtained through laser diffractometry to provide a complete characterisation before the printing phase. Data provided by these analysis was taken as a basis from which this work started. In figure 4.1 and table 4.1 the AISI H13 powder particle size distribution is reported, while in table 4.2 their chemical composition is shown. From elemental analysis the presence of about 0.055 wt% of nitrogen emerged as distinguishing factor with respect to the nominal AISI H13 chemical composition. As deeply described in chapter 5, the presence of nitrogen influences the stability of austenite phase and MC carbides, modifying the response of the material to heat treatment. This is the reason why it is necessary to study and tune the heat treatment procedure to ensure the highest possible quality standards.

Table 4.1: Characteristic diameters relative to AISI H13 atomized powder, provided by [4].

Powder	**D10** [μm]	**D50** [μm]	**D90** [μm]	**Mode** [μm]
H13	53.3 ± 0.28	67.1 ± 0.42	84.95 ± 0.07	66.75 ± 0.92

Table 4.2: AISI H13 powder chemical composition obtained from OES and elemental analysis light elements (CS and NOH), provided by [4].

Powder	**C** [**wt%**]	**Mn** [**wt%**]	**Si** [**wt%**]	**Cr** [**wt%**]	**Mo** [**wt%**]	**V** [**wt%**]	**N** [**wt%**]	**O** [**wt%**]	**S** [**wt%**]
H13	0.349	0.31	0.8	5.01	1.7	1.04	0.055	0.019	0.006

4.3 EBM printing

The EBM printing stage of the specimens was performed in the same former work [4] by a A2X Arcam EBM (GE Additive) machine at an accelerating voltage of 60kV in a He partial pressure of $2 \cdot 10^{-3}$ mbar. A total of three printing jobs were performed, namely job 5, job 6 and job 7. The processing window was defined in job 5, where 16 cubic specimens with side length of 18 mm were built, each one with a combination of different scan speeds and beam current were used. Other process parameters were set as constant, such as platform preheat temperature (PT) at 1040°C±10°C, focus offset (FO), i.e. the current applied to shift the electron beam focal plane with respect to the powder bed changing the spot size, at 15 mA, line offset (LO), i.e. the distance between two scan lines at 0.2 mm. With respect to the work in [4] where the baseplate preheat temperature was 750°C, in this case the value of 1040°C was chosen to reduce carbides precipitation. In table 4.3 the whole process parameters regarding job 5 are reported while in figure 4.2 the 16 printed cubic specimens are shown. After a density and inner porosity investigation, which included the design and validation of a complex predictive model to relate the results of Non-Destructive Techniques (NDT) and surface visual inspection with internal defects [63], two specific process parameters have been chosen for carrying on two additional jobs, i.e job 6 based on the parameters of sample 15 of job 5 (i.e. beam speed of 4000 mm/s and beam current of 16 mA) and job 7 based on the parameters of sample 13 of job 5 (i.e. beam speed of 2000 mm/s and beam current of 16 mA). In both cases a series of 10 specimens with dimension $15 \times 15 \times 60$ mm were built using the merge function which allows to keep the same parameters even when the beam rotates. Job 6 and job 7 specimens are shown in figure 4.3. The specimens have been then cut off from the baseplate using EDM.

Table 4.3: EBM process parameters used in job 5 by [4]

Sample	**Side length [mm]**	**Focus offset [mA]**	**Line offset [mm]**	**Beam current [mA]**	**Beam speed [mm/s]**	**Number of scan lines**
1#	18	15	0.2	10	2000	90
2#	18	15	0.2	10	3000	90
3#	18	15	0.2	10	4000	90
4#	18	15	0.2	10	5000	90
5#	18	15	0.2	12	2000	90
6#	18	15	0.2	12	3000	90
7#	18	15	0.2	12	4000	90
8#	18	15	0.2	12	5000	90
9#	18	15	0.2	14	2000	90
10#	18	15	0.2	14	3000	90
11#	18	15	0.2	14	4000	90
12#	18	15	0.2	14	5000	90
13#	18	15	0.2	16	2000	90
14#	18	15	0.2	16	3000	90
15#	18	15	0.2	16	4000	90
16#	18	15	0.2	16	5000	90

The thermograms of job 6 and job 7, obtained using a thermocouple in contact with the baseplate, are provided in figure 4.4. From the metallurgical point of view every specimen coming from job 5 can be considered equivalent. This is due to the fact that scan speed and beam current have an influence only on internal defects and building time. The thermal cycle undergone by the samples is almost identical, apart from relatively small variations in total dwell time at 1040°C. For job 6 and job 7 the larger dimensions of the samples lead to a much higher high temperature dwell time, since the overall job lasted longer (4.5 hours for job 6 and 6.5 hours for job 7). Therefore, an important effect of grain coarsening as well as carbides precipitation due to slow cooling (about 6 hours for both) is measured as shown in chapter 5.1.

4.4 Metallographic characterization

Several specimens have been obtained from job 5, job 6 and job 7 through a series of manual cuts. Samples were analysed both in the as-built state and in the heat treated state, to fully characterize the evolution of the microstructure. The

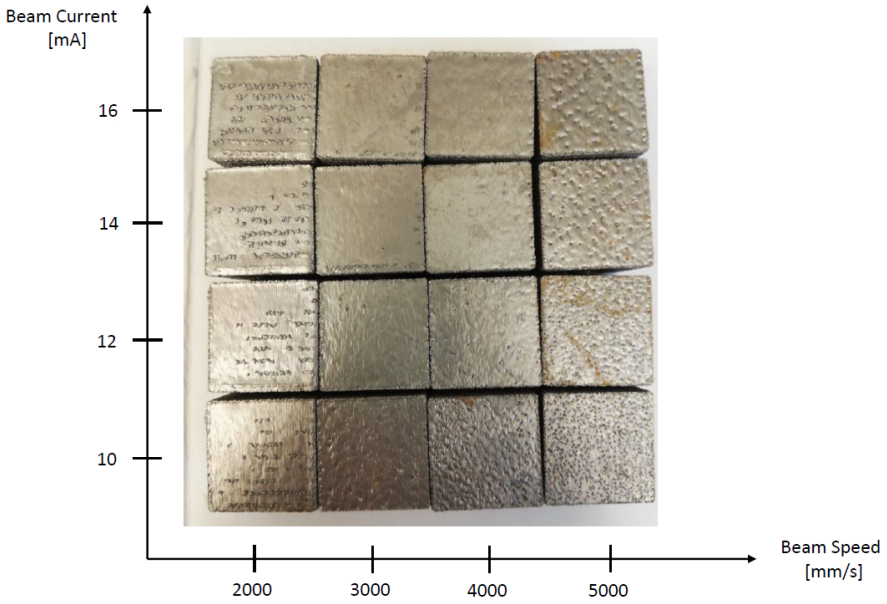

Figure 4.2: The 16 cubic specimens with side of 18 mm built in job 5, provided by [4].

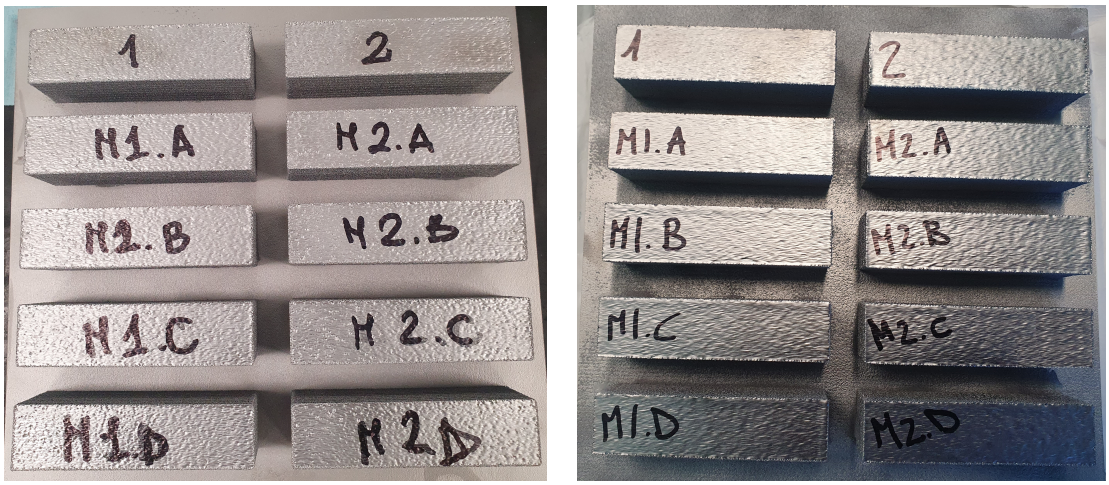

(a) (b)

Figure 4.3: Photos showing (a) specimens built in job 6, (b) specimens built in job 7.

samples j6-M2B and j7-M2B were analysed as a representative of job 6 and job 7. Two cuts have been performed along the z axis (building direction), and the surfaces have been observed. Consequently, they were mounted in a thermosetting resin for metallographic preparation and grounded starting from SiC sandpapers until 2400 grit. Finally, they were polished until 1 μm with polishing cloths with

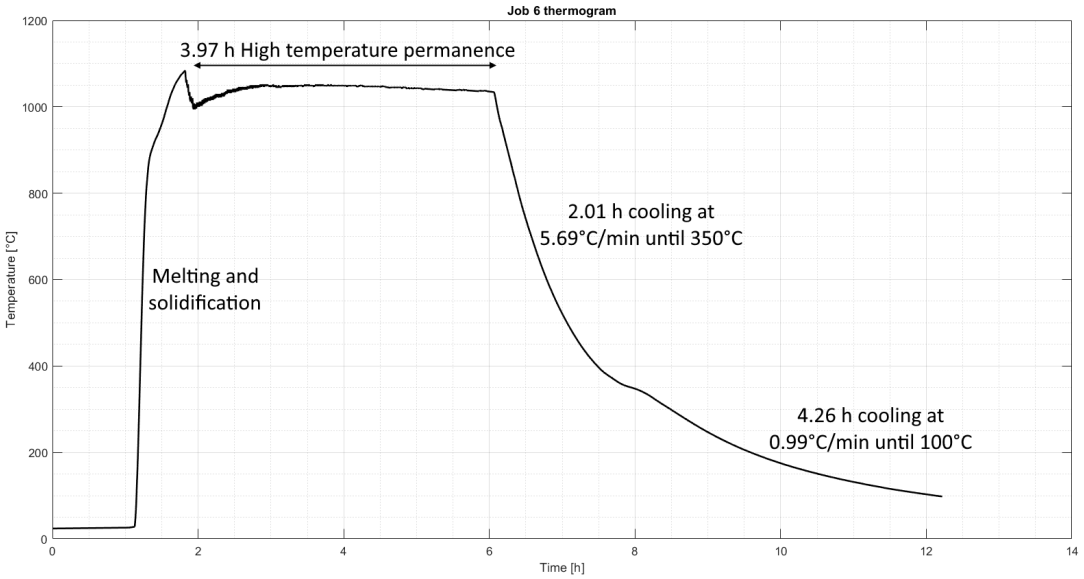

(a)

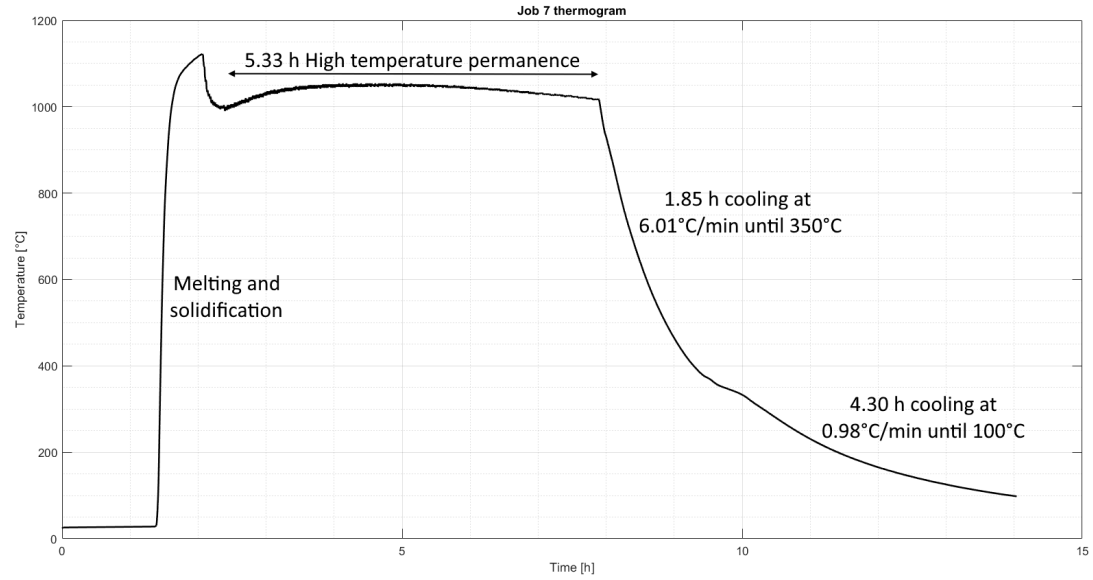

(b)

Figure 4.4: (a) Thermal history of job 6 with temperature measured at the baseplate, (b) Thermal history of job 7 with temperature measured at the baseplate.

diamond suspensions and underwent a final step using a suspension of colloidal silica according to ASTM E3-01 [64]. The polished specimens were analysed with OEM through a Leica MEF4M equipped with camera LEICA DFC295 to evaluate

their porosity. The polished surfaces have been later etched for microstructural analysis using Nital (containing 2%vol of HNO_3 in ethanol), Vilella (containing 1g of picric acid and 5 mL HCl in 100 mL ethanol) or Picral solutions (containing 4 g of picric acid in 100 mL of ethanol). Etching time were between 5 s - 25 s. The unetched specimens were observed using Zeiss EVO15 SEM, equipped with SE and BSE detection probes together with an EDS Oxford Ultimmax probe for semi-quantitative chemical analysis.

4.5 Differential Scanning Calorimetry

A sample of the as-built H13 material obtained from the same powder feedstock and manufactured using a bed preheat of 750°C was has undergone preliminary Differential Scanning Calorimetry (DSC) using a Setaram 92 16.18, in the work by [4]. The aim of this thermoanalytical technique is to study the thermal behaviour of a material across a specified temperature range analysing the specific heat of each occurring phase transformation. In this case a range between 20°C - 1300°C was evaluated with a scan rate of 20°C/min. A cooling ramp with the same scan rate followed the heating ramp with no high temperature maintenance.

4.6 Retained austenite evaluation with XRD

To evaluate the content of evolution of austenite from the as-built specimens and following the heat treatment, XRD analysis was adopted. The measurements were performed by a Pulstech USA μ-x360 diffractometer through a 2D revealer using the $\cos\alpha$ method for the evaluation of diffraction peaks according to Bragg's law, integrating the area within the corresponding peaks to evaluate the volume content of ferrite and austenite in polycrystalline samples. In particular, the main diffraction peak of each of the two phases was analysed. The procedure was conducted using a Cr anode (K_α at 2.29 $\dot{A}$), with 30 kV of accelerating voltage 1.5 mA of beam current selecting peaks between 120° - 175° and repeating the measurement over the all Debye ring, obtaining an average value. In figure 4.5 it is shown an example of XRD diffraction spectrum with relative Debye ring in a 3D visualization, showing the two peaks of ferrite (at higher angles) and austenite (at lower angles), taken from sample j7-M2B in the as-built condition. The final retained austenite percentage is taken as an average of all the values measured along the Debye ring.

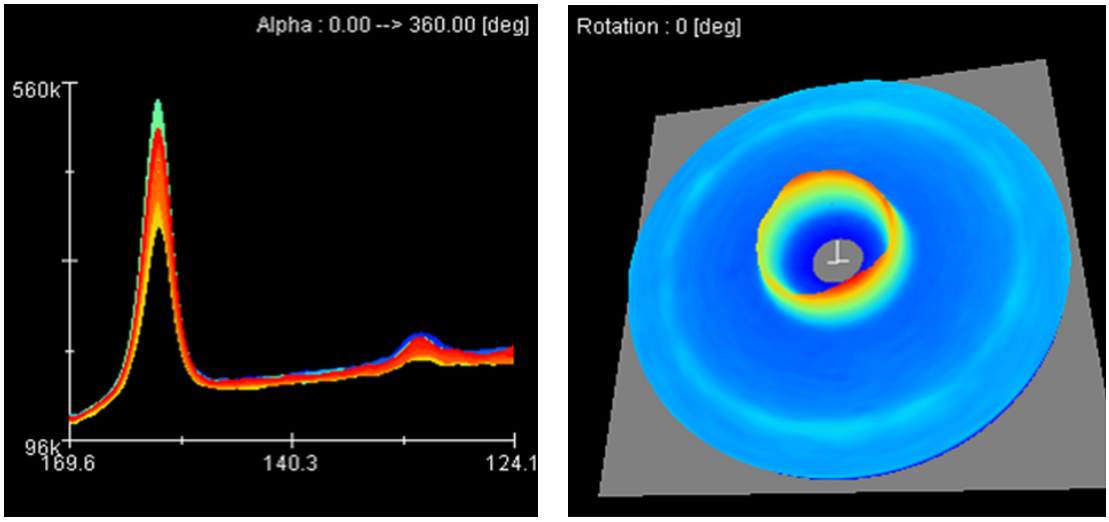

(a) (b)

Figure 4.5: Retained austenite measurement example coming from j7-M2B: (a) XRD spectrum with ferrite peak at higher angles and austenite peak (smaller) at lower angles, (b) Debye ring 3D visualization.

4.7 Heat treatments

The aim of the work was to study the effect of heat treatments on the as-built EBM material. Therefore a set of heat treatments have been performed. The choice of the heat treatment was performed based on the NADCA 207:2003 specifications of die casting materials [31], hence high temperature austenitizing of 30 min followed by quenching in oil or gas and double tempering of 2 hours each followed by air cooling. The schematics of the heat treatment is shown in figure 4.6. Fist the effects of different austenitizing temperatures, i.e. 1025°C (specimen j5-5), 1050°C (specimen j5-11), 1075°C (specimen j5-13) and 1100°C (specimen j5-15), has been evaluated through a 30 min air austenitizing inserting the specimens in the furnace already at temperature, followed by oil quenching. The aim of this analysis was to evaluate the solubility of carbides for different austenitizing condition. Another specimen was austenitized at 1050°C from room temperature (specimen j5-9) following a slow heat path lasting about 2 hours before 30 min austenitizing and oil quenching. The treatments were performed in a Nabertherm LH60/14, Nabertherm N120/85HA and Manfredi Warmy 9. Other two samples coming from job 7 (j7-M2B) have undergone full vacuum austenitizing at 1050°C and 1100°C for 30 min at a pressure of $2.9 \cdot 10^{-3}$ mbar in a TAV MIniJet HP235 furnace followed by nitrogen gas quenching at 3.5 bar pressure. The two quenching processes have been monitored using a thermocouple in direct contact with the

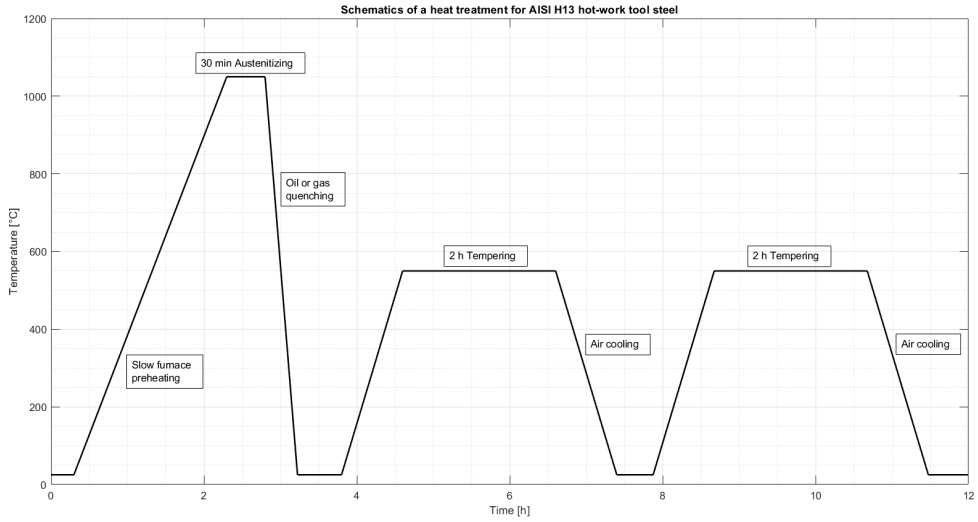

Figure 4.6: Schematics of the heat treatment followed in the experimental section.

sample and the heat path evolution is shown in figure 4.7. The tempering curves were built using samples from job 7 with the aim of reducing variability in the as-built microstructure. For each curve 6 samples were treated with double tempering. The sample was inserted in the furnace at room temperature, an heating stage was followed by a two hours soaking, while cooling was performed in air. The selected tempering temperatures were 400°C, 450°C, 500°C, 550°C, 600°C, 650°C.

4.8 Macro and micro-hardness tests

Micro and macro-hardness tests were performed to measure the mechanical properties of each specimen. The measurement of surface hardness is generally preferred for tool steels instead of tensile properties due to its easiness, i.e. need of a lower number of samples and quicker measurement, together with direct connection with abrasion resistance with respect to tensile properties evaluation. Micro-hardness tests were adopted to evaluate the as-build material (specimens j6-M2B and j7-M2B) in terms of possible anisotropy in the microstructure along the building direction. Tests was performed on a Leica VMHT with a Vickers indenter with 500 gF with 15 s of penetration time. Macro-hardness tests were performed using a Vickers scale on an EMCO-TEST M4U 025 with load of 100 kgF and 15 s of penetration time. All the measurements have been performed according to UNI EN ISO 6507-1 [66].

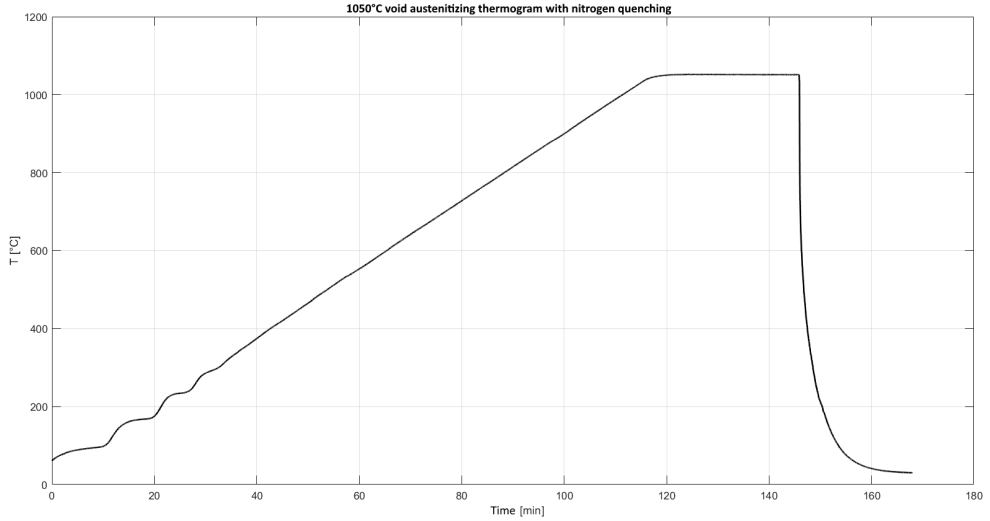

(a)

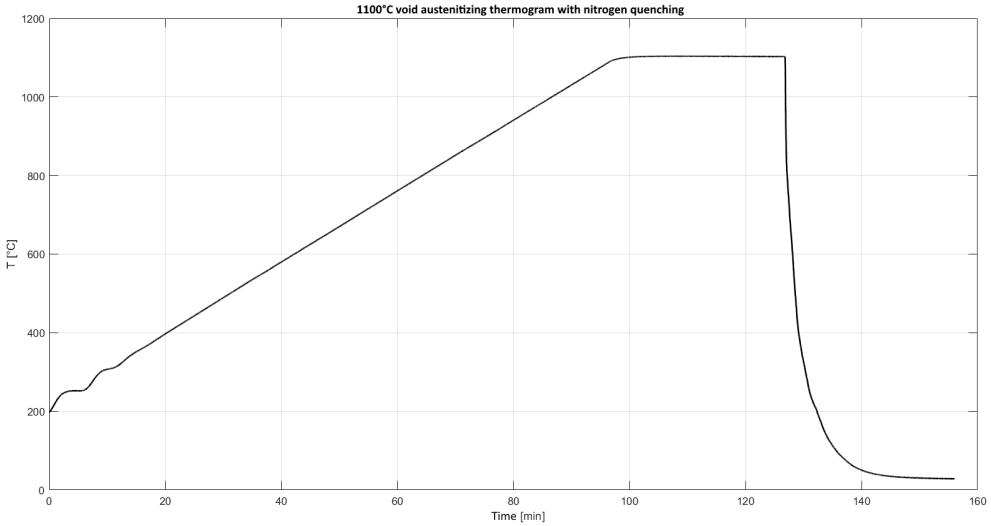

(b)

Figure 4.7: (a) Thermal history of 1050°C vacuum austenitizing and nitrogen quenching, (b) Thermal history of 1100°C void austenitizing and nitrogen quenching.

4.9 Image analysis

In addition, a number of four SEM micrographs with ×7500 magnification for each specimen (corresponding to each heat treatment condition) underwent image analysis using ImageJ software with the purpose of characterizing the evolution of the carbide population in terms of particle size distribution. The experimental

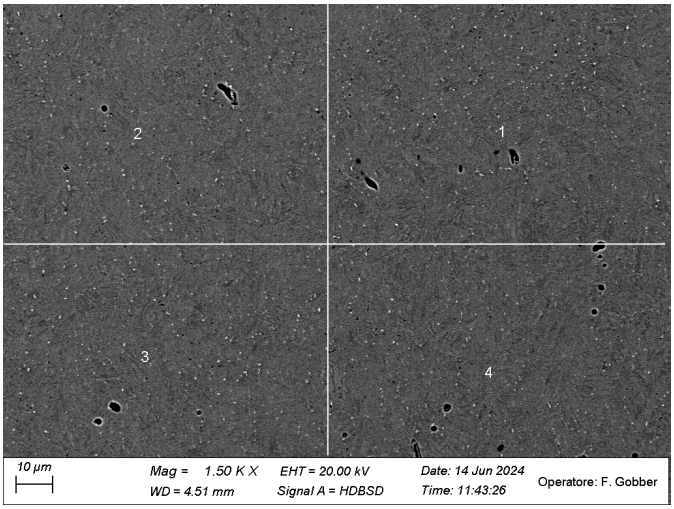

Figure 4.8: Example of overview for image analysis, taken from specimen 1050-550. Through a division into four sectors the images to be analysed were obtained.

procedure is described as follows. Each image was obtained using a Zeiss EVO15 SEM in BSD mode on polished samples to ensure a higher contrast of carbides with respect to the surrounding matrix. The Working Distance was set at 4.50 mm with an accelerating voltage of 20.00 kV. The images were taken from the bulk of each specimen, to avoid possible surface defects. The most central area of about 177×121 μm^2 was taken into account through an overview (×1500) and divided into four sectors, as shown in figure 4.8. Through this subdivision, the four analysed images were obtained, taken at ×7500 magnification. The images were obtained with a standard resolution of 1024×768 pixels and converted in 8-bit. They were then upscaled at 5000×3395 pixels and converted into binary leveraging on the contrast due to heavier carbides. A set of binary functions were applied using ImageJ software to fill holes inside closed particles, remove background noise due to possible errors in manual threshold selection (for binary generation) and to split agglomerates into smaller constituting particles. The complete algorithm is specified hereafter:

- SEM micrograph capture: obtaining a 1024×768 image taken with ×7500 magnification, 4.50 mm of working distance, 20.00 kV of accelerating voltage.
- 8-bit conversion: RGB to 8-bit conversion to allow binarization.
- SEM bar removal: removal of the lower SEM settings bar, to obtain a 1022×694 pixels image.
- Image upscaling: upscaling to 5000×3395 pixel size. This passage was fundamental to improve the efficiency of the later "Watershed" function, ensuring

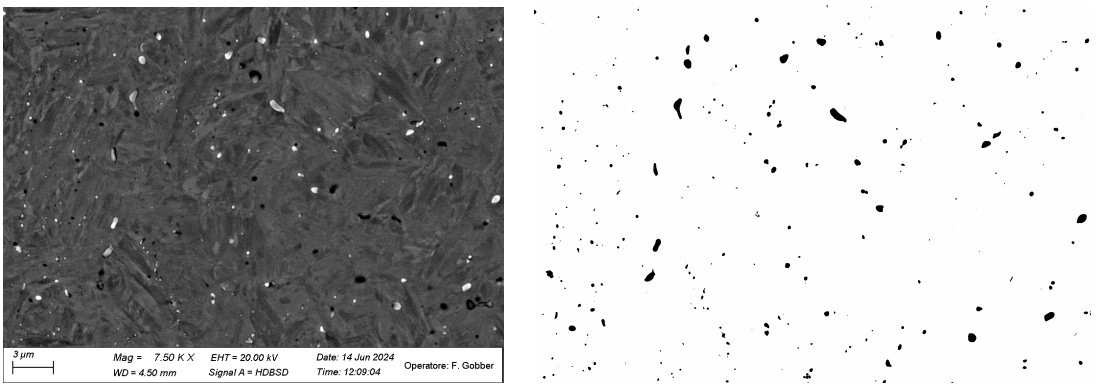

(a) (b)

Figure 4.9: Example of graphical results of the image analysis algorithm applied on a specimen taken from j7-M2B quenched at 1050°C and tempered at 550°C: (a) original SEM micrograph, (b) processed binary image where carbides are analysed (in black).

higher quality results.

- Scale measurement: conversion of the pixel size in micron size, with 1 μm corresponding to 138.62 pixels.
- Binarization: application of a manual threshold to convert the image into binary.
- Noise removal: application of "Despeckle" function in cases of high noise to remove it.
- Holes filling: application of the "Fill Holes" function in closed particles to have a filled shape.
- Agglomerate splitting: in cases of large agglomerates, the "Watershed" function was used to separate all the constituting particles by recognising the shape of the agglomerate and applying a sharp cut.
- Particles analysis: particles above a threshold set as 30 pixels of area (approximately 1561 nm^2 with equivalent diameter of 45 nm) were considered to avoid eventual noise detection. The "Analyze particles" function generates a table containing data concerning particles areas, area faction and Feret diameter.
- Data analysis: the available data from each specimen was processed through Minitab software to obtain the final particle size distribution. In particular for a single specimen the populations of the four analysed images were

included in a single dataset. This final dataset was modelled through a 3 parameter log-normal distribution obtaining the Location, Scale and Threshold parameters together with the total number of particles.

- Data plot: the three parameters describing the distribution are used to build the final Particle Size Distribution (PSD) curve. Results from each heat treatment condition are compared to characterize the evolution of carbides population.

The results of such image analysis algorithm is shown as an example in figure 4.9. The indicators that were analysed were the Feret diameter (d_F) and the equivalent circle diameter (d_{eq}). The first one is defined as the maximum distance between two parallel tangential lines to an object. The equivalent circle diameter is the diameter of the circle equivalent area to the particle one. The results of this data analysis are presented in chapter 5.

Chapter 5

Results and discussion

5.1 Characterization of the as-built material

During the EBM forming process, the AISI H13 powders have undergone a complex heat path which brought them to densification in the final shape. During the process, a deflected high energy electron beam preheats of the whole bed at a temperature around 1040°C, causing partial sintering with formation of necks between powder particles as described in section 3.3.2. During the melting step, the electron beam is selectively focused on the powders, creating a melt pool. Due to the presence of vacuum in the chamber, some of the material may vaporize bringing to small changes in the chemical composition. Moreover, according to the metal alloys of the baseplate (usually stainless steel), some elements, such as Cr, may diffuse to the metal part. Once the beam moves, a rapid solidification process begins due to the relatively small geometry of the melt pool and the extremely high heat transfer. From the metallurgical point of view, the material will experience a certain number of remelting and thermal cycling due to subsequent additional beam passages, followed by a long austenitizing at a temperature slightly below 1040°C and a final slow cooling in He, leading to a mixed martensitic/bainitic structure. The high temperature dwell time linearly depends on the process parameters adopted and on the part volume. Regarding job 5, small cubes with 18 mm side were built. Their process parameter and surface morphology can be correlated with internal porosity through a model proposed by [63]. An experimental analysis has been carried out to qualify this model and results are available in table 5.1, taken by [4]. Sample j5-15 parameters were adopted to reduce process time for the build up of job 6 while sample j5-13 parameters were chosen for job 7 to also minimize the porosity. Data available from job 6 and job 7 thermograms in figure 4.4 is reported in table 5.2. The soaking time at high temperature is longer for job 7 with respect to job 6 due to lower scan speed (2000 mm/s against 4000

Table 5.1: Job 5 porosity assessment through experimental analysis by [4].

Sample	**Beam speed [mm/s]**	**Beam current [mA]**	**Porosity [%]**	**St. dev**
1	2000	10	0.016	0.005
2	3000	10	0.016	0.146
3	4000	10	1.278	0.940
4	5000	10	6.209	1.917
5	2000	12	0.015	0.014
6	3000	12	0.015	0.007
7	4000	12	0.192	0.285
8	5000	12	2.236	1.417
9	2000	14	0.013	0.012
10	3000	14	0.011	0.008
11	4000	14	0.024	0.011
12	5000	14	0.906	1.074
13	2000	16	0.005	0.003
14	3000	16	0.020	0.013
15	4000	16	0.017	0.015
16	5000	16	1.268	1.651

mm/s), hence the total energy provided to melt the powders will be much higher in the case of job 7. Regarding cooling parameters, results are comparable, having a similar cooling rate in the 800°C - 500°C of about 7.4 - 7.5 °C/min. The performed cooling path is shown in figure 5.1 with a single cross due to partial overlapping.

The results are shown in figure 5.2. Due to the higher scan speed, the sample deriving from job 6 was highly porous (1.458%), showing presence of LoFs. This kind of defect has an elongated shape and is located along the the original powder bed layers which did not melt completely, not creating a metallurgical bond with the bottom layers. In contrast, the sample deriving from job 7 showed no signs of LoFs and negligible amounts of porosity (0.029%). The results from a porosity evaluation through ImageJ software considering 11 micrographs for job 6 and job 7 are reported in table 5.3. The two as-built specimens showed clear signs of heavy precipitation phenomena due to the elevated time at high temperature and to the relatively slow cooling in He, allowing diffusion of alloying elements to occur. The OM micrographs reported in figure 5.3 show a needle-like microstructure compatible with the mixed martensitic/bainitic one predicted by CCT curves in figure 5.1, as also reported by [58] and [61]. In addition, there is a clear evidence

Table 5.2: Heat path data from the thermograms of job 6 and job 7

Job type	High T dwell time [h]	800°C-500°C cooling rate [°C/min]
6	3.97	7.49
7	5.33	7.41

Job type	1040°C-350°C cooling time [h]	1040°C-350°C cooling rate [°C/min]	350°C-100°C cooling time [h]	350°C-100°C cooling rate [°C/min]
6	2.01	5.69	4.26	0.99
7	1.85	6.01	4.30	0.98

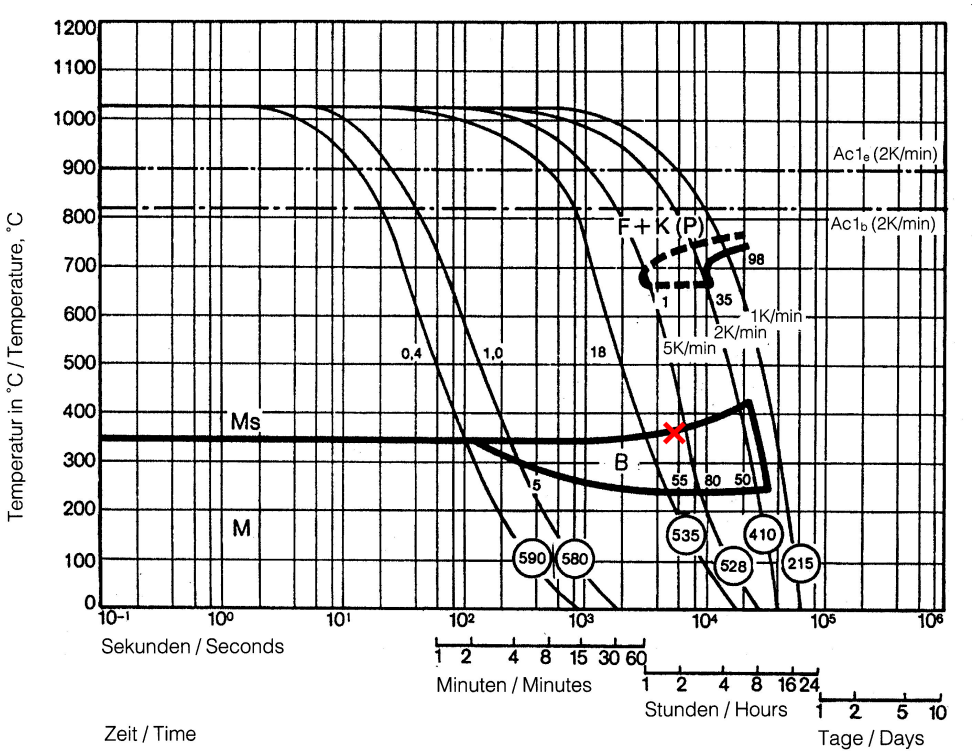

Figure 5.1: CCT curve of AISI H13 reporting the cooling path followed during job 6 and job 7 indicated with a single cross since results overlap almost completely.

of an anisotropic microstructure elongated and parallel to the building direction, which formed during solidification and corresponds to elongated prior austenitic grains, as also evaluated by [58]. In particular, detailed micrographs showed the

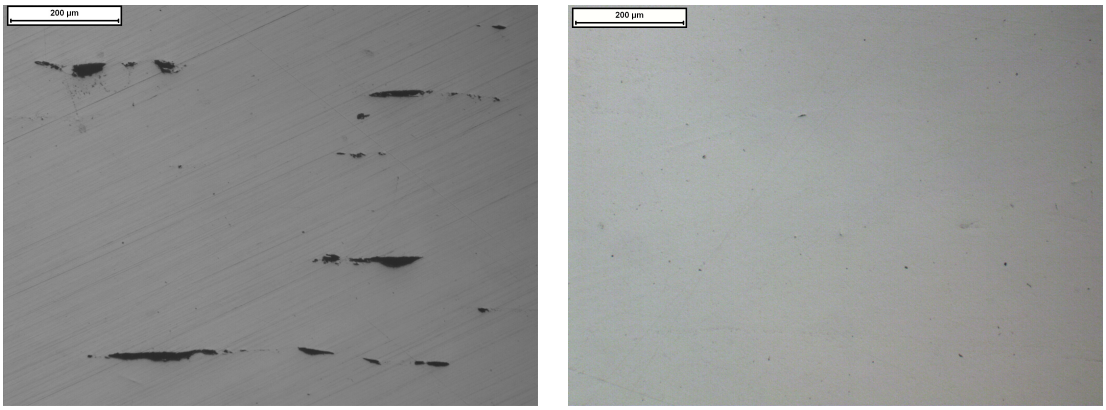

(a) (b)

Figure 5.2: OM Micrographs with ×100 magnitude showing porosity of unetched j6-M2B and j7-M2B: (a) view of j6-M2B, (c) view of j7-M2B.

Table 5.3: Preliminary porosity assessment of job 6 and job 7 considering the specimens j6-M2B and j7-M2B.

Job type	**Porosity [%]**	**St. dev**
6	1.458	0.504
7	0.029	0.005

presence of elongated ferritic grains with dimensions greater than 10 μm. Despite the presence of microstructural dishomogeneities, the high preheat temperature and soaking time has brought to a higher level of homogenization with respect to H13 samples produced via SLM [56]. Specimen j6-M2B showed a macro-hardness of 429.3 HV, having higher micro-hardness values of 504.0 HV as shown in table 5.4. This can be attributed to its porosity content, in fact, this factor strongly reduces macro-hardness values while not influencing micro-hardness. Specimen j7-M2B showed a macro-hardness of 467.3 HV, providing consistent micro-hardness of 474.8 HV due to lower porosity. Despite showing low homogeneity level at the micro scale, the EBM as-built materials processed with 1040°C bed preheat present a rather flat micro-hardness profiles along the building directions, as shown in figure 5.4. In fact, no net gradients was found. The lower value of micro-hardness of specimen j7-M2B can be attributed to the longer permanence time at high temperature causing grain coarsening. The prolonged time at high temperature followed by a relatively slow cooling during the two EBM jobs determined the decrease of M_f temperature, hence the presence of retained austenite. According to XRD

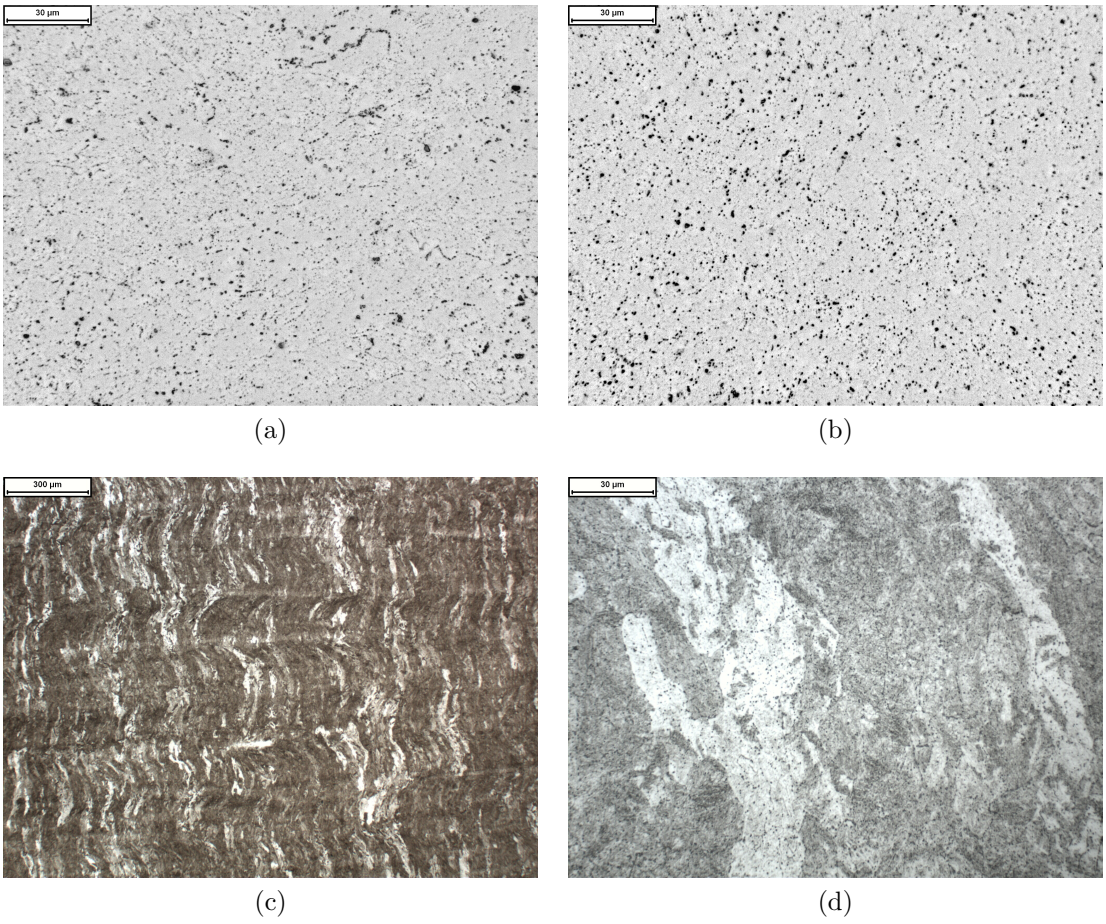

Figure 5.3: OM Micrographs ×500 showing carbides and microstructure in etched specimens j6-M2B and j7-M2B: (a) carbides in j6-M2B, (b) carbides in j7-M2B, (c) 1D grain anisotropy parallel to the building direction in j7-M2B, (d) detail of microstructure in j7-M2B.

measurements, both the specimens j6-M2B and j7-M2B reported a fraction of retained austenite around 9% - 10%. This is not acceptable for the final application, since retained austenite may transform during high temperature usage or due to mechanical stresses, determining severe distortions in the final part [2]. Retained austenite data is included in table 5.4. Based on the previously described porosity assessment, sample coming from job 6 were were not further investigated. Specimens from job 7 were further characterized in the as-built state and then used for studying the heat treatment route.

In the work proposed by [4], a specimen of H13 with the same chemical composition reported in table 4.2, but built using a bed preheat at 750°C, underwent a

Table 5.4: Hardness and retained austenite fraction of as-buit specimens j6-M2B and j7-M2B.

Job type	Macro HV 100	St. dev	Micro HV 0.5	St. dev	Ret. Austenite [%]	St. dev
6	429.3	7.8	504.0	21.9	9.9	2.0
7	467.3	0.5	474.8	12.4	10.4	2.6

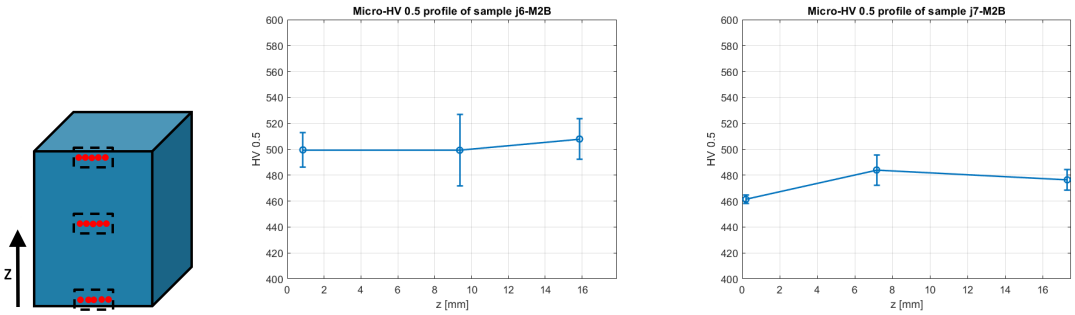

(a) (b) (c)

Figure 5.4: Micro-hardness profile in as-built j6-M2B and j7-M2B specimens: (a) Reference system where five measures have been performed on a line at the bottom, the middle and the top of the specimen, (b) Micro-HV 0.5 profile for sample j6-M2B, (c) Micro-HV 0.5 profile for sample j7-M2B.

preliminary differential scanning calorimetry (DSC) analysis. The resulting curve is shown in figure 5.5. A broad exothermic peak is revealed between 400°C - 600°C due to carbides precipitation, and two endothermic peaks associated with the magnetic transformation at Curie temperature (T_c) and with the transformation from ferrite to austenite occuring between A_{c1} and A_{c3}. No relevant signs of carbides dissolution at higher temperature can be easily addressed to this analysis due to the lower preliminary carbides precipitation with respect to 1040°C preheated samples. SEM micrographs from specimen j6-M2B and j7-M2B are reported in figure 5.6. Signs of carbides networks are found along prior austenitic grains. EDS spectra from sample j7-M2B verify that they are V-rich carbonitrides with presence of N, as shown in figure 5.7.1. The carbides total count and particle size distribution has been evaluated using ImageJ software according to the methodology described in section 4.9. Results are shown in figure 5.7 and table 5.5: the as-built material shows important signs of carbides precipitation having a measured carbides fraction of 3.68%, as confirmed by [61].

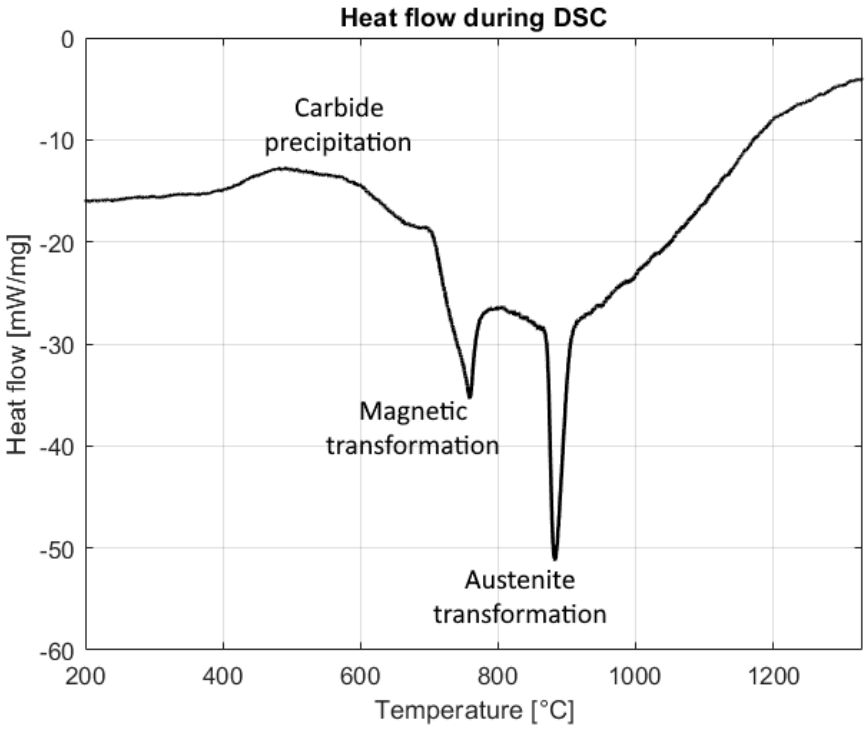

Figure 5.5: DSC curve of AISI H13 with N addition, after an EBM manufacturing process with bed preheat at 750°C, reporting heat flux with respect to sample temperature. A broad exothermic peak can be found due to carbides precipitation and two sharp endothermic peaks at higher temperatures can be seen due to magnetic transformation and austenitizing.

Table 5.5: Job 7 as-built summary, where hardness, carbides fraction and retained austenite are shown.

Sample	$\mathbf{T}_{platform}$ **[°C]**	**Macro-HV 100**	**Carbide fraction [%]**	**Count [4 photos]**	**Retained austenite [%]**
j7-M2B	1040	467.3 ± 0.5	3.68 ± 0.29	7667	10.4 ± 2.6

5.2 Austenitizing and quenching

Samples from job 5 undertook an austenitizing step. From the point of view of carbide size and fraction they can be considered similar to job 7, since most of them would precipitate during the final slow cooling in He. However, the aim of this treatment is to study the solubility of carbonitrides in austenite at high temperature, to obtain fine martensitic structure rich in C and alloy elements after

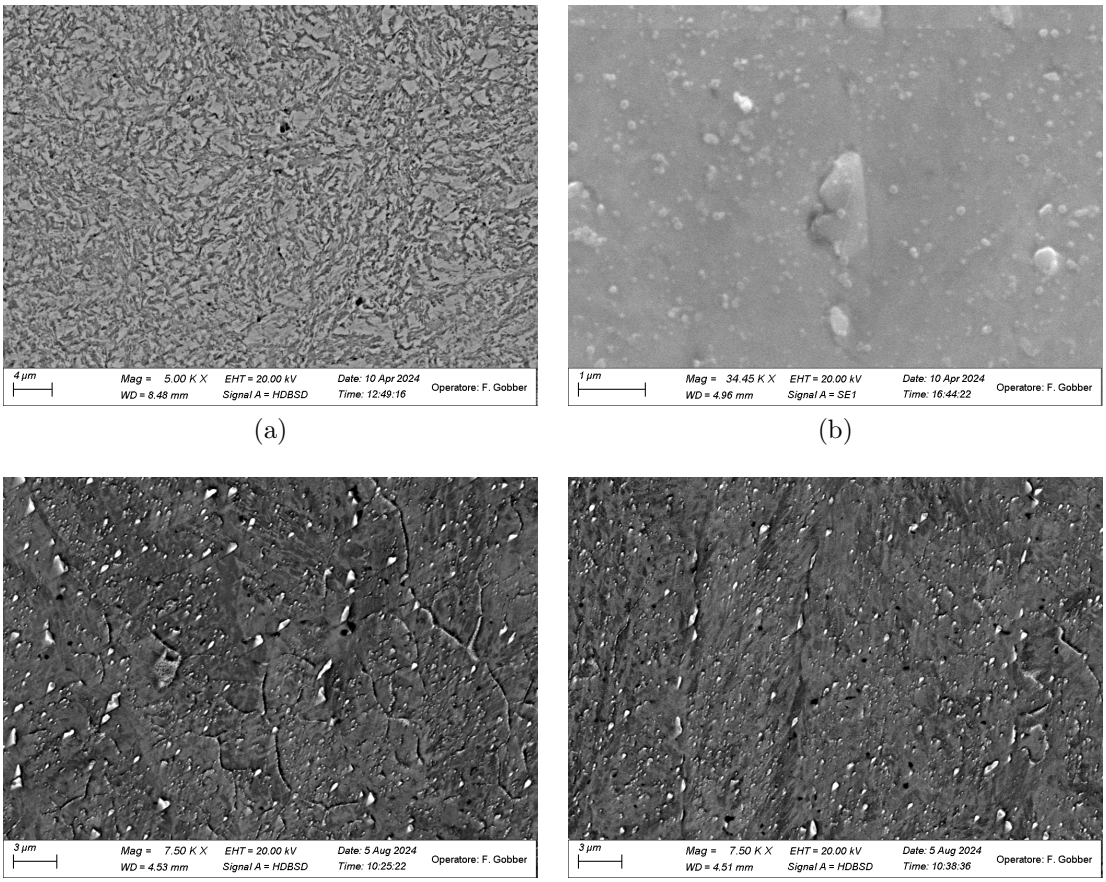

(a) (b)

(c) (d)

Figure 5.6: SEM Micrographs of specimens j6-M2B and j7-M2B showing: (a) needle-like microstructure in etched j6-M2B, (b) detail of a micrometric carbide, (c) and (d) carbides precipitation in unetched j7-M2B.

quenching. During tempering they will precipitate as nanometric rounded particles with extremely high strengthening effect. All the treated samples in the range 1025°C - 1100°C showed presence of undissolved carbonitrides. This is caused by the N content found in the former powders as described in section 2.5.4 which increases the stability of the V(C,N) species in austenite until temperatures of 1300°C. This was confirmed by EDS analysis conducted on these particles at all the four austenitizing temperatures. The final microstructure is the result of the quenching step and is composed of martensite needles in prior austenite grains together with undissolved carbonitrides particles (figure 5.8). All of them present martensitic structure. Despite the hardening treatment, the 1025°C, 1050°C and 1075°C austenitized samples still showed signs of banded microstructure parallel

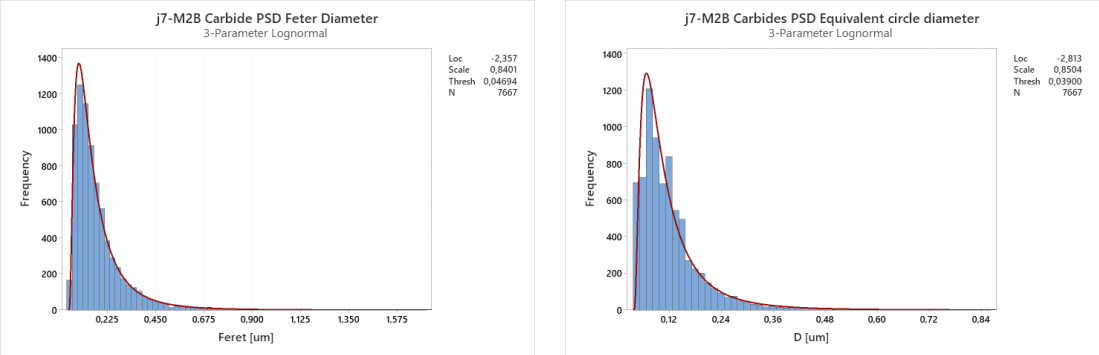

(a) (b)

Figure 5.7: Carbides PSD of specimen j7-M2B coming from image analysis. A three-parameters lognormal distribution has been used to model experimental: (a) Feret diameter plot, (b) Equivalent circle diameter plot.

to the building direction. This characteristic gradually disappears in the 1100°C austenitized specimen. SEM micrographs reported in figure 5.9 highlight the trend in carbonitrides dissolution with respect to the as-built material. EDS confirms the high content in V and N even at 1100°C, in accordance with the findings of [3]. An example of EDS spectra for specimen j5-15 (treated at 1100°C) is shown in figure 5.10.1 With the increasing of austenitizing temperature the volume of carbonitrides decreases as well as their total number according to image analysis, as also shown in table 5.6 and figure 5.10. In addition, higher temperature austenitizing increases carbide roundness reducing presence of sharp edges typical of primary solidification. Moreover, hardness increases with austenitizing temperature in the range of 560.3 - 596.7 HV. This is caused by carbides dissolution, bringing more C in martensite, hence increasing its hardness. All austenitizing conditions show a content of retained austenite (measured with XRD) below 5% due to the rapid cooling in oil, which is in accordance with NADCA #207-2003 standard [31]. The lower content of retained austenite in specimens coming from job 5 could be due to by the lower soaking at high temperature during the building phase, which dissolved a lower carbide fraction in austenite with respect to job 7. The effects of increasing austenitizing temperatures are reported on carbides PSD in figure 5.11. The particle size distribution doesn't shift significantly due to increased stability of V(C,N) phases with respect to VC [3], [27], however the solubilization effect of carbonitrides with small size is clearly visible on the equivalent circle diameter plot and this is confirmed by the drop of carbides content. Despite that, this investigation confirmed the trend reported by [3], confirming that conventional austenitizing temperatures are not able to fully dissolve all carbonitrides due to the effect of nitrogen addition. Specimen j5-9 was treated at 1050°C

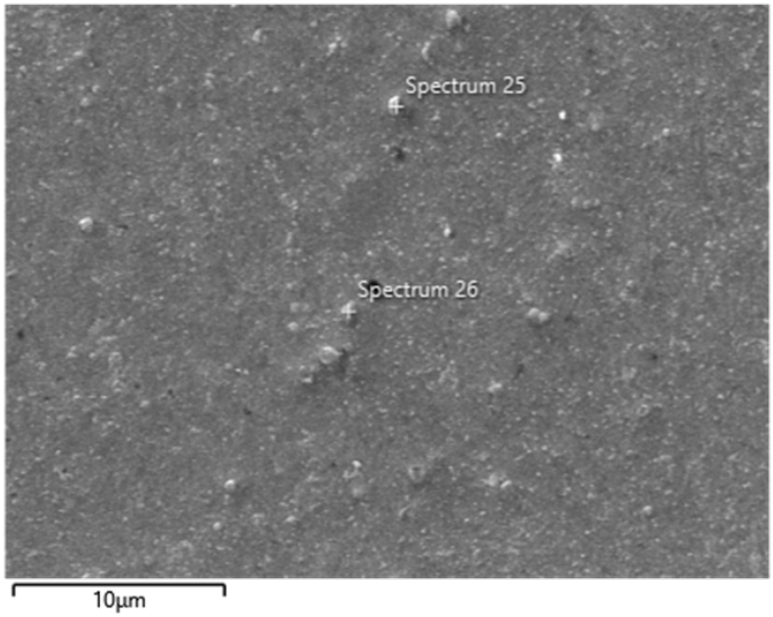

(a)

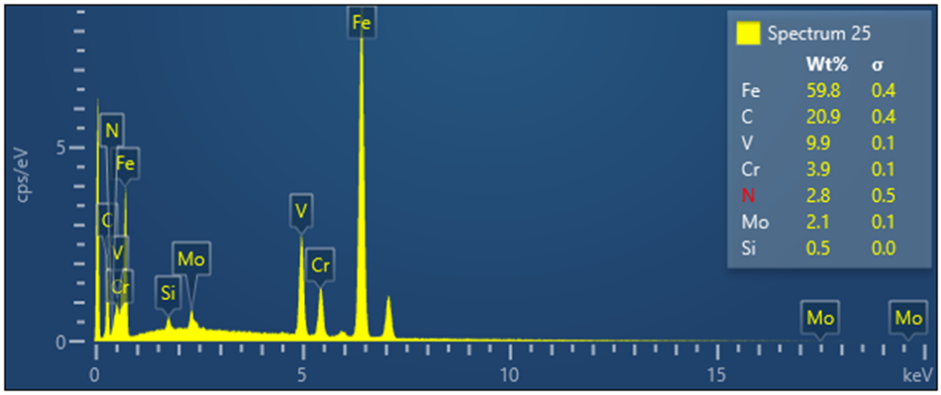

(b)

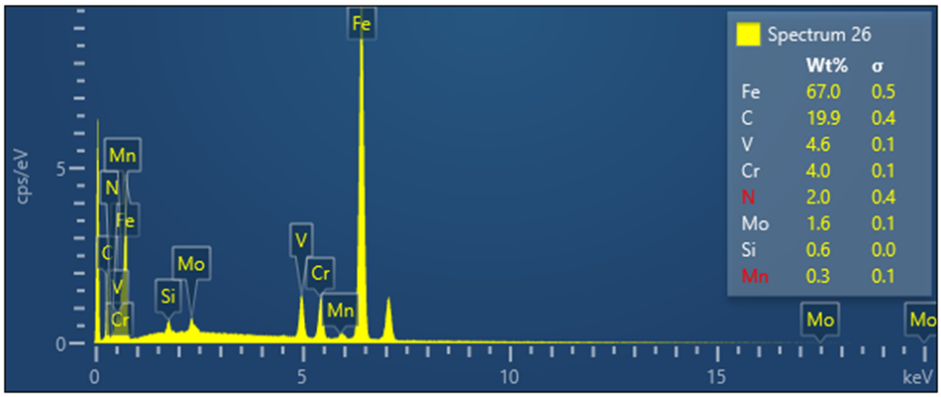

(c)

Figure 5.7.1: EDS spectrum of a V(C,N) carbide coming from a SEM micrograph of j7-M2B: (a) SEM micrograph where spectra 25 and 26 are obtained, (b) EDS spectrum 25, (c) EDS spectrum 26. The high weight percentage of C, V and N confirm this hypothesis.

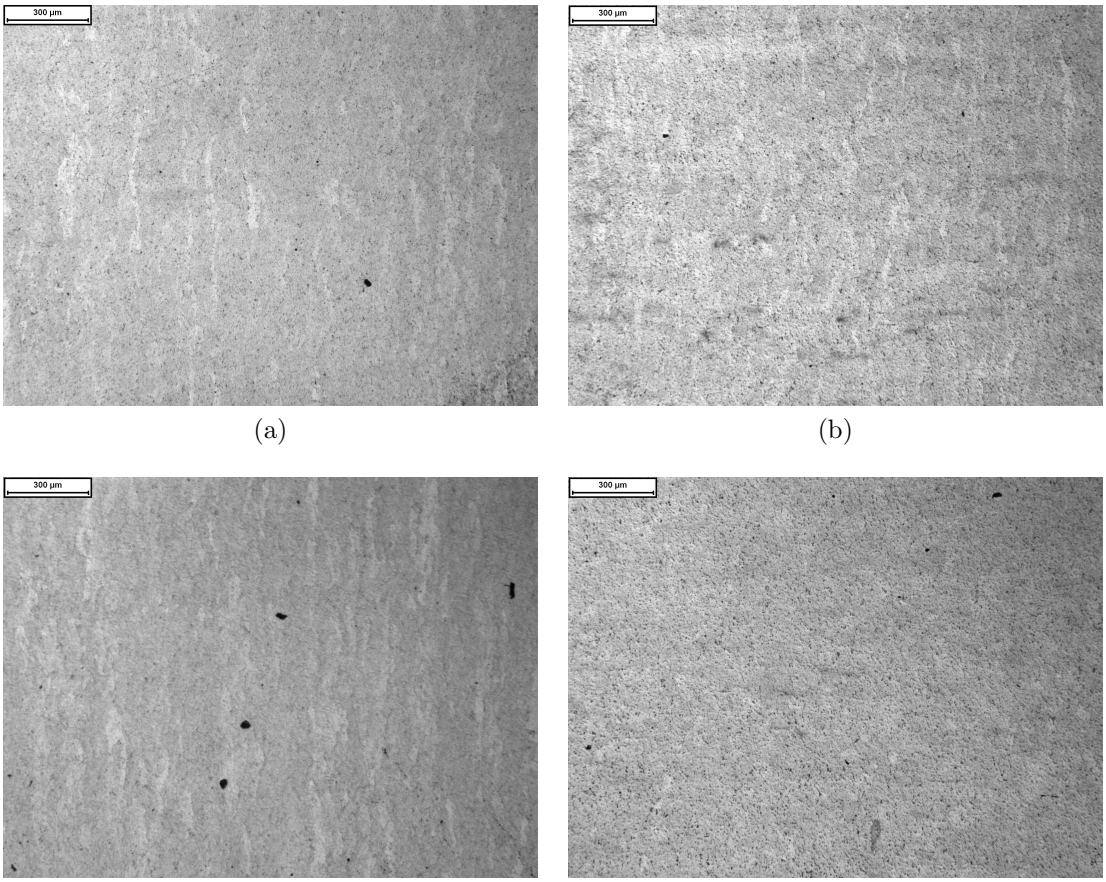

(a) (b)

(c) (d)

Figure 5.8: OM micrographs ×50 of quenched specimens showing prior austenitic grain superstructure: (a) 1025°C, (b) 1050°C, (c) 1075°C, (d) 1100°C. For the 100°C specimen it is possible to appreciate the gradual disappearance of banded superstructures.

Table 5.6: Air austenitizing summary where hardness, carbides fraction and retained austenite are shown.

Sample	**T$_{aust}$ [°C]**	**Macro-HV 100**	**Carbide fraction [%]**	**Count [4 photos]**	**Retained austenite [%]**
j5-5	1025	560.3 ± 3.7	2.411 ± 0.073	2738	1.5 ± 1.0
j5-11	1050	577.3 ± 4.9	2.232 ± 0.310	2816	1.3 ± 1.1
j5-13	1075	584.7 ± 1.7	1.421 ± 0.060	2394	1.2 ± 0.9
j5-15	1100	596.7 ± 0.5	1.371 ± 0.179	936	2.2 ± 1.5

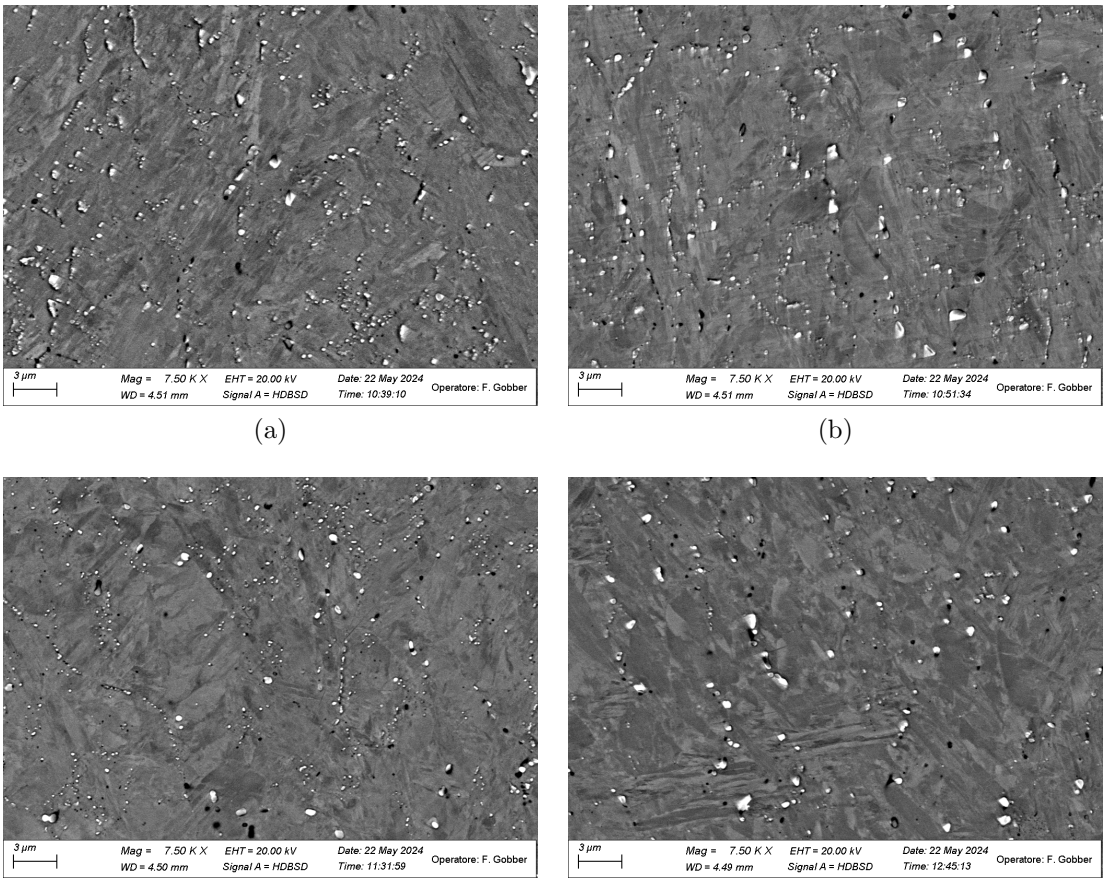

Figure 5.9: SEM micrographs ×7500 of quenched specimens showing carbides dissolution at higher temperatures: (a) 1025°C, (b) 1050°C, (c) 1075°C, (d) 1100°C.

for 30 minutes, starting from room temperature with a heating ramp of 2 hours. This preheating stage increased the total time at high temperature, contributing to dissolve a higher fraction of carbonitrides with respect to specimen j5-11 and to enhance grain coarsening, hence reducing hardness. Moreover, as shown in figure 5.11, the carbides particle size distribution shifts to higher diameters. This can be also be attributed to the higher time at temperatures $T<T_{aust}$, since the presence of N could promote the dissolution of Mo and Cr-rich carbides, while enhancing V(C,N) precipitation as suggested by [3]. Data for this treatment is reported in table 5.7.

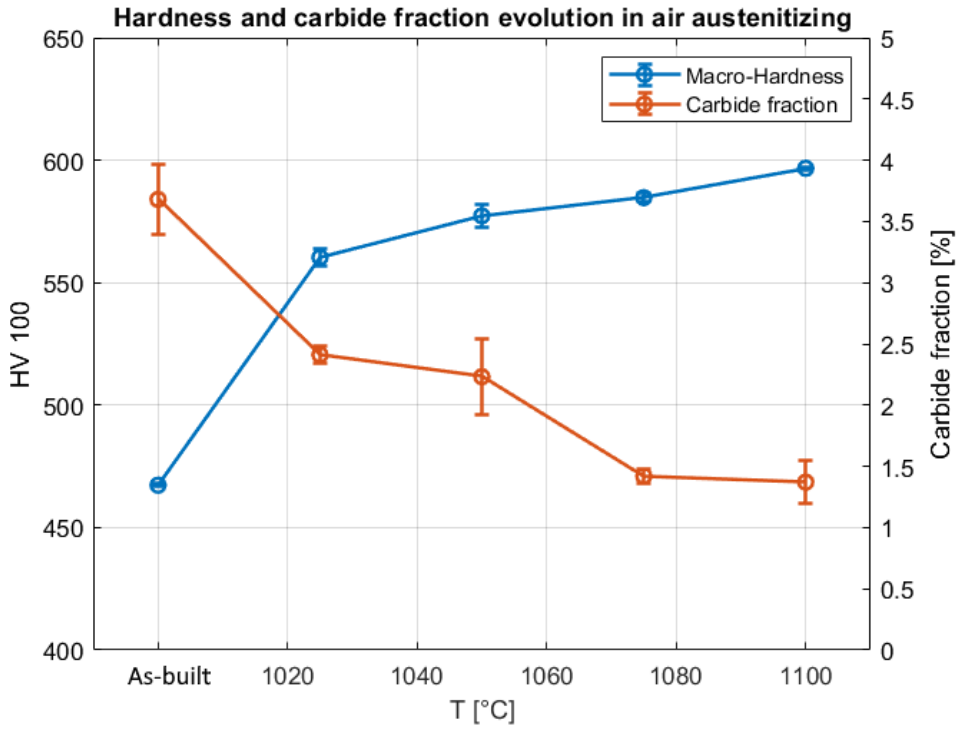

Figure 5.10: Macro-hardness HV 100 and carbides fraction in air austenitized and oil quenched specimens.

Table 5.7: Air austenitizing from room temperature summary for sample j5-9 where hardness, carbides fraction and retained austenite are shown.

Sample	**T$_{aust}$[°C]**	**Macro-HV 100**	**Carbide fraction [%]**	**Count [4 photos]**	**Retained austenite [%]**
j5-9	1050	567.7 ± 1.7	1.443 ± 0.170	2703	1.4 ± 1.3

5.3 Vacuum austenitizing and gas quenching

To simulate the conventional austenitizing condition on the chosen material, two samples coming from job 7 were vacuum austenitized at 1050°C or 1100°C and gas quenched. The reason for this treatment is to avoid the formation of the oxide skin which affects dimensional tolerances in as-built specimens, avoiding material loss. The treatment was conducted in a vacuum furnace and the samples were inserted at room temperature. Hence, a heating time of about 90-110 min was performed as shown in the thermograms in figure 4.7. The resulting microstructure is comparable to the one of air austenitized specimens, as shown by OM

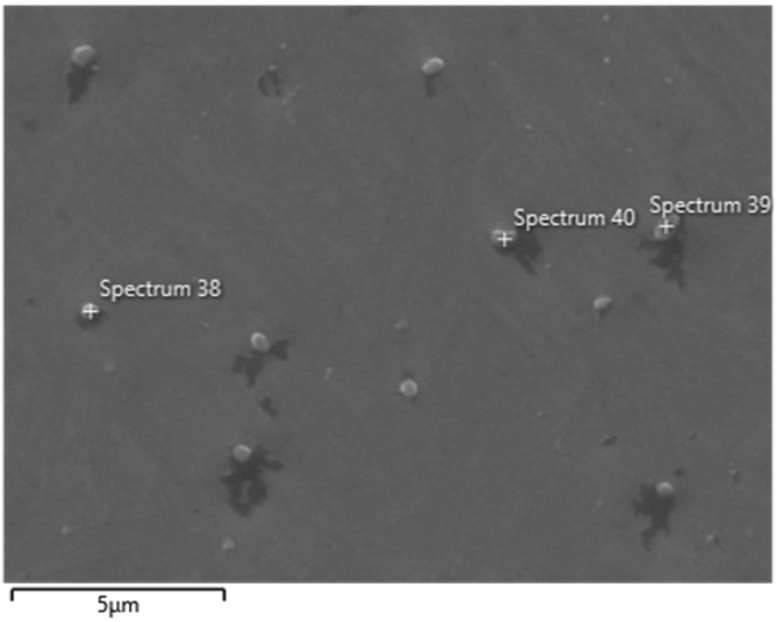

(a)

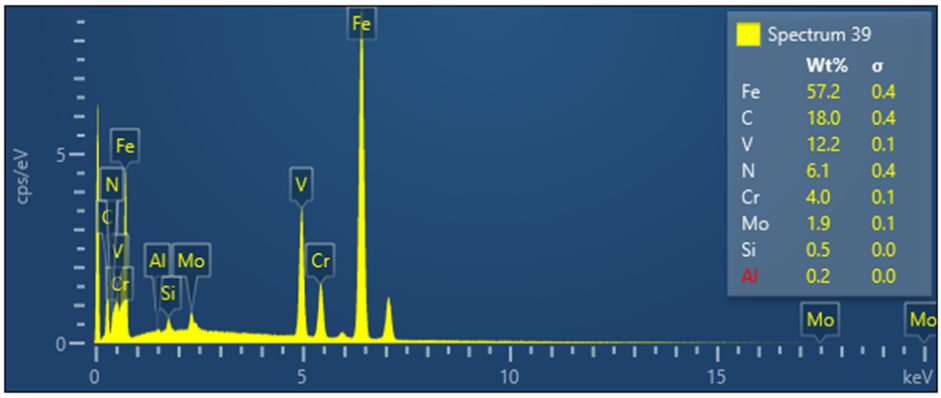

(b)

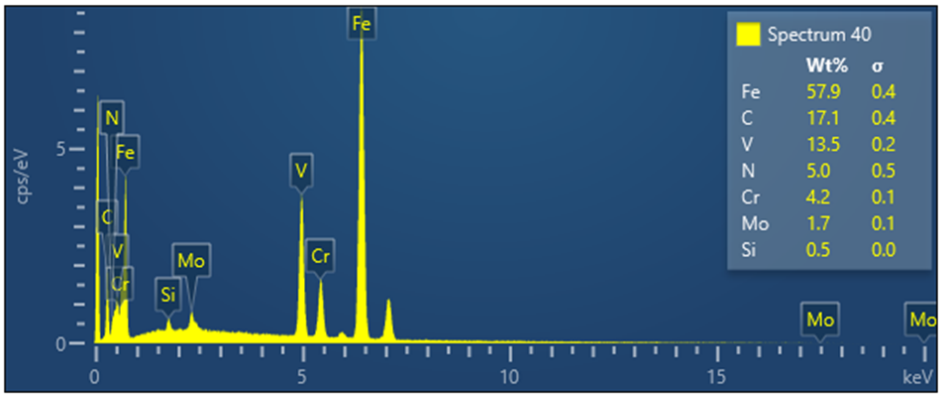

(c)

Figure 5.10.1: EDS spectrum of a V(C,N) carbide coming from a SEM micrograph of j5-15, austenitized at 1100°C in air: (a) SEM micrograph where spectra 39 and 40 are obtained, (b) EDS spectrum 39, (c) EDS spectrum 40. The high weight percentage of C, V and N confirm this hypothesis.

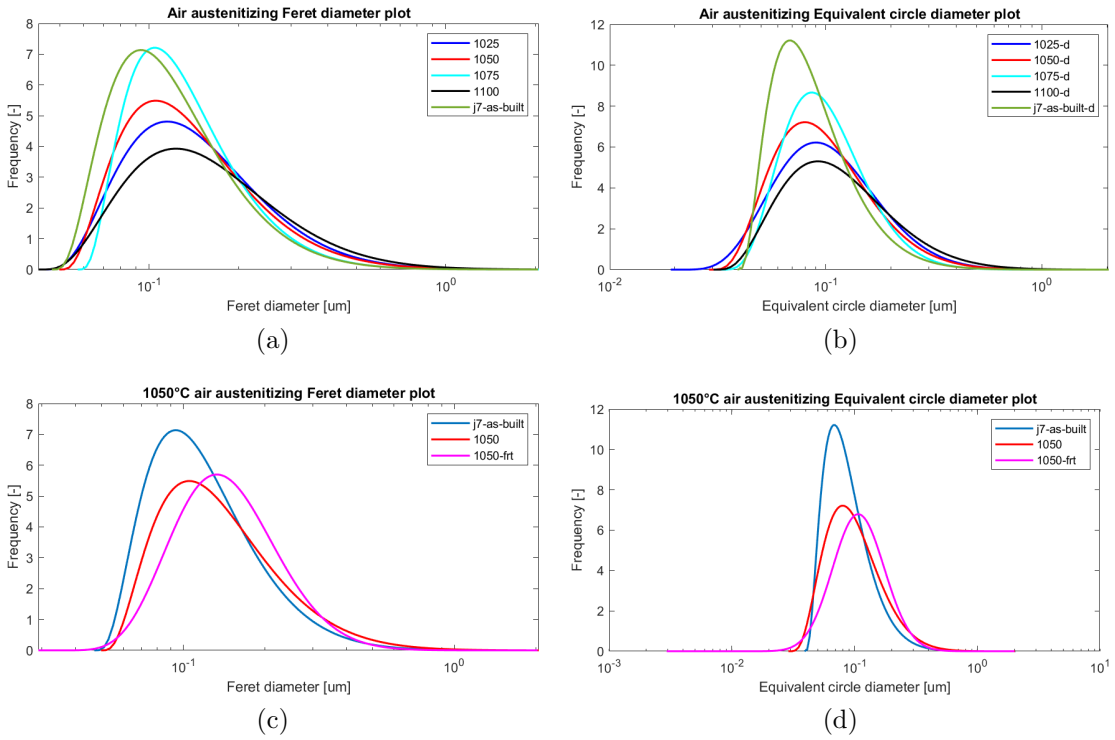

Figure 5.11: Air austenitizing PSD curves at different austenitizing temperatures against the as-built condition: (a) Feret diameter plot, (b) equivalent circle diameter plot, (c) comparison between 1050°C air austenitizing in Feret diameter, (d) comparison between 1050°C air austenitizing in equivalent circle diameter.

and SEM micrographs in figure 5.12, where undissolved carbides are embedded in a martensitic matrix. A clear difference in terms of carbides content can be appreciated between the two quenching conditions, with the 1100°C austenitizing bringing to a higher solubilization effect. However, even in this case, a decrement in hardness with respect to air treated samples have been found due to the higher time at high temperature causing grain coarsening and higher carbides dissolution, as shown in table 5.8 and 5.13. Similarly to the case of air austenitized sample from RT (j5-9), the carbides particle size distribution shifts to higher sizes due to possible coarsening of MC at T<T_{aust} as described earlier. The increment in retained austenite with respect to air austenitized samples can be explained with the shift of M_f to lower temperatures due to higher C content in austenite caused by carbides dissolution [1]. In facts, it is reasonable to accept that specimens coming from job 6 and job 7, contain more retained austenite than specimens coming from job 5 used for air austenitizing, since the higher building time, i.e. alloying elements and carbides dissolution which lowered M_f. In figure 5.14, the two

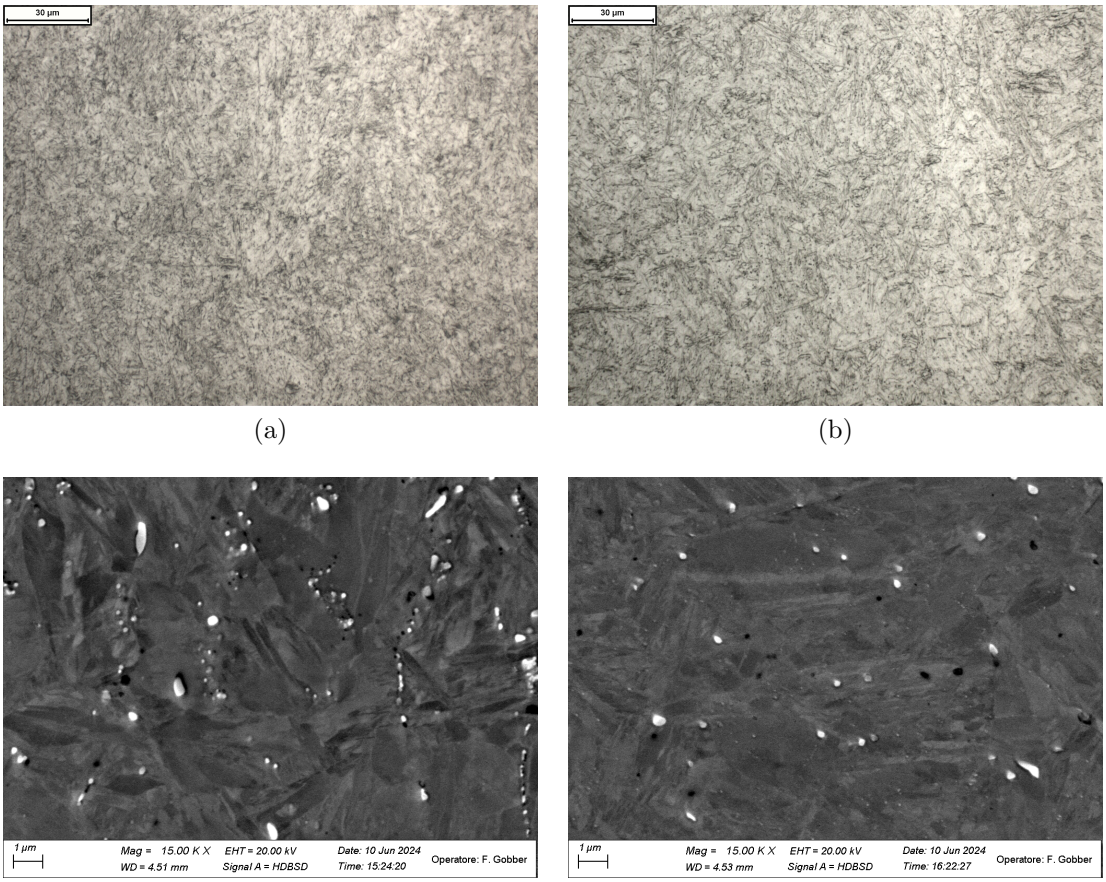

(a) (b)

(c) (d)

Figure 5.12: Vacuum austenitizing OM ×500 and SEM ×15000 microstructures: (a) OM etched 1050°C quenched, (b) OM etched 1100°C quenched, (c) SEM unetched 1050°C quenched, (d) SEM unetched 1100°C quenched.

Table 5.8: Vacuum austenitizing from room temperature summary for samples coming from job 7 where hardness, carbides fraction and retained austenite are shown.

Sample	**T**$_{aust}$**[°C]**	**Macro-HV 100**	**Carbide fraction [%]**	**Count [4 photos]**	**Retained austenite [%]**
j7-M2B	1050	544.0 ± 2.5	1.558 ± 0.156	1885	6.8 ± 1.7
j7-M2B	1100	567.7 ± 2.3	1.019 ± 0.124	901	4.3 ± 2.0

vacuum quenching thermograms have been compared with AISI H13 CCT curves by [13]. The cooling rate between 800°C - 500°C is the most important cooling

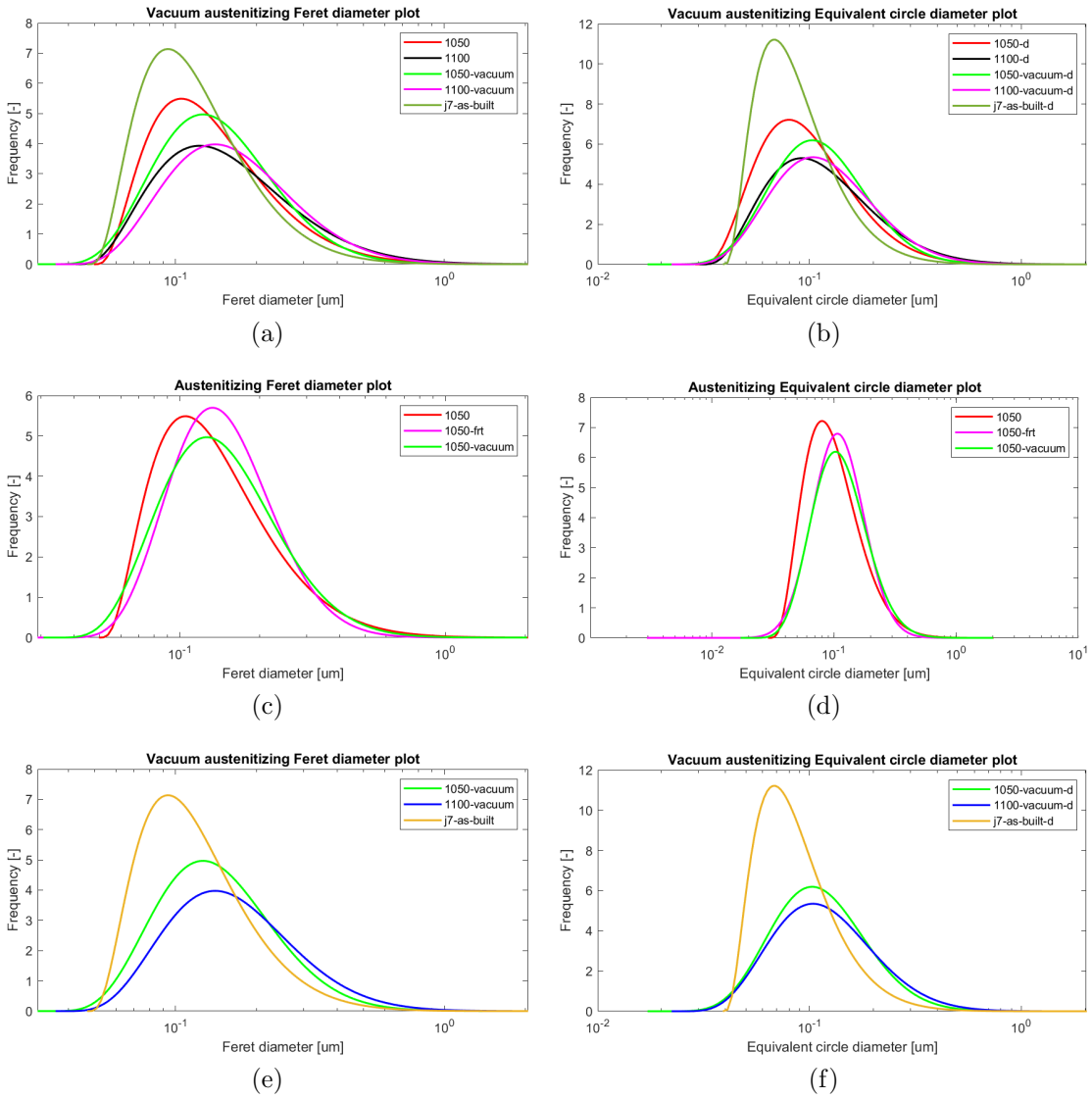

Figure 5.13: Vacuum austenitizing PSD curves at different austenitizing temperatures against the as-built condition: (a) Feret diameter plot, (b) Equivalent circle diameter plot, (c) comparison between 1050°C austenitizing conditions in Feret PSD, (d) comparison between 1050°C austenitizing conditions in Equivalent circle PSD, (e) final austenitizing choice in Feret PSD, (f) final austenitizing choice in Equivalent circle PSD.

parameter to characterize the quenching step. As already pointed out, the measured hardness is lower than that predicted by the CCT curves for two possible reasons: the reference H13 is a wrought product with a specific grain size and the CCT curves refer to an austenitizing temperature of 1020°C with a holding time

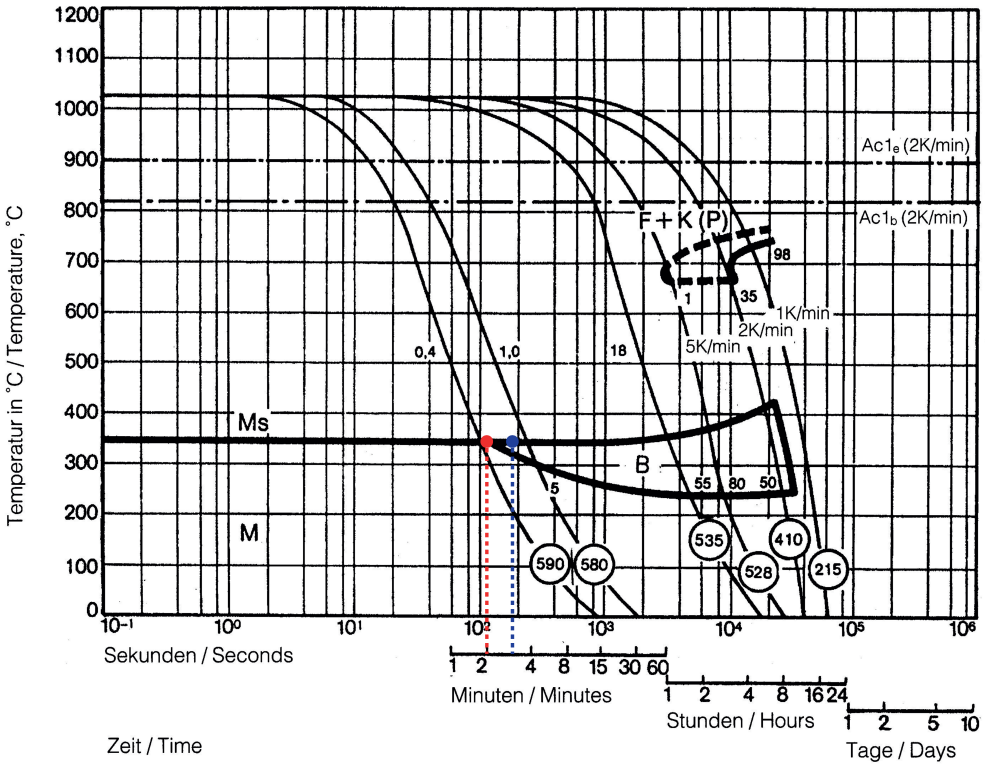

Figure 5.14: CCT curve of AISI H13 reporting the cooling path followed during 1050°C and 1100°C gas quenching indicated with in red (1050°C) and blue (1100°C).

Table 5.9: Main cooling parameters in gas quenching with cooling rate between T_{aust} - 350°C and 800°C - 500°C.

Sample	**T_{aust}[°C]**	**Macro-HV 100**	**Cooling rate T_{aust} - 350°C [°C/s]**	**Cooling rate 800°C - 500°C [°C/s]**
j7-M2B	1050	544.0 ± 2.5	5.48	6.38
j7-M2B	1100	567.7 ± 2.3	4.35	3.66

of 15 min. Cooling rates between T_{aust} - 350°C and between 800°C - 500°C have been reported in table 5.9.

Table 5.10: Summary of tempering data from 1050°C quenched specimens where hardness, carbides fraction and retained austenite are shown.

Sample	**T_{temp}[°C]**	**Macro-HV 100**	**Carbide fraction [%]**	**Count [4 photos]**	**Retained austenite [%]**
j7-M2B	400	544.0 ± 7.1	1.390 ± 0.082	2196	5.3 ± 1.8
j7-M2B	500	570.3 ± 1.2	1.100 ± 0.187	2212	2.8 ± 1.6
j7-M2B	550	558.0 ± 4.1	1.161 ± 0.267	1157	0.7 ± 0.4
j7-M2B	650	397.0 ± 0.1	1.683 ± 0.226	3947	0.5 ± 0.2

5.4 Tempering

The samples which underwent the vacuum austenitizing treatment with gas quenching were double tempered in air, following the procedure described in section 4.7. Tempering curves reporting hardness evolution with temperature are shown in 5.19 while tempering summary data are reported in table 5.10 and 5.11. A first decrease in hardness at T<400°C is caused by preliminary transformation of martensite, while a broad peak is present at temperatures around 500°C for both quenching temperatures, due to secondary carbides precipitation. Peak hardness was measured to be 570.3 HV (54 HRC) for 1050°C and 591.7 HV (55 HRC) for 1100°C quenching, exceeding that of the as-quenched state, respectively. At 550°C the Vickers hardness drops of only 10 HV due to further tempering of martensite, while above 600°C the effect of carbides coarsening and tempering of martensite overlap, causing a significant loss of mechanical properties. OM and SEM micrographs are reported for four tempering conditions: 400°C, 500°C, 550°C and 650°C in figure 5.15, 5.16, 5.17 and 5.18. Furthermore, it is reasonable to assume that both carbon and nitrogen would dissolve in the matrix during austenitizing. During tempering, nitrogen may have diffused together with carbon to form fine V-rich carbonitrides, as depicted by [3], while strengthening the matrix through the solid solution mechanism.

From OM micrographs a gradual tempering of martensite can be evaluated as a function of temperature, with formation of ferrite and carbides evident for 650°C tempering condition in particular. SEM images in BSD mode show the evolution of carbides for the various tempering conditions. More pronounced coarsening and grain boundary precipitation is distinguishable at 650°C, while for lower temperatures, prior undissolved carbides are visible together with nanometric particles. To further characterize these particles TEM analysis would be needed, due to their small size. Tempering treatment causes the transformation of martensite in more thermodynamically stable phases, recovering strong inner residual stresses due to quenching. The diffusional processes of carbon start at temperatures around 100°C

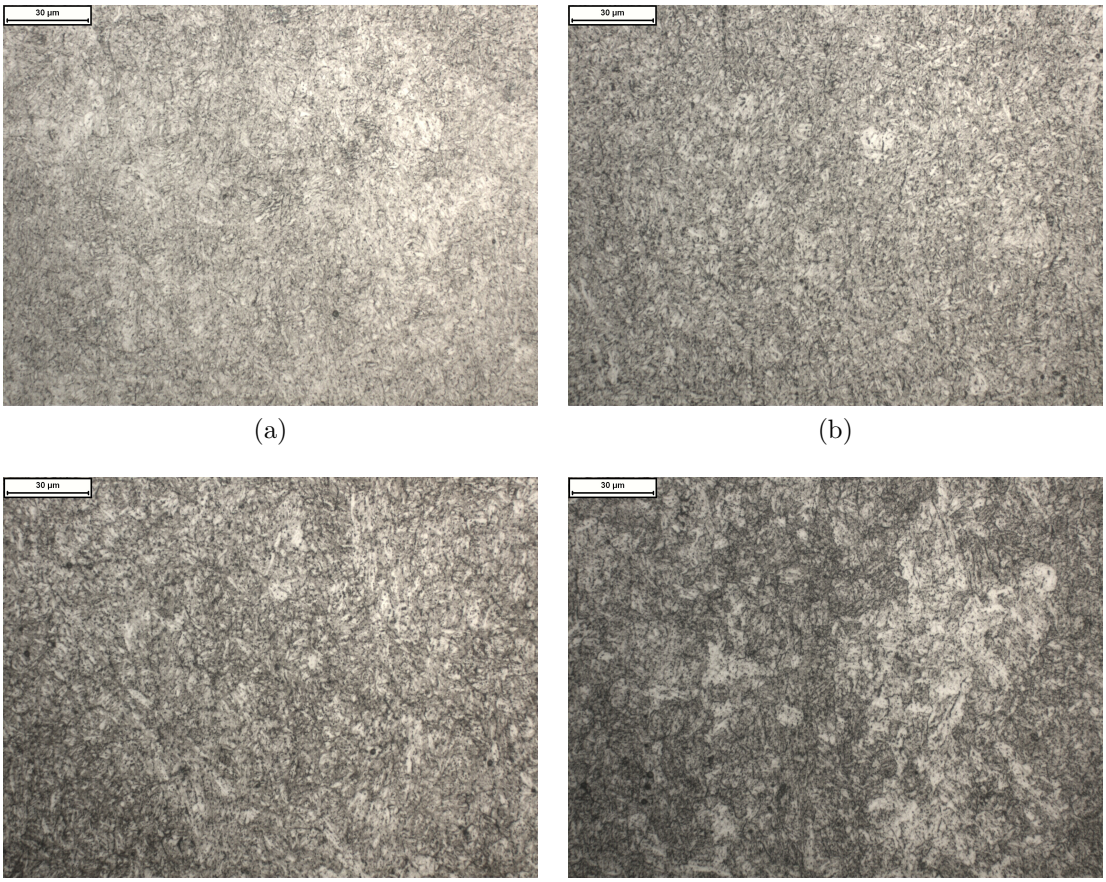

(a) (b)

(c) (d)

Figure 5.15: OM microstructures ×500 of double tempered specimens after etching (1050°C quenching): (a) 400°C, (b) 500°C, (c) 550°C, (d) 650°C.

Table 5.11: Summary of tempering data from 1100°C quenched specimens where hardness, carbides fraction and retained austenite are shown.

Sample	**T_{temp}[°C]**	**Macro-HV 100**	**Carbide fraction [%]**	**Count [4 photos]**	**Retained austenite [%]**
j7-M2B	400	560.7 ± 2.5	1.232 ± 0.047	1045	4.2 ± 2.1
j7-M2B	500	591.7 ± 2.6	1.064 ± 0.125	1069	2.6 ± 1.2
j7-M2B	550	580.7 ± 1.2	1.132 ± 0.047	929	0.7 ± 0.4
j7-M2B	650	397.0 ± 0.1	1.851 ± 0.150	3205	0.6 ± 0.3

- 250°C, causing the series of transformation described in section 2.5.2. In contrast, alloy elements such as Cr, Mo, V tend to diffuse at much higher temperatures,

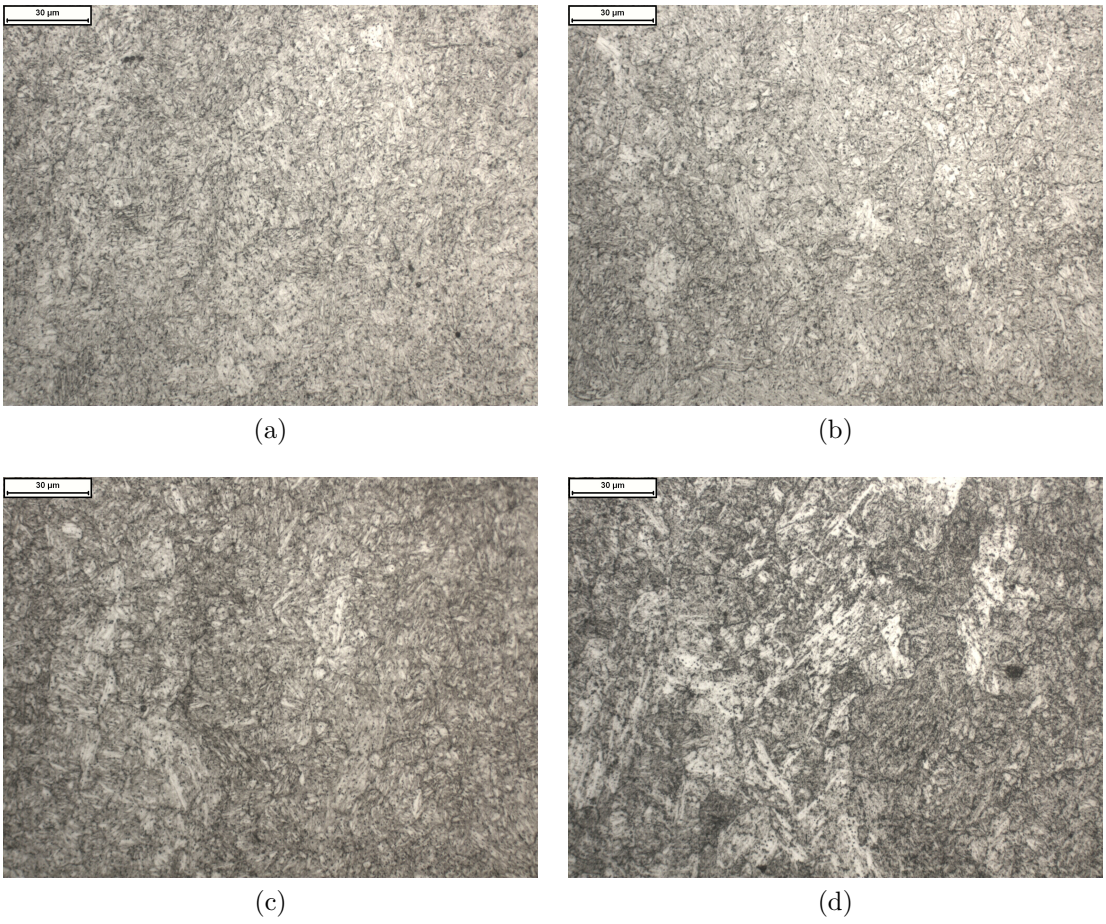

Figure 5.16: OM microstructures ×500 of double tempered specimens after etching (1100°C quenching): (a) 400°C, (b) 500°C, (c) 550°C, (d) 650°C.

starting from 400°C, forming carbides. By far the most important alloy carbides precipitating in N-rich H13 steel during tempering are M(C,N)-type carbonitrides (rich in V), which have the highest strengthening effect being finely dispersed with size less than 50 nm, as described by [28] and [27]. It has been also seen that the addition of N promotes the precipitation of finer V-rich carbonitrides with respect to N-free H13 samples. In figure 5.20 the carbide PSD curves as a function of tempering temperature are reported while in figure 5.21 it is shown the evolution of carbides fraction and of carbides count within the whole heat treatment. It is necessary to specify that the overall PSD analysis was evaluated by considering a threshold parameter corresponding to about 1561 nm^2. This means that only particles above this threshold, with an equivalent circle diameter of approximately 45 nm, were effectively taken into account. Therefore, these results are not able

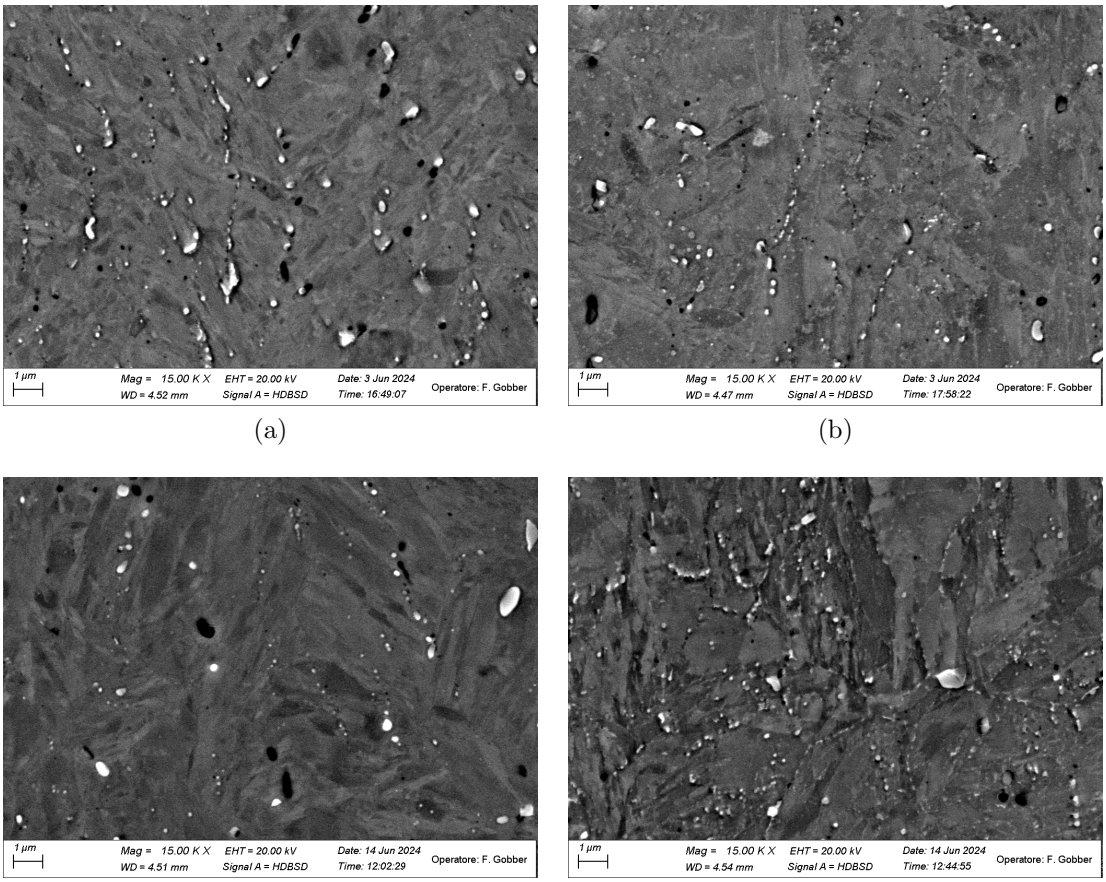

Figure 5.17: SEM microstructures ×15000 of double tempered specimens after etching (1050°C quenching): (a) 400°C, (b) 500°C, (c) 550°C, (d) 650°C.

to characterize effectively the precipitation of V(C,N) phases during tempering. This is the reason why the PSD curves obtained from tempering at 400°C, 500°C and 550°C do not deviate significantly from the as-quenched condition. The same consideration can be made regarding carbides count and fraction, while at 650°C, the precipitation and coarsening of carbides can be measured. This is probably due to $M_{23}C_6$ phases rich in Cr, having a much higher coarsening rate with respect to MC [21], [22]. The evolution of retained austenite with tempering temperature is shown in figure 5.22. Retained austenite levels remained around 4% - 5% until 450°C, following a drop at higher temperatures due to its complete transformation in ferrite and pearlite.

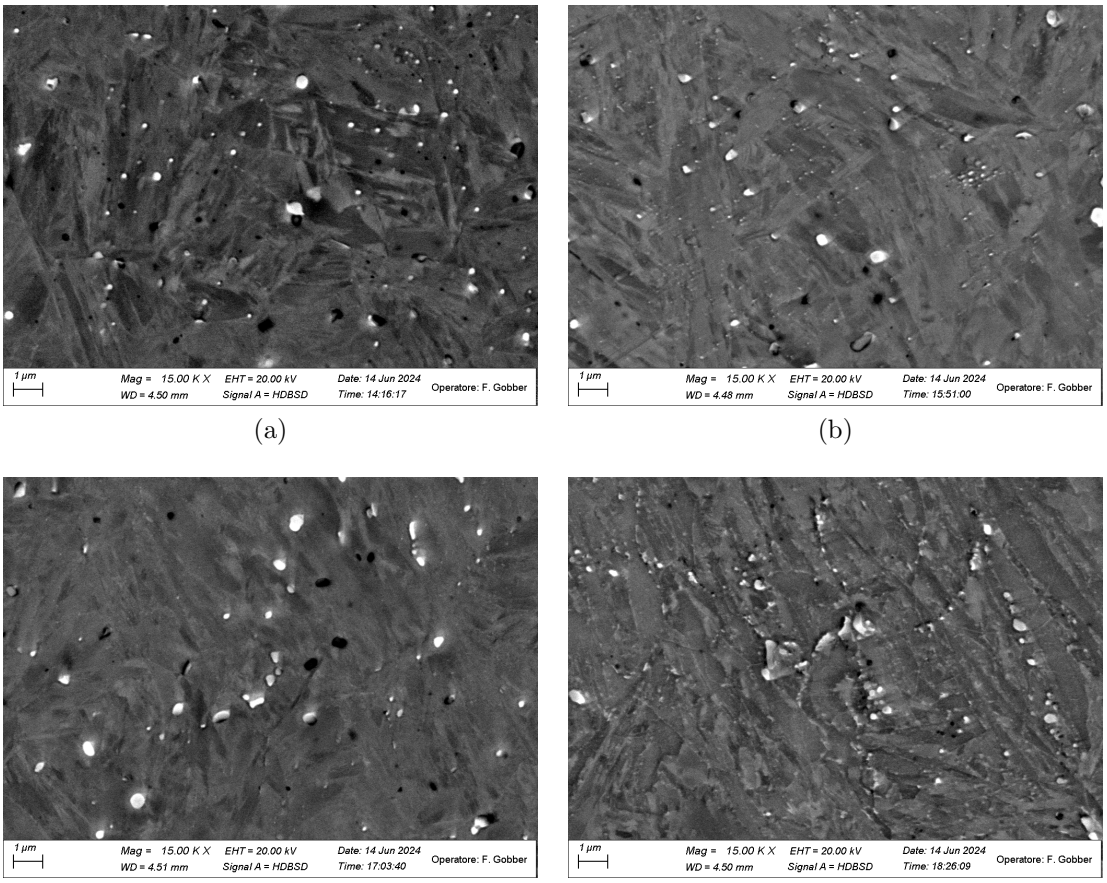

(a) (b)

(c) (d)

Figure 5.18: SEM microstructures ×15000 of double tempered specimens after etching (1100°C quenching): (a) 400°C, (b) 500°C, (c) 550°C, (d) 650°C.

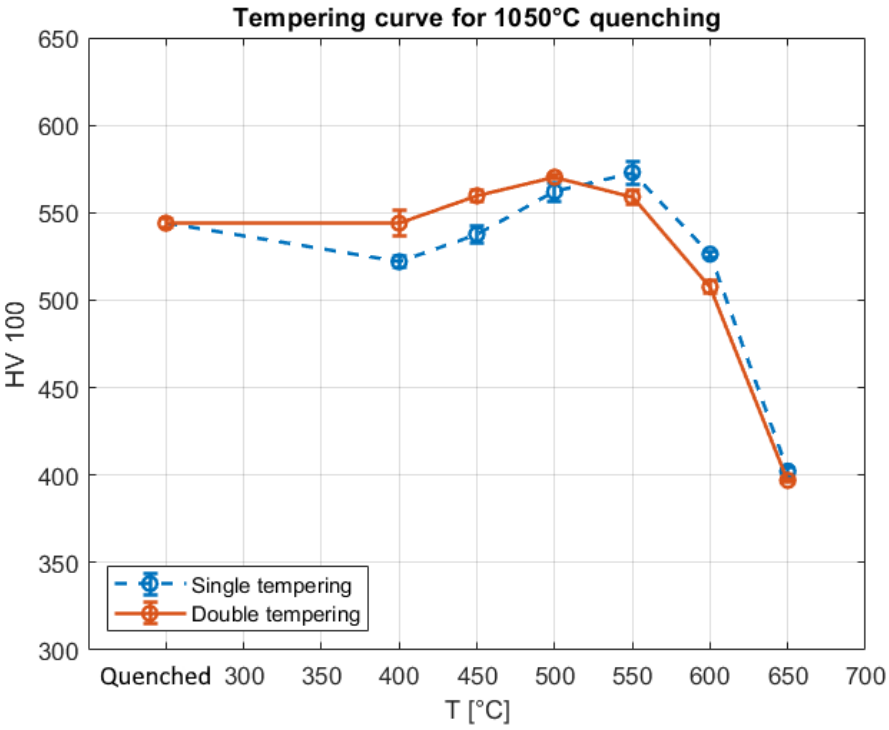

(a)

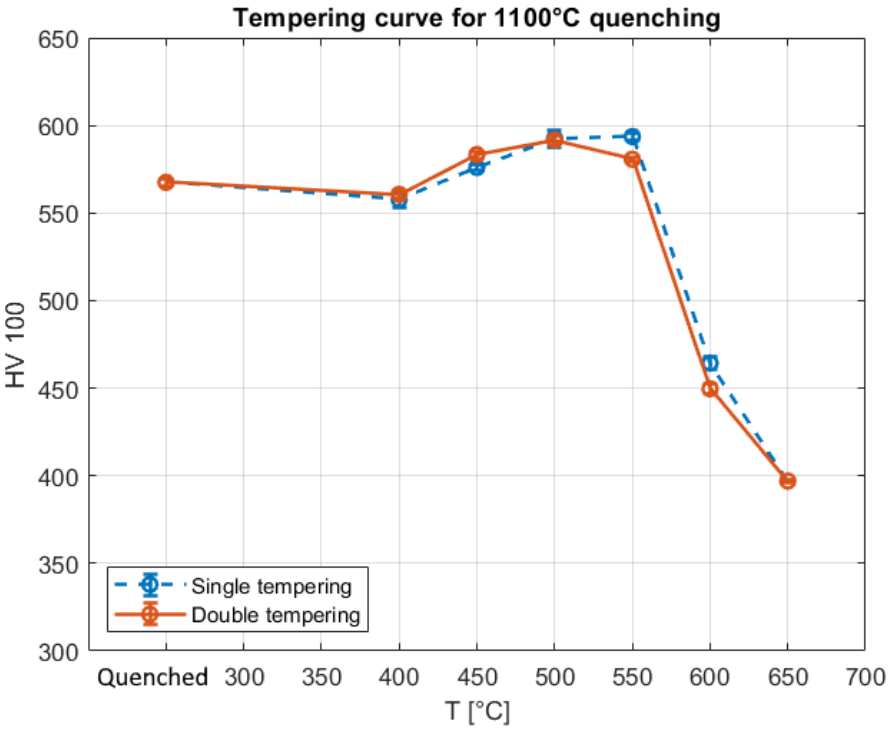

(b)

Figure 5.19: Tempering curves showing hardness evolution with respect to tempering temperature for (a) 1050°C and (b) 1100°C quenched samples. Single and double tempering hardness values are reported.

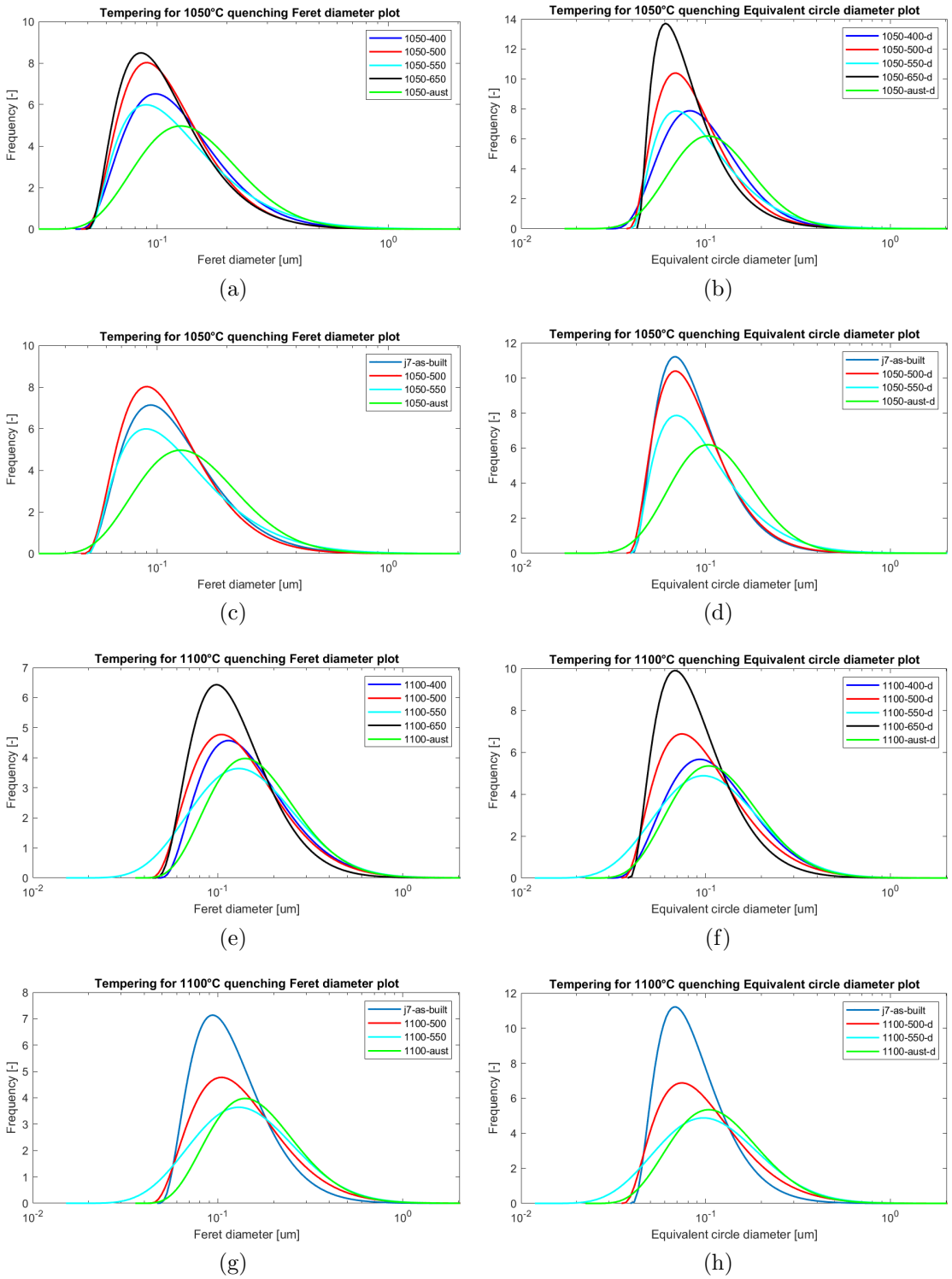

Figure 5.20: Carbide PSD curves evolution at different tempering temperatures against the as-quenched condition: (a), (b) 1050°C quenching Feret and equivalent circle diameter plot, (c), (d) 1050°C quenching Feret and equivalent circle diameter plot of most notable heat treatment conditions, (e), (f) 1100°C quenching Feret and equivalent circle diameter plot, (g), (h) 1100°C quenching Feret and equivalent circle diameter plot of most notable heat treatment conditions.

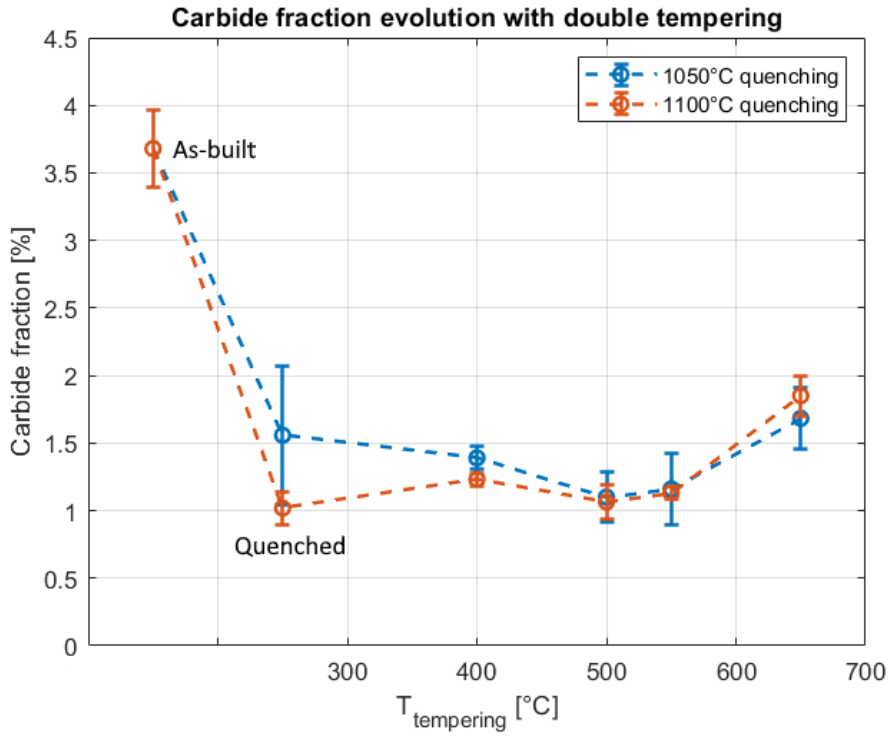

(a)

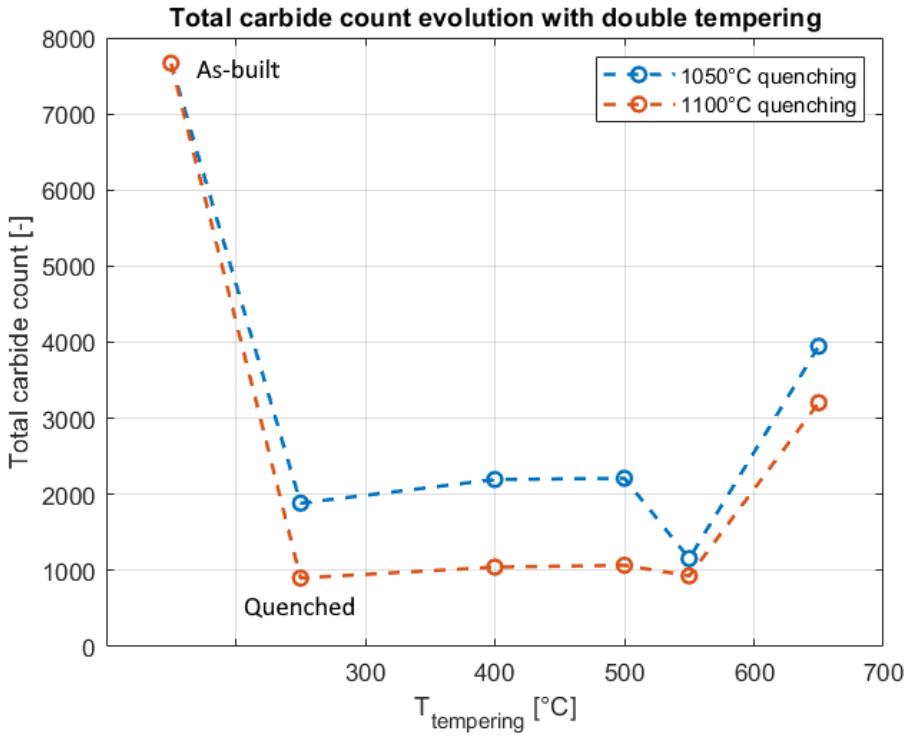

(b)

Figure 5.21: Carbide fraction and total carbides count evolution during for H13 heat treated specimens measured with image analysis (four photographs for each condition): (a) carbides fraction, (b) carbides count.

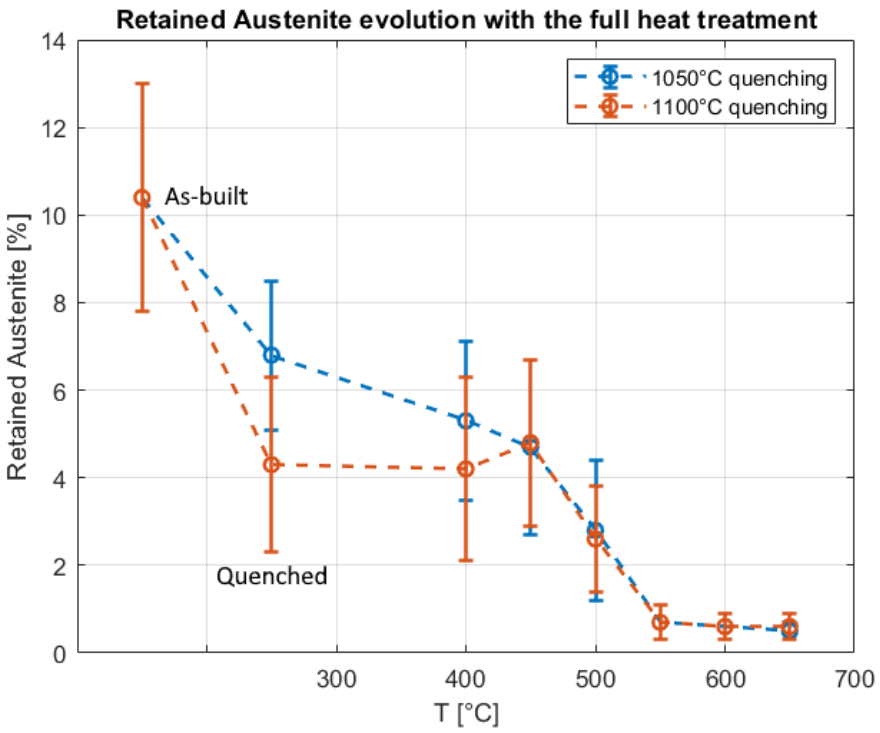

Figure 5.22: Evolution of retained austenite measured with XRD during the full heat treatment with major reference to tempering temperatures between 400°C - 650°C for both quenched specimens at 1050°C and 1100°C.

Chapter 6

Conclusions

Within this thesis work, the effects of different heat treatment conditions were studied for an AISI H13 hot-work tool steel manufactured through EBM with a bed preheat of 1040°C. Results show a possible process window for a correct processability of the alloy. By adopting a beam speed of 2000 mm/s with a beam current of 16 mA crack free and dense (>99%) specimens were obtained. These process parameters were effective both for relatively small cubic samples with 18 mm of side length and for larger 15×15×60 mm specimens. In particular the following results emerged:

- The high temperature soaking during the building stage determined heavy carbides precipitation phenomena at the grain boundaries and the formation of an elongated and dishomogeneous microstructure along the building direction. Despite that, no net hardness gradient hardness was measured in the as-built material.

- The presence of V-rich carbonitrides was verified through EDS analysis and led the heat treatment strategy towards investigating the effect of their dissolution on the mechanical properties, both in the as-built stage and in the austenitized condition. The work also covered an in-depth image analysis through Imagej software, obtaining as result the evolution of carbides PSD across the full heat treatment. However, a full characterization of V(C,N) carbonitrides precipitated during tempering still needs to be integrated with TEM analysis due to their small size (below 50 nm).

- Conventional austenitizing between 1025°C - 1100°C is not capable to fully dissolve such particles in the matrix, as expected from literature workings on the same wrought material. In fact, nitrogen increases the thermal stability of these carbides until temperatures of about 1300°C, which are far above

common austenitizing temperatures of wrought H13, bringing to strong effects of grain coarsening.

- This work proved the effectiveness of double tempering treatments on 1050°C and 1100°C vacuum quenched samples at temperatures between 500°C and 600°C. In both cases the peak hardness is located at 500°C with values around 570 HV (54 HRC) and 590 HV (55 HRC). Surface hardness lowers of about 10 HV for 550°C tempered specimens, due to tempering of martensite, while 600°C tempering involves higher loss in hardness. i.e. 510 HV (50 HRC) and 450 HV (45 HRC) for 1050°C and 1100°C quenched respectively.

- Lower temperatures tempering is not able to fully transform retained austenite, which keeps around 5% in volume fraction, while higher temperatures involve excessive tempering of martensite transforming to ferrite and carbides, hence bringing to a severe loss in hardness.

- Through a tuned heat treatment on the as-built material a net gain in mechanical properties was obtained compared to wrought H13. This can be attributed to the combined effect of EBM in producing relatively fine microstructures and to nitrogen addition in carbonitrides and in solid solution.

By adopting a manufacturing process such as EBM, which has intrinsic limitations, such as the long build time and the high price of feedstock powder, it is not only possible to design more complex geometries for tooling and inserts, but also finer microstructures performing better than traditional alternatives. In fact, the final heat treated H13 surpasses the required hardness specified in NADCA #207-2003 [31], GM DC-9999-1 [67] and Ford AMTD-DC 2010 [68], established between 44-46 HRC, allowing the application of such material for die casting applications with a possible high effectiveness as wear resistance regards. In particular, this hardness assessment suggests a maximum working temperature of 600°C, optimal for HPDC applications. Moreover, overcoming 50 HRC of hardness at lower temperatures would allow its exploitation also for injection molding of fibre reinforced polymers and for hot-extrusion matrices. However, the applicability of this material in the heat treated conditions developed in this work needs further experimental characterization in terms of impact toughness and thermal fatigue resistance. These properties cover an important role in tooling application, especially in the aluminium extrusion and die casting tooling sector where the sole hardness cannot represent the steel properties in its whole.

Bibliography

[1] G. Roberts, G. Krauss, and R. Kennedy, "Tool Steels", ASM International, 1998.

[2] R. A. Mesquita, Ed., "Tool Steels: Properties and Performance", Boca Raton: CRC Press, 2016.

[3] L. Li, W. Zhang, J. Gu, W. Li, F. Xu, e J. Li, "Effect of Nitrogen-Substituted Carbon on Thermal Stability of Cr-Mo-V Hot-Working Die Steel", steel research international, vol. 91, no. 10, p. 2000206, 2020.

[4] F. S. Gobber, C Ghibaudo, G. Marchese, S. Biamino, D. Ugues. "Characterization of an AISI H13 hot-work tool steel produced by Electron Beam Melting". Conference proceeding, Tooling Conference, EuroPM2021, Apr. 2022.

[5] [Online]. "Tool Steel Market Outlook, Growth, Report to 2030". Straits Research. Accessed: Jul. 18, 2024. Available: `https://straitsresearch.com/report/tool-steel-market`.

[6] [Online]. "Tool Steel Market Size and Share — Industry Statistics – 2028"', Global Market Insights Inc. Accessed: Jul. 18, 2024. Available: `https://www.gminsights.com/industry-analysis/tool-steel-market`.

[7] [Online]. "Tool Steel Market Size, Growth, Analysis e Forecast 2030", Credence Research. Accessed: Jul. 19, 2024. Available: `https://www.credenceresearch.com/report/tool-steel-market`.

[8] ASTM A681-08, "Standard specification for tool steels alloy" Materials Park, OH. ASTM International, 2022.

[9] ASTM A600-92, "Standard specification for tool steel high speed". Materials Park, OH. ASTM International, 2016.

[10] [Online] UNI EN ISO 4957:2018 "Tool Steels", 2018. International Organization for Standardization. Available at `https://www.iso.org/standard/4957.html`.

[11] J. Yasin, S. Selvakumar, P. Mathan Kumar, R. Sundaresan, and K. M. Arunraja, "Experimental study of TiN, TiAlN and TiSiN coated high speed steel tool", Materials Today: Proceedings, vol. 64, pp. 1707–1710, Jan. 2022.

[12] [Online] ISO 3252:2023, "Powder metallurgy — Vocabulary", 2023. International Organization for Standardization. Available at `https://www.iso.org/`

obp/ui/en/#iso:std:iso:3252:ed-6:v1:en.

[13] [Online]. "Hot work tool steels", Voelstalpine, Böhler. Accessed: Jul. 20, 2024. Available at https://www.bohler-edelstahl.com/app/uploads/sites/92/2018/10/BW015En_Hot-Work-Tool-Steel.pdf.

[14] D. Hull and D. J. Bacon, "Chapter 10 - Strength of Crystalline Solids", in Introduction to Dislocations (Fifth Edition), Oxford: Butterworth-Heinemann, pp. 205–249, 2011.

[15] [Online]. "About the failure of H13 steel die you need to know - cause and solution", Songshun Steel. Accessed: Sep. 03, 2024. Available at https://songshunsteel.com/analysis-h13-steel-die/.

[16] Z. Yang, X. Zhang, C. Sang, P. Wang, L. Zhang, and D. Li, "Effects of Rare Earth on the Microstructure and Mechanical Properties of a Pearlitic Steel Wire Rod", steel research international, vol. 94, no. 12, p. 2300063, 2023.

[17] [Online]. "DIN 1.2344 SKD61 Hot Work Mould Steel Bars with ANSI H13 Steel Grade — Fushun Special Steel Co., Ltd. - Professional Supplier of Special Steel, and Manufacturer of Tool Steel". Accessed: Aug. 29, 2024. Available at https://www.fushunspecialsteel.com/aisi-h13-1-2344-skd61-hot-work-mould-steel-bar/.

[18] G. Krauss, "Steels: Processing, Structure, and Performance, Second Edition". ASM International, 2015.

[19] L. D. Jaffe and B. Swartz, "Time-Temperature Relations in Tempering Steel.",Transactions of the Metallurgical Society of AIME, vol 162, pp. 223–249, 1945.

[20] F.D. Richardson, "The thermodynamics of metallurgical carbides and of carbon in iron". Journal of the Iron and Steel Institute, vol 175, pp. 33–51, 1953.

[21] A. Ning, W. Mao, X. Chen, H. Guo, and J. Guo, "Precipitation Behavior of Carbides in H13 Hot Work Die Steel and Its Strengthening during Tempering", Metals, vol. 7, no. 3, Mar. 2017.

[22] A. Ning, Y. Liu, R. Gao, S. Yue, M. Wang, and H. Guo, "Effect of Tempering Condition on Microstructure, Mechanical Properties and Precipitates in AISI H13 Steel", JOM, vol. 73, no. 7, pp. 2194–2202, Jul. 2021.

[23] N. Du et al., "Formation mechanism of MC and M2C primary carbides in as-cast M50 bearing steel", Materials Characterization, vol. 174, p. 111011, Apr. 2021.

[24] A. Ning, Y. Liu, R. Gao, S. Yue, M. Wang, and H. Guo, "Effect of austenitizing condition on mechanical properties, microstructure and precipitation behavior of AISI H13 steel", J. Iron Steel Res. Int., vol. 31, no. 1, pp. 143–156, Jan. 2024.

[25] K. Shi, F. Zhao, Y. Liu, S. Yin, and R. Yang, "The Effect of the Pre-Existing VC on the Evolution of Precipitate and Mechanical Properties in the H13

Steel", Materials (Basel), vol. 15, no. 11, pp. 3970, Jun. 2022.

[26] N. Angang, G. Hanjie, C. Xichun, and W. Mingbo, "Precipitation Behaviors and Strengthening of Carbides in H13 Steel during Annealing", Materials Transactions, vol. 56, no. 4, pp. 581–586, 2015.

[27] J. Gu, J. Li, and J. Huo, "Effect of Precipitation on Hardening and Toughening of Nitrogen-Alloyed H13 Steel," steel Res. Int., vol. 88, no. 11, pp. 1700031, Nov. 2017.

[28] J.-Y. Li, Y.-L. Chen, and J.-H. Huo, "Mechanism of improvement on strength and toughness of H13 die steel by nitrogen," Mater. Sci. Eng. A, vol. 640, pp. 16–23, Jul. 2015.

[29] J. Li, P. Zhao, J. Yanagimoto, S. Sugiyama, and Y. Chen, "Effects of heat treatment on the microstructures and mechanical properties of a new type of nitrogen-containing die steel," Int. J. Miner. Metall. Mater., vol. 19, no. 6, pp. 511–517, Jun. 2012.

[30] Y.-L. Chen, B. Liu, and J.-Y. Li, "Study on Heat Treatment of Nitrogen H13 Steel", Advanced Materials Research, vol. 146–147, pp. 1885–1888, 2011.

[31] [Online] NADCA #207-2003 "S H13 Steel Acceptance and Heat Treat Criteria - 2003 I", 2003. Available at `https://www.diecasting.org/Web/Resources/Technical_Standards/Web/R_D/Standards.aspx`.

[32] H. Danninger and C. Gierl-Mayer, "7 - Advanced powder metallurgy steel alloys", in Advances in Powder Metallurgy, I. Chang and Y. Zhao, Eds., Woodhead Publishing Series in Metals and Surface Engineering., Woodhead Publishing, pp. 149–201, 2013.

[33] R. P. M. Guimarães et al., "Advances in Metal Additive Manufacturing", S. Salunkhe, S. T. Amancio-Filho, and J. P. Davim, Eds., in Woodhead Publishing Reviews: Mechanical Engineering Series., Woodhead Publishing, pp. 1–104, 2023.

[34] D. Joshi and B. Ravi, "Quantifying the Shape Complexity of Cast Parts", Computer-Aided Design and Applications, vol. 7, no. 5, pp. 685–700, Jan. 2010.

[35] M. Armstrong, H. Mehrabi, and N. Naveed, "An overview of modern metal additive manufacturing technology", Journal of Manufacturing Processes, vol. 84, pp. 1001–1029, Dec. 2022.

[36] L. Rännar, A. Glad, and C. Gustafson, "Efficient cooling with tool inserts manufactured by electron beam melting", Rapid Prototyping Journal, vol. 13, no. 3, pp. 128–135, Jan. 2007.

[37] N. Omidi, P. Farhadipour, L. Baali, K. Bensalem, N. Barka, and M. Jahazi, "A Comprehensive Review of Additively Manufactured H13 Tool Steel Applicable in the Injection Mold Industry: Applications, Designs, Microstructure, Mechanical Properties", JOM, vol. 75, no. 11, pp. 4457–4469, Nov. 2023.

[38] "ISO/ASTM 52900:2021(en), Additive manufacturing — General principles — Fundamentals and vocabulary". International Organization for Standardization. Available at `https://www.iso.org/obp/ui/#iso:std:iso-astm:52900:ed-2:v1:en`.

[39] P. Bajaj, A. Hariharan, A. Kini, P. Kürnsteiner, D. Raabe, and E. A. Jägle, "Steels in additive manufacturing: A review of their microstructure and properties", Materials Science and Engineering: A, vol. 772, pp. 138633, Jan. 2020.

[40] D. Masaylo, S. Igoshin, A. Popovich, A. Orlov, A. Kim, and V. Popovich, "Microstructural and Hardness Behavior of H13 Tool Steel Manufactured by Ultrasound-Assisted Laser-Directed Energy Deposition", Metals, vol. 12, no. 3, Art. no. 3, Mar. 2022.

[41] D.-G. Ahn, "Directed Energy Deposition (DED) Process: State of the Art", Int. J. of Precis. Eng. and Manuf.-Green Tech., vol. 8, no. 2, pp. 703–742, Mar. 2021.

[42] R. Chkalov and D. Chkalova, "Laser Powder Cladding Complex: Principles of Advanced Automated Control", IOP Conference Series: Materials Science and Engineering, vol. 969, pp. 012093, Nov. 2020.

[43] S. S. Joshi, S. Sharma, S. Mazumder, M. V. Pantawane, and N. B. Dahotre, "Solidification and microstructure evolution in additively manufactured H13 steel via directed energy deposition: Integrated experimental and computational approach", Journal of Manufacturing Processes, vol. 68, pp. 852–866, Aug. 2021.

[44] X. Zhao et al., "The effect of thermal cycling on direct laser-deposited gradient H13 tool steel: Microstructure evolution, nanoprecipitation behaviour, and mechanical properties", Materials Today Communications, vol. 25, pp. 101390, Dec. 2020.

[45] X. Du, X. Liu, Y. Shen, R. Liu, and Y. Wei, "H13 tool steel fabricated by wire arc additive manufacturing: Solidification mode, microstructure evolution mechanism and mechanical properties", Materials Science and Engineering: A, vol. 883, pp. 145536, Sep. 2023.

[46] J. Ge, N. Fan, Y. Long, J. Lin, Y. Lei, and S. Yin, "Investigation on H13 buildups produced with wire arc additive manufacturing: Deposition strategies-induced microstructural evolution and mechanical performances", Journal of Alloys and Compounds, vol. 860, pp. 157893, Apr. 2021.

[47] J. Mazumder, J. Choi, K. Nagarathnam, J. Koch, and D. Hetzner, "The direct metal deposition of H13 tool steel for 3-D components", JOM, vol. 49, no. 5, pp. 55–60, 1997.

[48] T. A. Rodrigues, V. Duarte, R. M. Miranda, T. G. Santos, and J. P. Oliveira, "Current Status and Perspectives on Wire and Arc Additive Manufacturing (WAAM)", Materials (Basel), vol. 12, no. 7, pp. 1121, Apr. 2019.

[49] F. Niu, W. Bi, K. Zhang, X. Sun, G. Ma, and D. Wu, "Additive manufacturing of 304 stainless steel integrated component by hybrid WAAM and LDED", Materials Today Communications, vol. 35, pp. 106227, Jun. 2023.

[50] R. Mertens, B. Vrancken, N. Holmstock, Y. Kinds, J.-P. Kruth, and J. Van Humbeeck, "Influence of Powder Bed Preheating on Microstructure and Mechanical Properties of H13 Tool Steel SLM Parts", Physics Procedia, vol. 83, pp. 882–890, Jan. 2016.

[51] M. Galati and L. Iuliano, "A literature review of powder-based electron beam melting focusing on numerical simulations", Additive Manufacturing, vol. 19, pp. 1–20, Jan. 2018.

[52] T. Wenz, A. Kirchner, B. Klöden, T. Weißgärber, and M. Jurisch, "Processing of High-Carbon Steel by Selective Electron Beam Melting", steel research international, vol. 91, no. 5, p. 1900479, 2020.

[53] C. Botero et al., "Additive Manufacturing of a Cold-Work Tool Steel using Electron Beam Melting", steel research international, vol. 91, no. 5, p. 1900448, 2020.

[54] J. L. Bartlett and X. Li, "An overview of residual stresses in metal powder bed fusion", Additive Manufacturing, vol. 27, pp. 131–149, May 2019.

[55] E. B. Fonseca, A. H. G. Gabriel, L. C. Araújo, P. L. L. Santos, K. N. Campo, and E. S. N. Lopes, "Assessment of laser power and scan speed influence on microstructural features and consolidation of AISI H13 tool steel processed by additive manufacturing", Additive Manufacturing, vol. 34, pp. 101250, Aug. 2020.

[56] M. Narvan, K. S. Al-Rubaie, and M. Elbestawi, "Process-Structure-Property Relationships of AISI H13 Tool Steel Processed with Selective Laser Melting", Materials, vol. 12, no. 14, Art. no. 14, Jan. 2019.

[57] M. Katancik, S. Mirzababaei, M. Ghayoor, and S. Pasebani, "Selective laser melting and tempering of H13 tool steel for rapid tooling applications", Journal of Alloys and Compounds, vol. 849, 2020.

[58] M. Kahlert, F. Brenne, M. Vollmer, and T. Niendorf, "Influence of Microstructure and Defects on Mechanical Properties of AISI H13 Manufactured by Electron Beam Powder Bed Fusion", J. of Mater. Eng. and Perform., vol. 30, no. 9, pp. 6895–6904, Sep. 2021.

[59] A. Kirchner, B. Klöden, M. Franke-Jurisch, L.-I. Rauh-Hain, and T. Weißgärber, "Manufacturing of Tool Steels by PBF-EB", Metals, vol. 11, no. 10, Art. no. 10, Oct. 2021.

[60] D. Cormier, O. Harrysson, and H. West, "Characterization of H13 steel produced via electron beam melting", Rapid Prototyping Journal, vol. 10, no. 1, pp. 35–41, Jan. 2004.

[61] X. Yang et al., "Microstructure evolution and mechanical properties of H13

steel produced by Selective Electron Beam Melting", Materials Characterization, vol. 203, pp. 113053, Sep. 2023.

[62] [Online]. J. He, "H13 Tool Steel — 1.2344 — X40CrMoV5-1 — SKD61 Hot Work Steel", Otai Special Steel. Accessed: Sep. 09, 2024. Available at `https://www.astmsteel.com/product/h13-tool-steel-x40crmov5-1-skd61-hot-work-steel/`.

[63] C. Ghibaudo et al., "Information-rich quality controls prediction model based on non-destructive analysis for porosity determination of AISI H13 produced by electron beam melting", Int J Adv Manuf Technol, vol. 126, no. 3, pp. 1159–1173, May 2023.

[64] [Online] ASTM E3-01:2017. "Standard Guide for Preparation of Metallographic Specimens". Accessed: Sep. 09, 2024. Available at `https://www.astm.org/e0003-11r17.html`.

[65] [Online] ASTM E975:2013. "Standard Practice for X-Ray Determination of Retained Austenite in Steel with Near Random Crystallographic Orientation". Accessed: Sep. 10, 2024. Available at `https://shorturl.at/ONPJd`.

[66] UNI EN ISO 6507-1, "Materiali metallici - Prova di durezza Vickers - Parte 1: Metodo di prova", 2018.

[67] [Online] GM DC-9999-1 "Standard Specification Die insert material and heat treating specification", 2005. Available at `https://www.diecasting.org/docs/Rev18.pdf`.

[68] [Online] Ford AMTD-DC2010 "Die insert material and heat treatment performance requirements general applications", 2005. Available at `https://www.diecasting.org/docs/AMTD_DC2010_RevL.pdf`.